Enhancing Proton Conduction in Metal Organic Frameworks by Post-synthetic Modification

A Thesis

Submitted in Partial Fulfillment of the Requirements

for the Degree of

Doctor of Philosophy

by

Shalini

ID: 20123205

Indian Institute of Science Education and Research (IISER), Pune, 2018

Dedicated to

My family

Certificate:

This is to certify that the work incorporated in the thesis entitled "**Enhancing Proton Conduction in Metal Organic Frameworks by Post-synthetic Modification**" submitted by **Shalini** has been carried out by the candidate at the Indian Institute of Science Education and Research (IISER), Pune, under my supervision. The work presented here or any part of it has not been included in any other thesis submitted previously for the award of any degree or diploma from any other University or Institution.

Date:

Dr. R. Vaidhyanathan
(Research Supervisor)
Associate Professor, IISER-Pune
Pune-411008, India

Declaration

I hereby declare that the thesis entitled "**Enhancing Proton Conduction in Metal Organic Frameworks by Post-synthetic Modification**" submitted for the degree of Doctor of Philosophy in Chemistry at Indian Institute of Science Education and Research (IISER), Pune has not been submitted by me to any other University or Institution. This work was carried out at Indian Institute of Science Education and Research (IISER), Pune, India under the supervision of Dr. R. Vaidhyanathan.

Date: Shalini

Acknowledgement

To start with, I would like to express my heartfelt gratitude to my research supervisor Dr. R. Vaidhyanathan for his support and encouragement throughout the whole tenure of my Ph.D. His guidance, support, and patience these past years have made this work possible. Not only did he teach me how to propose a scientific project and complete it productively, but he also trained me how to communicate science. I still have a long way to go in those regards, and as I work to get better, I will always measure myself against his standard. He was there at each step of the journey and motivated me enough every time I lost hope. He constantly believed in me, even when I didn't believe in myself. Being his first student, I also got the opportunity to set up the lab, which was an exciting and learning experience in itself. I thank Indian Institute of Science Education and Research (IISER), Pune and the former Director Prof. K. N. Ganesh (who was always approachable and available) for providing excellent research facilities, funding and an amazing and friendly research atmosphere. I would also like to acknowledge the current director Prof. Jayant B. Udgaonkar for taking over the task and continuing at the same pace. I am extremely thankful to DST, SERB, and Enovex for the funding.

I would like to convey my sincere thankfulness to Dr. R. Boomi Shankar (IISER Pune) and Dr. Rajesh G. Gonnade (CSIR-NCL Pune) for serving on my Research Advisory Committee (RAC). Their precious suggestions during the discussion sessions helped me shape my projects better. I am also thankful to Dr. Sreekumar Kurungot (CSIR-NCL Pune), Dr. T.G. Ajithkumar (CSIR-NCL Pune), and Prof. Ulrike Werner-Zwanziger (University of Dalhousie) for their collaborative research inputs. I am extremely grateful to all the faculty members of IISER Pune and Prof. M. Jayakanan (the chair, chemistry department) for their kind assistance.

I thank my lab mates Aparna, Dinesh, Debanjan, Rahul, Rinku, Sattwick, and Shyama for their help. I would also like to recognize the help from the former group members Harpeet, Satya, Neha, and the summer project fellows Hemkalyan, Shubhangi, Suchit, Nidhi, Bhavin, and Yogesh. I am thankful to Dr. Vishal M. Dhavale, Dr. Santosh K. Singh, Rajith, Siddheshwar N. Bhange, Kavalakal M. Eldho, and Malvika Dutt from CSIR-NCL Pune for carrying out some of the measurements for my projects.

I would take this opportunity to state my sincere gratefulness to the professors who taught me in my masters and bachelors. Special thanks to Prof. Monika Datta who is the main reason I decided to pursue research. After my masters, I had the privilege of working with Professor

Ashok Ganguly (IIT Delhi, and Director at Institute of Nano Science & Technology) who made room for me in his research group and found funding for me to work as a research assistant. It was in his group that I got the first taste for materials chemistry and nano-materials.

I would like to thank Dr. Umeshareddy Kacherki (deputy librarian) and Anuradha for library support. Heartfelt thanks to all the instrument operators (Mr. Parveen Nasa, Mrs. Archana, Mr. Nilesh Dumbre, Ms. Swati, Ms. Nayana, Mr. Anil, Mr. Mahesh, Mr. Yatish, Mr. Nitin, Mrs. Megha to name a few), as well as all the IISER Pune non-teaching staff members, especially Mr. Mayuresh, Mr. Tushar, Ms. Vrushali, Mr. Prabhas, Mr. Suresh, Mr. Sandeep, Ms. Mariamma for their support during last six years.

I would like to thank Pallavi, Avinash, Aditya, Mitu, Gandharva, Sneha, and Ankit for being my constants. Alden has always been there for me and is the best friend one can ever ask for. Kunalika is the closest friend and confidant in IISER. After I talk to her about any situation that seems daunting, I feel I can handle it. Vikram is great to talk science with, and his non-stop blabbering about astronomy never makes any sense to me. Pooja and Simi have been my partners in crime, always up to handle my crazy. I had a great time exploring Pune with Harsha, Chopra, Priyank, Katti, Omkar, Abhijeet, and Harjot. Abhay, Thakur, Yogesh, Prithvi, Mukta, Mahesh, Desai, and Chavan made Pune feel like a home away from home. It is always the most fun to celebrate life achievements with the IISER friends Abhik, Aditi, Aman, Ankur, Avishek, Harpreet, Joyeeta, Jyoti, Niraja, Nishtha, Sonashree, Sudeshna, Sunil, Vikash, and Yamini. If I am forgetting anyone, please remember you are in my heart.

I am extremely thankful to my family especially my brother (Sanjay) and sister in law (Seema) for their unconditional and selfless love and support throughout my whole academic career. It wouldn't have been possible for me to achieve all that I have without their support. The example my brother has set for the values of integrity, morality, hard work, and fair-mindedness has served as guidance for me in my Ph.D. and my life as a whole. I look up to him. I would also thank my niece and my nephew, Aarzoo and Avdeep, just for existing in this world. Well, just talking to them always takes all the stress away. Finally, I would sign off by thanking my late mother who has been a continuous pillar of strength throughout my whole life. It is to them that I dedicate this work.

Acknowledgement

Thank you to everyone who made this thesis possible and kept me sane these past six years.

Shalini

Table of contents

Abstract

The human need for energy is increasing in response to the increasing population, rapid urbanization and industrialization, especially in the developing countries. U.S. Energy Information Administration's (EIA) recently released International Energy Outlook 2013 (IEO2013) projects claim that the global energy consumption will increase by 56% between 2010 and 2040. In response to this demand, various energy alternatives to fossil fuels are being looked at, out of which, fuel cells have proven to be a promising candidate due to their high conversion efficiency, low pollution, and high fuel flexibility. They are electrochemical conversion devices that produce electrical energy from the chemical energy of a fuel and oxygen at high thermodynamic efficiencies. They mainly have three components; the cathode, the anode, and the electrolyte. At one of the electrodes hydrogen is oxidized to protons. The electrolyte is necessary to transfer these protons to the other electrode, where they combine with the oxygen to form water. At present, Nafion is the commercially used electrolyte membrane which has a conductivity of 10^{-2} to 10^{-1} S/cm in the presence of humidity, but it fails to conduct ions at a higher temperature under anhydrous conditions. Regardless, the Nafion is still the commercially used proton conducting electrolyte because of its robust structure, excellent thermal and mechanical stability, high proton conductivity and reusability without any significant loss of activity.

Various materials are being studied to be used as electrolytes in the fuel cells. Developing Metal Organic Framework (MOF) - based proton-conducting electrolytes for fuel-cell applications is an important target that has drawn a lot of attention. They are coordination framework compounds formed by linking metal ions/clusters via organic linkers and have emerged as a new class of functional materials. The modular and crystalline nature of the MOF permits controlled introduction of functional species and characterization of their composition with high precision, a task which is very difficult to achieve in amorphous polymers. This makes MOFs excellent for hosting proton bearing guests and the chemistry around their framework can be tuned to function cooperatively with the guests to obtain desirable proton conductivity values.

In this context, we have developed a few dense MOFs which display very interesting proton conducting properties. Via an experimental-modeling approach, we show how the extra-framework species can be site-specifically modulated to enhance the proton conduction by constructing highly ordered hydrogen bond pathways within the MOF. From a comparison of

three structurally related metal terephthalate frameworks, we realize that we need an amphoteric guest in the MOF which can form a hydrogen-bonded network and thus help in the transfer of protons. Post-synthetic loading of ethylene glycol, a strong hydrogen bonding and coordinating guest, in the MOF help us achieve a 1000-fold enhancement in the humidity-dependent proton conductivity. The post-synthetic approach we adopt makes it very generic. Similarly, we demonstrate how highly hydrating sites can be embedded into MOF to achieve up to 10000-fold enhancement in hydrous conductivity. Loading Cs^+ ions to bring in more coordinated and acidic water in the same MOF helps attain conductivity values comparable to that of Nafion. Unfortunately, none of these show any high-temperature proton conductivity.

In another system, wide-temperature range proton conductivity, i.e., both humidity dependent as well as anhydrous conductivity (30° to 150˚C). A 3-dimensional, dense MOF having azoles in the pores as proton-conducting guests conducts at 10^{-3} S/cm at 90˚C and 90% RH but fails to show any conductivity at higher temperatures under anhydrous conditions. Using a post-synthetic strategy, the conductivity value has been pushed to 10^{-2} S/cm at 90˚C, and 90% RH and conductivity of the order of 10^{-4} S/cm at 150˚C has been attained. Considering, relatively very few MOFs showing anhydrous conductivity are reported, this, we believe, is a worthy achievement.

The investigations in this thesis include (i) synthesis of dense MOFs as proton conducting electrolytes; (ii) understanding the proton-transfer pathways and proton conducting characteristics of the MOFs through a combined experimental-modeling approach; (iii) post-synthetic modifications of the MOFs to enhance the proton conductivities and to achieve anhydrous proton conductivity.

List of Acronyms:

1. AC: Alternating Current
2. adp: Adipate
3. AFCs: Alkaline Fuel Cells
4. Å: Angstrom
5. BDC: Benzene-1,4-dicarboxylate
6. 1,4-bdc: 1,4-benzenedicarboxylate
7. BPDSDC: Biphenyl-3,30-disulphonyl-4,40-dicarboxylic acid
8. CPE: Constant Phase Element
9. DC: Direct Current
10. DFT-TB: Tight Binding Density Functional Theory
11. DMA: Dimethyl Ammonium
12. DMF: N,N-dimethylformamide
13. DOE: Department Of Energy
14. DOTP: 2,5-dioxidoterephthalate
15. Ea: Activation Energy
16. EG: Ethylene glycol
17. eV: electron volt
18. FCs: Fuel Cells
19. GCMC: Grand Canonical Monte Carlo
20. Hpdec: High power decoupling
21. Hpy: Pyridinium cation
22. I: Current
23. ICE: Internal Combustion Engine
24. ICP: Inductively Coupled Plasma
25. Imdc: 4,5-imidazoledicarboxylate
26. I_o: Amplitude of the signal
27. I_t: Current at time t
28. kW·h/kg: kilowatt.hour per gram
29. MAS NMR: Magic Angle Spinning NMR
30. MCFCs: Molten Carbonate Fuel Cells

31. MEA: Membrane Electrolyte Assembly
32. MOF: Metal Organic Framework
33. Mpca: 5-methyl-2-pyrazinecarboxylate
34. mW/cm^2: mili-Watt per centimeter square
35. n: Mobile charge carriers per unit volume
36. NDC: Naphthalene-2,6-dicarboxylate
37. 1,4-ndc: 1,4-naphthalenedicarboxylate
38. NiMH: Nickel Metal Hydride
39. nm: Nanometer
40. ox: Oxalate
41. PAFCs: Phosphoric Acid Fuel Cells
42. PbA: Lead Acid
43. PCMOF: Proton Conducting Metal Organic Framework
44. PEMFCs: Polymer Electrolyte Membrane Fuel Cells
45. PFSA: Perfluorosulphonic Acid
46. ppm: parts per million
47. psi: pounds per square inch
48. PTFE: Poly(tetrafluoroethylene)
49. PyOH: 4-Pyridinol
50. q: Charge on ion
51. R: Resistance
52. RH: Relative Humidity
53. RT: Room Temperature
54. SANS: Small-Angle Neutron Scattering
55. SAXS: Small-Angle X-ray Scattering
56. S/cm: Siemen per Centimeter
57. SOFCs: Solid Oxide Fuel Cells
58. SSNMR: Solid State Nuclear Magnetic Resonanace
59. TG: Thermal Gravimetry
60. USABC: U.S. Advanced Battery Consortium
61. US-EIA: US Energy Information Administration

62. V: Voltage
63. V_0: Amplitude of the signal
64. V_t: Potential at time t
65. WAXD: Wide-Angle X-ray Diffraction
66. XRD: X-Ray Diffraction
67. YSZ: Yttria-Stabilized Zirconia
68. Z: Impedance
69. μ: Mobility of the charge carrier
70. φ: Phase shift
71. ω: Radial frequency
72. μ: Micron
73. σ: Ionic conductivity

Chapter 1

Chapter 1

Chapter 2

Chapter 3I

Chapter 3II

Included in thesis:

1. 1000-fold enhancement in proton conductivity of a MOF using post-synthetically anchored proton transporters; **S. Shalini**, V. M. Dhavale, K. M. Eldho, S. Kurungot, T. G. Ajithkumar, R. Vaidhyanathan; *Scientific reports*, **6**, *2016*, 32489.
2. 10000-Fold Enhancement in Proton Conduction by Doping of Cesium Ions in a Proton-Conducting Zwitterionic Metal–Organic Framework; ***S. Shalini***, S. Aggarwal, S. K. Singh, M. Dutt, T. G. Ajithkumar, R. Vaidhyanathan; *European Journal of Inorganic Chemistry*; **27**, *2016*, 4382.
3. Introducing high temperature anhydrous proton conductivity via post-synthetic modification; manuscript under preparation.

Not included in thesis:

1. Super-hydrophobic covalent organic frameworks for chemical resistant coatings and hydrophobic paper and textile composites; D. Mullangi, **S. Shalini**, S. Nandi, B. Choksi, R. Vaidhyanathan; *Journal of Materials Chemistry A*, **18**, *2017*, 8376. DOI: 10.1002/aenm.201600110.
2. Low-Overpotential Electrocatalytic Water Splitting with Noble-Metal-Free Nanoparticles Supported in a sp3 N-Rich Flexible COF; D. Mullangi, V. Dhavale, **S. Shalini**, S. Nandi, S. Collins, T. Woo, S. Kurungot, R. Vaidhyanathan; *Advanced Energy Materials*, **6**, *2016*, DOI: 10.1002/aenm.201600110.
3. Pd loaded amphiphilic COF as catalyst for multi-fold Heck reactions, C-C couplings and CO oxidation; D. Mullangi, S. Nandi, **S. Shalini**, S. Sreedhala, C. P. Vinod, R. Vaidhyanathan; *Scientific Reports*, **5**, *2015*, doi:10.1038/srep10876.
4. Lithium-Assisted Proton Conduction at 150˚C in a Microporous Triazine-Phenol Polymer; S. Nandi, V. M. Dhavale, **S. Shalini**, U. Werner-Zwanziger, H. Singh, S. Kurungot, R. Vaidhyanathan; *Advanced Materials Interfaces*, **2**, *2015*, 10.1002/admi.201500301.
5. Identifying Solid Luminogens through Gold-Catalysed Intramolecular Hydroarylation of Alkynes; A. C. Shaikh, **S. Shalini**, R. Vaidhyanathan, M. V. Mane, A. K. Barui, C. R. Patra, Y. Venkatesh, P. R. Bangal, N. T. Patil; *European Journal of Organic Chemistry*, **22**, *2015*, 4860.

6. Anion Driven [CuIIL2]n Frameworks: Crystal Structures, Guest-encapsulation, Dielectric and Possible Ferroelectric Properties; A. K. Srivastava, B. P. kumar, I. K. Mahawar, P. Divya, **S. Shalini**, R. Boomishankar; *Chemistry of Materials*, **26**, *2014*, 3811.

REVIEW:

1. Potentials of Ultramicroporous Metal Organic Frameworks in CO_2 clean-up; **S. Shalini**, S. Nandi, A. Justin, R. Maity R. Vaidhyanathan; *Chemcomm*, **54**, 2018,13472.

Chapter 1

Introduction

2018

1.1 Energy challenges in today's world

With the ever-increasing population, rapid urbanization and industrialization, especially in the developing countries, humanity's want for energy has reached unprecedented levels. U.S. Energy Information Administration's (EIA) recently released International Energy Outlook 2013 (IEO2013) projects claim that the global energy consumption will increase by 56% between 2010 and 2040[1]. Despite the adverse effects on the environment, fossil fuels continue to be the main source of energy. Their use releases an immense amount of greenhouse gases leading to global climate change. Fossil fuel retrieval, processing, their distribution and the power stations contribute to about 30% of the emissions. These emissions lead to pollution which has a detrimental impact on human health. Also, the mining and drilling for fossil fuels are expensive. Therefore, we need to look for alternative sources of energy. One of the alternatives can be nuclear power, but it has challenges associated with it like safety, radioactive waste disposal, and fuel availability. Also, the high initial capital costs limit its use as a viable energy source, especially for the developing countries. For example, the cost of building a power plant increased from $2-$4 billion to $9 billion per unit between the year 2002 to 2008. Even though it can help us make the world a better place, it can also lead to undesirable energy competitiveness. Energy production alternate to combustion of fossil fuels brings opportunities for both developed and developing nations[l]. Such alternatives include renewable energy sources such as solar, wind, tidal, hydroelectric and geothermal power. Although they are sustainable, provide clean energy and produce no or very little waste products, they rely on the weather and are not always geographically accessible. This impacts the reliability of the consistent energy supply. Also being very expensive, the technologies are still facing a lot of challenges[2]. It is also very difficult to generate the amount of electricity as large as produced by traditional power plants to meet the base power load. All this currently limits their use as energy sources. *So the most feasible and likely solution seems to efficiently store the renewable power while it is not being used and then dispense it at the time of need.*

1.2 Energy storage and conversion

The storage and delivery of energy for its utilization at the time of need is also challenging because of various concerns like the capacity, size, cost, and the efficiency of the method. For a technology to strive against the present fossil fuel based technology and be a

viable alternative, it should be cheap, have high efficiency, and provide high capacity for the required application. The storage of energy can either be done via physical, chemical or electrical methods. The physical storage involves the physical movement of objects for storing the produced energy as potential or kinetic energy and is not suitable for mobile applications[3]. Storing the energy in molecular bonds of fuel and releasing it through combustion is how the chemical storage of energy works and is very widely used. The internal combustion engine (ICE) run by fuels like gasoline, methane, and diesel is a typical example. Although it provides high energy densities (6 kW·h/kg) and the storage and transport of fuels are easy, the discharge of the enormous amount of greenhouse gases result in the change in climate globally. Also, ICE has an efficiency of only 30%[4]. Another approach, i.e., the electrical method uses electrochemical or electrical conversion devices like batteries, fuel cells or capacitors. Capacitors are used to store electric charge using electrodes separated by an insulating material. They have a long lifetime, high discharge rates and power densities and thus can provide a large burst of power in a short time, but because of their low energy densities, they are not suitable for the applications involving transportation[4]. In contrast, batteries have higher energy densities but reduced power densities because of their sluggish kinetics[4]. Although their cost is decreasing with the increasing demand, the long battery recharge time is a major drawback. *The fuel cells (FCs), which have shown great promise for mobile applications, convert the chemical energy of fuels directly into electrical energy and produce water and heat as byproducts*[5]. This thesis focuses on developing electrolyte materials for fuel cells, so the fuel cells would be described in depth in the following section.

1.3 Fuel Cells

In 1839 Schoenbein published his first observations that the charged platinum wire lost its charge when immersed in an atmosphere of oxygen or hydrogen[6]. This principle laid the foundation for the fuel cell. At the same time, W.R. Grove reported the first hydrogen fuel cell which used platinum electrodes and sulfuric acid as an electrolyte[7,8]. The study for developing fuel cells moved forward with great vigor until the 1950s when NASA started developing Alkaline Fuel Cells (AFCs) and PEM FCs for the Gemini and Apollo space programs because they could provide power as well as drinking water for astronauts[9,10]. This was then followed by extensive research on Nafion, the polymer electrolyte membrane, in the 1970s by Walther Grot

of Dupont Corporation[11,12]. Till date, Nafion remains the commercially used material and will be discussed in detail in section 1.3.4.1. Following this, mainly due to a small market and the high cost of FCs, the research and progress slacked off until the advancement of decreasing the loading of platinum catalyst helped envision a lot cheaper cells in the 1980s[9].

1.3.1 Desirability of fuel cells

Fuel cells are being extensively studied due to their advantages such as high conversion efficiency, low pollution, and high fuel flexibility[13-15]. They combine the advantages of an ICE (rapid chemical energy storage) and a battery. They are similar to ICE as they use chemically stored energy in the form of a liquid or gaseous fuel which can be easily refilled making them valuable for continuous operations. But unlike internal combustion engines, their efficiency is not constrained by the thermodynamics of the process as they rely on electrochemical conversions for producing the energy, and therefore are more efficient. Also, Fuel cells mainly use hydrogen as fuel which is abundant, more efficient, clean and non-toxic[16]. When compared to a battery, fuel cells have higher specific energy (energy per unit weight; Figure 1.1.) and therefore can provide electricity with ~ 8-14 times less weight than the current batteries and four times less than the U.S. Advanced Battery Consortium (USABC) goal[17].

They are proving to be superior because of their less weight, compactness, low operating temperatures, less greenhouse gas generation, non-corrosion, and sustained operation at a high current density and less time required to refuel. Therefore the fuel cells are being viewed as an important alternative to produce and store energy via electrolysis and are finding applications in portable electronics, electric vehicles (EV), and large-scale stationary power generation applications[18-22]. As a result, many companies are commercializing FCs for various applications. Some of them are Ballard Power Systems, Versa Power Systems, UTC Power Corporation, Toyota, Honda, and Mercedes-Benz[9].

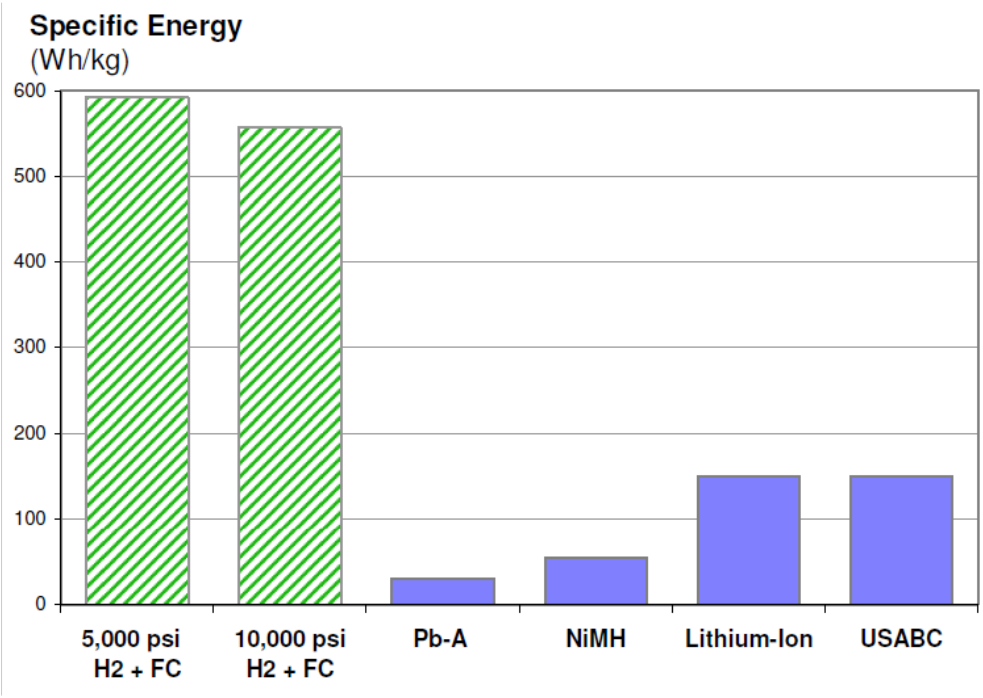

Figure 1.1. Comparison of the specific energy of a Polymer Electrolyte Membrane (PEM) fuel cell compressed with hydrogen to the specific energy of lead-acid (PbA), nickel metal hydride (NiMH), Lithium Ion batteries and the USABC goal. Two hydrogen pressures are shown: 5,000 psi and 10,000 psi with fiber wrapped composite tanks. (Adapted from ref. 17)

1.3.2 Working of Fuel Cells

Fuel cells (FCs) are electrochemical conversion devices that produce electrical energy from the chemical energy of a fuel and oxygen at high thermodynamic efficiencies[23]. Many configurations of a fuel cell are possible (see section 1.3.3) depending on the fuel and electrolyte used, but the basic working principle is same and therefore PEM fuel cell using hydrogen as fuel, and a proton-conducting polymer electrolyte will be used to explain the general operating principle.

The core components of FCs are the two electrodes (anode and cathode) and a proton-conducting polymer electrolyte membrane (Figure 1.2). In addition to that, the fuel cell assembly also consists of a cooling system, humidity chamber, and a water management system. The fuel, i.e., hydrogen and an oxidant (oxygen) generally from ambient air is continuously diffused to the electron conducting, porous anode and cathode respectively. At the anode, which is typically loaded with platinum catalyst, electrons and protons are produced by splitting hydrogen atoms at

the interface of the electrolyte, catalyst, and pores[24]. The polymer electrolyte membrane being permeable to protons let them pass through and reach

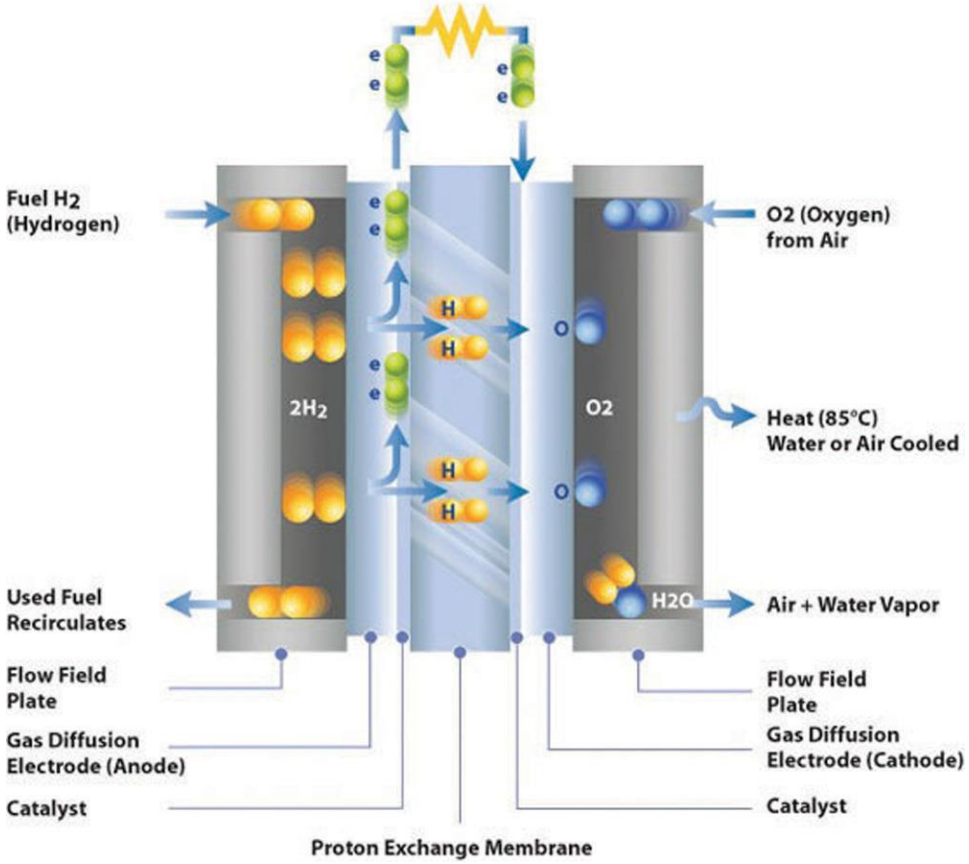

Figure 1.2. A basic schematic representation of a PEM fuel cell. (Adapted from http://www.climatetechwiki.org/technology/mobile-fuel-cells)

cathode but restricts the passage of electrons. The electrons are thus transported to the cathode via an external circuit, where they reduce oxygen. At the cathode, protons combine with oxygen to produce water. In a nutshell, the fuel cells combine hydrogen and oxygen to produce clean electricity as the main product and water as a by-product (equation 1.1)[5].

Anode: $H_2 \rightarrow 2H^+ + 2e^-$

Cathode: $1/2O_2 + 2H^+ + 2e^- \rightarrow H_2O$

Overall: $H_2 + 1/2O_2 \rightarrow H_2O$ **….Equation 1.1**

1.3.3 Types of fuel cells

Depending on the type of electrolyte and fuel used, FCs are divided into five namely Molten Carbonate Fuel Cells (MCFCs), Phosphoric Acid Fuel Cells (PAFCs), Solid Oxide Fuel Cells (SOFCs), Alkaline Fuel Cells (AFCs) and Proton Exchange Membrane Fuel Cells (PEMFCs) (Table 1.1)[5,24].

Table 1.1. Selected Characteristics of five major types of fuel cells. Power density, being an important factor, is shown in bold.

Type of fuel cell	**Electrolyte used**	**Operating Temperature (˚C) and Power Density (mW/cm^2)**	**Possible Fuels**	**Advantages**	**Challenges**
Solid Oxide (SOFC)	Ceramic	600-1000˚C **250 – 350 mW/cm^2**	H_2, CH_4, CO, alcohols, hydrocarbons	Fuel flexibility. Can use a variety of catalysts.	Corrosion, the breakdown of components. Long startup time.
Molten Carbonate (MCFC)	Molten Li_2CO_3/ K_2CO_3	600-700˚C **100 – 300 mW/cm^2**	H_2, CH_4, CO, small chain alcohols and hydrocarbons	High efficiency. Fuel flexibility. Can use a variety of catalysts.	Corrosion, the breakdown of components. Long startup time. Low power

					density
Phosphoric Acid (PAFC)	Liquid phosphoric acid	150-200˚C **150 – 300 mW/cm^2**	H_2	Increased tolerance to impurities	Pt catalyst. Long start up time.
Alkaline (AFC)	Liquid KOH	90-100˚C **150 – 400 mW/cm^2**	H_2	Faster cathode reaction in alkaline electrolyte, high performance, and low-cost components	Electrolyte management and sensitive to CO_2 in fuel and air
Polymer Electrolyte Membrane (PEMFC)	Nafion	50-100˚C **300 – 1000 mW/cm^2**	H_2, Methanol	Reduced corrosion and electrolyte management problems. Quick startup.	Expensive catalyst and sensitive to fuel impurities

Solid Oxide Fuel Cells (SOFCs)

SOFCs use perovskites or yttria-stabilized zirconia (YSZ, ceramic electrolytes). They are operated at high temperatures and the conduction happens via oxide anions[24,25]. They are therefore also called high-temperature fuel cells. Because they are used at higher temperatures, they are significantly cheaper as the expensive platinum is replaced with nickel. They have high electrical efficiency (50 to 60%) because the need of a separate reformer to form hydrogen from the fuel is bypassed. However, the operation at high temperatures brings in challenges regarding material stability[26]. Other drawbacks include slow startup and intolerance to the sulfur content of the fuel cell. SOFCs are thus only suited for stationary high power applications, where the waste heat can also be used to produce additional electricity[27,28].

Molten Carbonate Fuel Cells (MCFCs)

MCFCs also operate at high temperature, have CO tolerance, and fuel flexibility. They use inexpensive catalysts, but they use different electrolyte, i.e., a mixture of molten lithium carbonate and potassium carbonate. They use the carbonate anion instead of oxide ion as the charge carrier. This produces CO_2 at the anode which is then used as a reactant at the cathode. Therefore this type of FC requires an extra CO_2 recycling system. The overall reaction is as follows (equation 1.2):

Anode: $H_2 + CO_3^{2-} \rightarrow CO_2 + H_2O + 2e^-$

Cathode: $\frac{1}{2} O_2 + CO_2 + 2e^- \rightarrow CO_3^{2-}$ **…Equation 1.2**

Just like SOFCs, they are also suited for stationary applications with constant power supply, but they have a shorter life because carbonate electrolyte is very corrosive in nature.

Phosphoric Acid Fuel Cells (PAFCs)

PAFCs use phosphoric acid as an electrolyte in the form of concentrated aqueous solution embedded in an inert matrix such as silicon carbide[24]. The operating temperature for these cells is limited to below 200˚C[29]. They use H_2 as a fuel and have very moderate resistance to CO impurities. They have an electrical efficiency of 40%. These cells do not find many commercial applications owing to the corrosive and volatile nature of phosphoric acid electrolyte and low power densities. However, they have been developed to the first stage of commercialization, and the 100, 200 and 500 kW size plants are available for stationary and heat applications[30].

Alkaline Fuel Cells (AFCs)

The alkaline fuel cell is one of the earlier fuel cell systems which were employed in NASA's space missions. It is also known as Bacon fuel cell after the inventor. The operating temperature is around 100˚C just like the PEMFC, and they have an efficiency of ~60–70%. Potassium hydroxide (KOH) is used as an electrolyte to transport negative ions from one electrode to another. These fuel cells give quick startup but are very sensitive to CO_2 as it takes a lot of time to react and thus consumes the electrolyte and reduces the concentration of hydroxide

ion required for the chemical reaction[27,31]. Also, the corrosive electrolyte lowers the lifespan of the FC. They are mostly used in fleet vehicles, boats and space shuttles.

Proton Exchange Membrane Fuel Cells (PEMFCs)

PEMFCs normally use 10-200 μm thin electrolyte membranes which facilitate the easy exchange of protons. They typically are acidic organic polymers. These proton exchange membranes (PEM) rely on the presence of water to help form proton conducting pathways; a feature that limits the use of these FCs below the boiling point of water, i.e.,100°C. PEMFCs have electrical efficiency of 40–60%. These advantages make them the most studied systems for a lot of applications. They use costly platinum catalyst and because they operate at low temperatures, the biggest problem arises from a phenomenon called 'CO poisoning' of the catalyst as soon as the CO concentration increases more than 20 ppm. Therefore these FCs require the use of pure fuel sources, increasing the operational costs[32]. However, because of the the same fact that they work at low temperatures, the shutdown and the start-up of these FCs are made easier. This means that the electrolytes which can perform at high temperatures need to be developed[32,33-36]. Operation of FCs above 100°C would also mean that the electrode reaction kinetics, especially for the oxygen reduction reaction, will become more favorable[32]. Second, FC operation above 100°C would produce water only in the vapor phase which will decrease the likelihood of flooding of the FC[32-34]. Also, it is easy to manage the heat that is produced in the process. Finally, the operation of the FC at high temperature will open up the possibility of using cheaper catalysts, which in turn, will make the FCs cheaper[32]. In order to attain all these prospective benefits various new electrolytes need to be developed. The challenges that need to be addressed in PEMFCs are shown in table 1.2[37].

Table 1.2. Current (2016) challenges of Polymer Electrolyte Fuel Cells

Task	**Approach**
Catalysts/Electrodes	• Optimize electrode design and assembly • Develop electrocatalysts and electrodes with reduced platinum group metal loading, increased activity, and improved durability/stability.
Membranes/Electrolytes	• Develop/identify electrolytes and membranes/matrices with improved conductivity over the entire temperature and humidity range of a fuel cell and increased mechanical, thermal and chemical stability with reduced/eliminated fuel crossover. • Fabricate membranes from ionomers with scalable fabrication processes
Membrane Electrode Assemblies (MEA), Cells and other stack components	• Integrate membranes, electrolytes, and electrodes. • Expand the MEA operating range, improving stability, and mitigating effects of impurities. • Test, analyze and characterize MEAs

The work in this thesis deals with developing electrolytes/membranes for the PEMFC, and therefore only the electrolytes part would be discussed in detail in the sections ahead.

1.3.4 Electrolytes for PEMFCs

Proton conducting materials have attracted a lot of research attention due to their applications in FCs, electrochemical sensors, and reactors[38-43]. A large number of materials have been researched and reported in the literature to be used as electrolyte materials. Non-fluorinated polymers mainly hydrocarbon-based, and acid-base complexes have been studied to address the shortcomings of perfluorosulphonic acids (PFSA)[33,44-47]. Organic compounds containing acidic moieties or nitrogen functionalities such as imidazole and triazole have also been researched for proton conduction, mainly at high temperature, and humidity-free conditions. Imidazole and

triazole, by themselves, are very poor proton conducting materials. They conduct at 10^{-8}-10^{-7} S/cm and 10^{-5} S/cm respectively in their solid state and have a proton conductivity of 10^{-3} S/cm in their molten state[48,49]. They are unstable under FC operating conditions and thus cannot be used for practical applications. Their performance has been improved by anchoring these azoles on different polymers. Using this strategy, researchers have achieved moderate conductitvity values of 10^{-5} S/cm at temperatures above 100˚C and 0% humidity[49-51]. Other organic molecules like carboxylic acids have been researched too for the same[52]. Recently organic sulphonates[33], imidazole, and pyrazole[53,54] have been used as additives in polymers to produce novel materials with appealing proton-conducting properties[55,56]. In addition to this, proton conduction in extended crystalline networks is still challenging. Mainly, two kind of inorganic electrolytes; polyoxometalates and solid acids have been found to show moderate proton conductivities of 10^{-4} to 10^{-1} S/cm[57-61]. There are other examples like $CsHSO_4$ and its family[62]. $CsHSO_4$ is a good proton conductor but is soluble in water and therefore cannot be used in FCs[63].The $CsHSO_4$-composite materials like $CsHSO_4$–SiO_2 and CsH_2PO_4–SiO_2[64-65] show good proton conductivity.

Although a huge variety of systems have been evaluated, the nafion despite being discovered in the 1970s is still the commercially used proton conducting electrolyte.

1.3.4.1 Nafion

Nafion[67-69] is the commercially used electrolyte in the PEMFCs. It was discovered by DuPont in the 1960s[70]. It is a tetrafluoroethylene based fluoropolymer-copolymer terminal sulphonic acid groups (Figure 1.3). The fluorinated backbone provides it its chemical stability whereas the sulphonic acid acts as a proton source[71]. It has a high proton conductivity of 10^{-1} to10^{-2} S/cm at 85°C with varying humidity[71], but the conductivity depends on the temperature and humidity conditions, membrane preparation and the equilibration time[72]. Nafion has achieved great success because of its robust structure, excellent thermal and mechanical stability, high proton conductivity and reusability without any significant loss of activity. Importantly, the high affinity of sulfonate to water and the poor affinity to the fluorinated backbone favor facile water dynamics which means shortened equilibrium time.

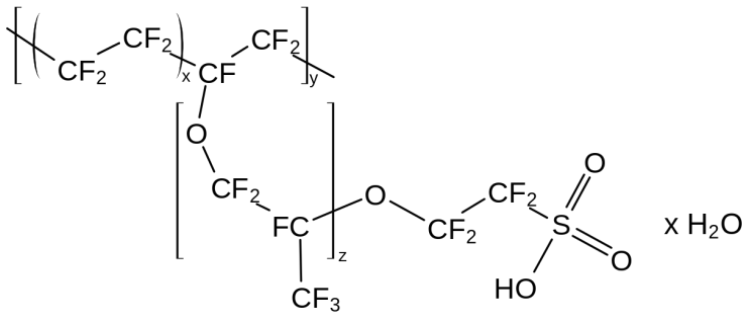

Figure 1.3. Chemical structure of Nafion.

The fact that the Nafion is amorphous makes the understanding of the conduction mechanism very difficult, but researchers have agreed upon a model that there are two different domains formed by the self-segregation of sulfonic acid groups (hydrophilic domain) and the fluorinated backbone (hydrophobic domain). Using small-angle X-ray scattering (SAXS), small-angle neutron scattering (SANS), and wide-angle X-ray diffraction (WAXD), many researchers have proposed a plethora of models[73]. Schmidt-Rohr and Chen[74] reported a model where they proposed the structure of Nafion being made up of long and parallel inverse micelles (Figure 1.4). These inverse micelles were claimed to be cylindrical (1.8-3.5 nm in diameter at 20 vol% water) in nature, filled with water and lined with terminal sulfonic acid groups. Because of the hydrophobicity of the fluorinated backbone, elongated crystallites having a cross-section of ~5 nm^2 running parallel to the water channels are formed. When dehydrated, these channels reduce in size or shrink thereby decreasing the proton conductivity.

Despite Nafion being very widely used, there are a lot of issues that need to be addressed such as the high cost, its humidity dependence, and low operation temperature (lower than 80°C). The dependence on humidity is the major drawback for it to be used as an electrolyte because it requires an external humidification chamber to maintain the constant conductivity values, and this leads to the decrease in the fuel cell efficiency on the whole. This also implies that these FCs are restricted to operate below the water's BP and therefore the operation of FCs, at present, is limited to below 85°C. The Nafion membrane, itself, can not be used at higher temperatures as its performance declines with the increase in temperature above 100˚C[75].

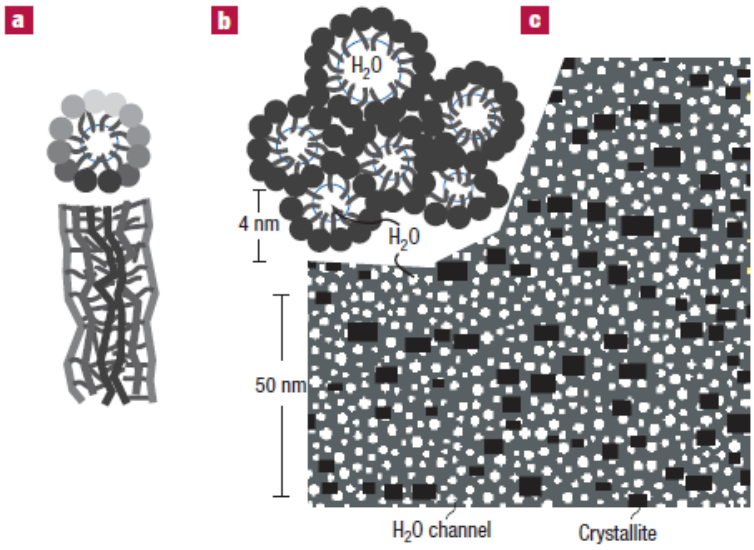

Figure 1.4. The 'Parallel water channel/inverted-micelle cylindrical' model of Nafion as proposed by Schmidt and co-workers. (a) Two views of an inverted-micelle cylinder. (b) Schematic showing the hexagonal packing the micelle cylinders. (c) Cross-sections through the cylindrical water channels and nafion crystallites represented in white and black respectively. (Adapted from ref. 74)

Bouzek and co-workers showed that this decrease isn't due to the chemical degradation of the membrane but is due to the increase in the amorphous domains and the decrease of the pseudo-crystalline domains in the polymer above its glass transition temperature (117˚C)[76]. Because at higher temperatures, the polymer contains a larger fraction of amorphous phase, it is more prone to swelling in a humid environment. The presence of hydrophilic groups, in fact, assists this swelling. Still, the effect of the structure change cannot be ruled out. Zhu and co-workers reported that the membrane stretching changes the orientation of the conductivity channels and thereby affects the overall membrane conductivity[77,78]. Also, as already discussed, the amorphous nature of the polymer makes the optimization of the proton transport pathway and the characterization of the conduction behavior very difficult. The use of this polymeric conducting membrane is also very questionable in direct methanol FCs because of its permeability to methanol which decreases the efficiency of the FCs significantly[79-84]. Therefore, it is imperative to develop cheaper, designable and better performing solid/gel electrolytes, though it is challenging. It is critical to the technological advancement of automotive applications that can work from very high to sub-zero temperature[71].

1.4. Designing an electrolyte material

When designing or developing an electrolyte in FCs, one needs to keep certain features in mind that need to be incorporated in it[16]. First and foremost, the material should possess high proton conductivity, i.e., values greater than or equal to 10^{-2} S/cm[9,85]. In addition to being highly proton conductive, it should simultaneously be electronically insulating to block the transfer of electrons across the electrolyte membrane to avoid the lowering of the overall efficiency of the system[44]. It should have low membrane resistance and a very effective way to reduce it is to use a thinner membrane. For example, initially in the fuel cells, Nafion117 with a thickness of 175–183 µ was employed, followed by Nafion115 and Nafion112 with a thickness of 127 µ and 51 µ respectively. Currently, Nafion211 or Nafion111 with 25 µ thickness are being used. However, decreasing the membrane thickness poses another problem, i.e., fuel crossover. This becomes a limiting factor especially at low current densities and therefore, necessitates studying the material for hydrogen at higher temperatures where the H_2 crossover is more dominant[86]. So it should also have the ability to restrict the oxidant's and the fuel's flow across the cell[9]. Hydrogen crossover normally has three undesirable effects which include a decrease in the efficiency of the system, depression in the cathode potential, and formation of peroxide radical. The hydrogen crosses over and comes in direct contact with oxygen at cathode which results in a lower cathode potential[87]. Also, the direct and highly exothermic reaction between hydrogen and oxygen produces peroxide radicals, which severely attack the catalyst as well as the membrane[88-90]. Also, the formation of pin-holes and hot points in the membrane destroys the membrane electrode assembly (MEA) due to the enormous heat produced during this reaction[91]. The electrolyte material, therefore, must have the chemical, mechanical and thermal stability under the FC operating conditions[9,44]. Also, it should have a long lifetime. According to the US-DOE 2015 target, a material used in the FC should be able to run a vehicle for at least 5,000 hours[9]. Fourth, the electrolyte material must have the ability to be integrated into a FC, preferably in the form of a membrane. Most importantly, the material should conduct protons at higher temperatures. This feature brings an additional advantage, i.e., decrease in the operational cost of the FC. Operating a FC at high temperatures can help replace the expensive platinum catalyst with inexpensive transition metal-based catalysts, which typically have sluggish redox kinetics at ambient temperatures[92]. In fact, the rate of electrode reactions almost doubles with every 10˚C increase in temperature[92].

As already discussed in section 1.3.4., a large number of materials have been studied for the application of proton conductivity, and a detailed discussion of all the systems is beyond the scope of this thesis. Lot more details can be found in abundant review articles published on the subject[9,32-35,44,57,60,93-98]. Metal-Organic Frameworks will be introduced in the next section, in the context of their use for proton conducting applications, which will then be followed by an in-depth discussion of the Proton Conducting MOFs (PCMOFs) available in literature.

1.5. Metal Organic Frameworks

Metal Organic Frameworks (MOFs) or Porous Coordination Polymers (PCPs) are coordination framework compounds formed by linking metal ions/clusters via organic linkers and have emerged as a new class of functional materials[99-101]. They possess large surface area, ordered crystallinity[102-107], structural flexibility and diversity, tunable pore size and their pores can easily be functionalized. Due to these features, MOFs find their use in various applications such as catalysis[108-119], gas storage[120-137], separation[138-153], sensing[154-158], photoluminescence[159-165], energy storage & conversion[166-172], electrical conductivity[173-177], and proton conductivity[178-186]. MOF's striking properties like chemical stability, hybridization with other materials, and material fabrication make them ideal candidates for proton-conducting applications. Owing to their modular structure, proton carriers or protic species can easily be moduled into their frameworks and/or in the channels to alter the proton conducting properties. Also, the crystalline nature facilitates the study of the proton conduction mechanism and pathway[187].

Generally, the proton conductivity of a MOF is tuned by either increasing the proton mobility and/or the proton concentration also by altering the intrinsic acidity via a choice of functional groups[188]. This has been shown by Hiroshi and coworkers[189] and Susumu and coworkers[190]. Shimizu and coworkers[191] in 2009 reported a proton-conducting MOF (β-PCMOF-2) where the channels were occupied by 1H-1,2,4-triazole (Tz). It is made up of the sulfonate ligand, 2,4,6-trihydroxy-1,3,5-benzenetrisulfonate. The hexagonal sheets of the ligand in the ab plane are cross-linked by Na ions in the c-axis to form channels lined solely with oxygen atoms of the sulfonate groups. It exhibited proton conductivity of 5×10^{-6} S/cm at 30˚C and 1×10^{-8} S/cm at 70˚C. The conductivity was enhanced by loading triazole molecules into the 1-D channels of β-PCMOF-2. β-PCMOF-2$(Tz)_x$ were prepared with different loadings of triazole (x=0.3, 0.45, and 0.6). Despite of the amount of the triazole loaded in the MOF, the proton

conductivity of Tz@β-PCMOF-2 at 150˚C was in the range of 2–5 x 10^{-4} S/cm under anhydrous conditions. The conductivity of Tz@β-PCMOF-2 was higher than of either β-PCMOF-2 or triazole.

Ghosh and coworkers in 2014[179], reported a 3-D oxalate based MOF, $\{[(Me_2NH_2)_3(SO_4)]_2[Zn_2(ox)_3]\}_n$ (Figure 1.5). The pores of the MOF were filled with acid-base to set up an efficient proton conducting pathway and thus enhancing the proton mobility. The structure has an anionic $[Zn_2(ox)_3]_n^{2-}$ framework interpenetrated with $[(Me_2NH_2)_3SO_4]_n^{+}$ supramolecular net formed by electrostatic interactions between dimethyl ammonium (DMA) cations and sulfate anions. It has a humidity-dependent conductivity of 4.2 x 10^{-2} S/cm at 25˚C and 98% relative humidity (RH) and an anhydrous conductivity of 1 x10^{-4} S/cm at 150˚C.

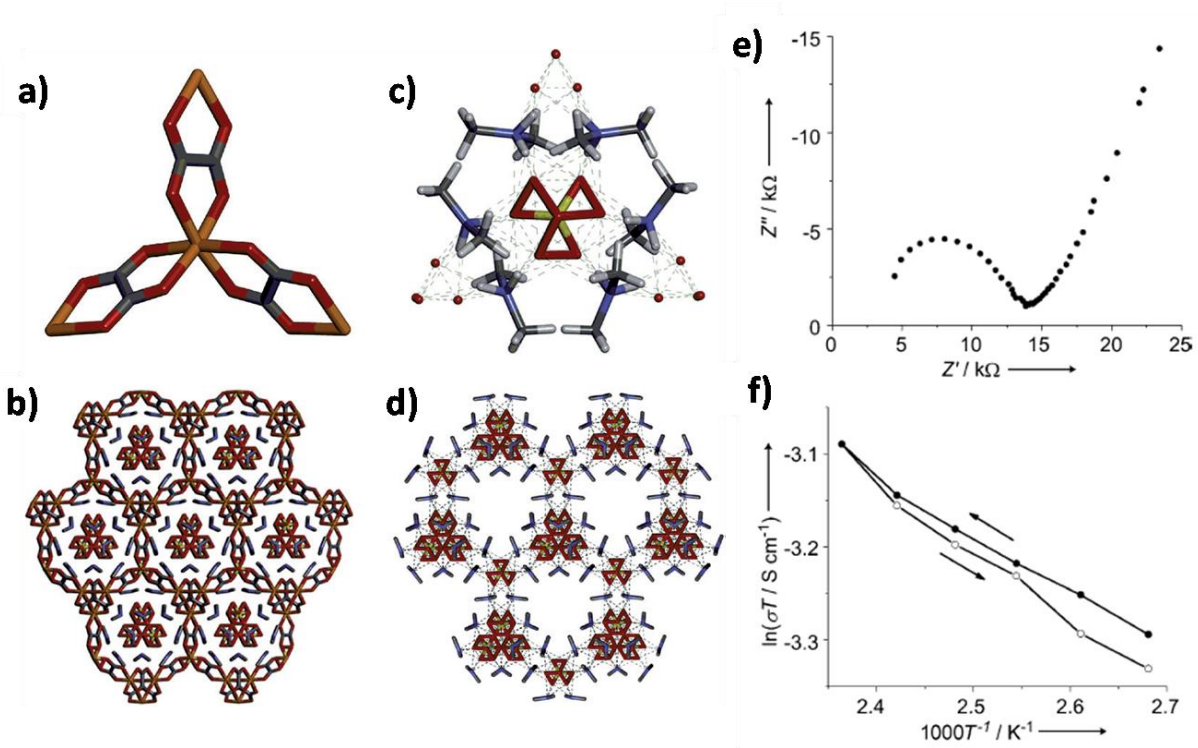

Figure 1.5. (a) The tris-chelated $[Zn_2(ox)_3]^{2-}$ unit. (b) 3D framework of $\{[(Me_2NH_2)_3(SO_4)]_2[Zn_2(ox)_3]\}_n$. (c) Figure showing the hydrogen bonding between DMA cations and sulfate anions. (d) 3D supramolecular $[(Me_2NH_2)_3SO_4]_n^{+}$ net formed by acid-base pairs. (e) Nyquist plot for the MOF at 150˚C under anhydrous conditions. (f) Arrhenius plot for the MOF; heating cycle (open circle) and cooling cycle (closed circle). (Adapted from ref 179)

Hong and coworkers[192] reported a very stable MOF, UiO-66$(SO_3H)_2$, which has a conductivity of 8.4 x 10^{-2} S/cm at 80˚C and 90% RH, the highest value among the reported MOFs under similar conditions employed. Their strategy involved an increase in the concentration of the protons in the framework by post-synthetic oxidation of the thiol groups of UiO-66$(SH)_2$ (Figure 1.6). The thiol groups were converted to sulfonic acid groups which were anchored on to the backbone of the MOF. The high conductivity resulted from the presence of strong Brønsted acid sites (SO_3H groups) on the organic ligands. These acidic groups favor adsorption of water molecules establishing favorable proton-transport pathways, very similar to that observed in the commercially used Nafion.

Mainly, two types of proton-conducting MOFs have been studied[71,85,184,188,193,194]:

1. MOFs having water assisted proton-conduction at low temperature (20–80˚C).
2. MOFs having anhydrous proton conduction at a higher temperature (100–250˚C), where the water is replaced with high boiling, amphiprotic guests.

The following sections discuss the recent advancements in MOFs concerning their proton conducting behaviors. A wide variety of MOFs such as sulphonate-carboxylate-based MOFs[195-200], phosphonate-based MOFs[185,201-205], oxalate-based MOFs[206-212], carboxylate-based MOFs[192,213-223], and other mixed-linkers-based MOFs[224-227] have been reported for proton conduction. Carboxylate groups coordinate strongly with metal center forming pretty stable MOFs whereas sulphonate groups having weaker coordination ability can be retained, thereby,

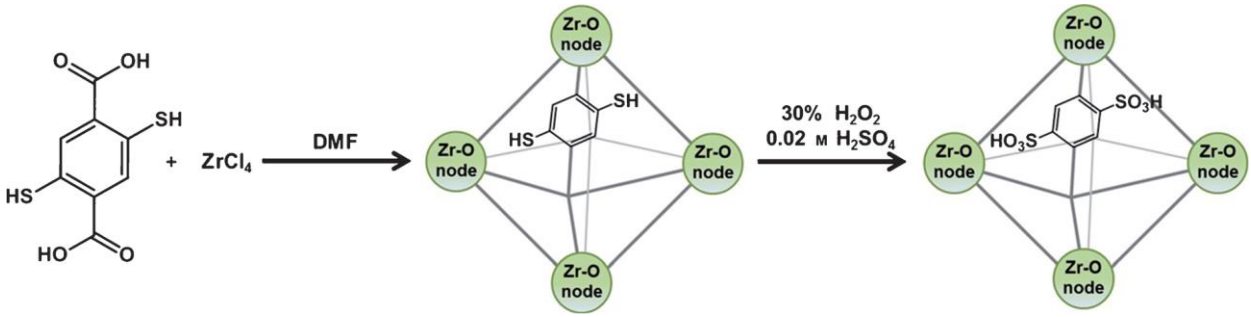

Figure 1.6. Synthesis of UiO-66$(SH)_2$ and post-synthetic oxidative modification of UiO-66$(SH)_2$ to UiO-66$(SO_3H)_2$. DMF=N,N-dimethylformamide. (Adapted from ref. 192)

When compared with carboxylate ligands, phosphonate groups have several advantages in terms of acidity and stability. The majority of reports focus on using one type of ligand, however, using

two or more types of ligands provide many other opportunities. The mixed ligand systems can afford functionalized proton conducting channels, providing flexibility for designing proton-conducting materials. ***The work in thesis deals with mixed oxalate-based and terephthalate-based MOFs having amphoteric moieties in the framework/pores, therefore, what follows is a detailed review of the known oxalate and carboxylate-based MOFs for proton conduction.***

1.5.1. MOFs having water assisted proton-conduction

Oxalate based MOFs

Oxalate-based MOFs form a wide variety of structures, such as one-dimensional straight or zigzag chains[228], two-dimensional honeycomb sheets, and three-dimensional quartz like structures. Out of the three, honeycomb $[M_2(ox)_3]$ structures show high proton conductivity and have attracted a lot of interest[189,211,229,230]. One of the main reasons for the high conductivity is that these structures form as anionic frameworks and therefore, the proton donor can be introduced as counter-cations in the framework. The $[M_2(ox)_3]$ frameworks also have a lot of oxygen atoms which make extensive hydrogen bonds with the adsorbed water in the frameworks. Therefore, $(NH_4)_2[Zn_2(ox)_3](adp).3H_2O$ shows high proton conductivity.

In a recent report, a dense metal organic framework, $(dma)_2[Li_2Zr(ox)_4]$ with ox = oxalate and dma = dimethylammonium)[207] was reported to show an abrupt increase in the value of proton conductivity. It increases from $<10^{-9}$ to 3.9×10^{-5} S/cm at 17°C when exposed to humidity. It has an activation energy of 0.64 eV. The conductivities measurements were done on single crystals. The as-synthesized MOF is highly insulating till ~50% RH, with conductivity even less than the detection limit of the instrument ($\sim 10^{-9}$ S/cm). The initial structure then transforms to a dense structure on humidification via topotactic hydration ($H_2O/Zr = 0.5$), where $1/4^{th}$ of the Li^+ are irreversibly rearranged and coordinated with water molecules. The hydrous structure then further transforms to a third crystalline structure ($H_2O/Zr = 4.0$). The authors relate the reversible increase in conductivity with the reversible structure transformation. The water molecules bound to Li^+ formed in the first step, act as the proton source, and the absorbed H_2O molecules formed in the second step of transformation, act as proton carriers. The structure and composition of phase II were determined via single-crystal diffraction. The composition was found to be $(dma)_2[Li_2(H_2O)_{0.5}Zr(ox)_4]$. One water molecule is added to one of the four Li^+ to form II from I

(Figure 1.7), which increases the coordination number from 4 to 5. Both I and II have 1-D square-shaped channels which are formed by $[Zr(ox)_4]^-$ anions connected by the Li^+ (Figure 1.7 a, e) and filled with dma cations leaving no significant pores. On hydration, Li binds the water molecule (Figure 1.7 b) and forms a chain of edge-sharing LiO_5 units (Figure 1.7 f,g). Simultaneously, half of the $[Zr(ox)_4]^{4-}$ and Zr rotate for the structure to retains the square channels(Figure 1.7 b).

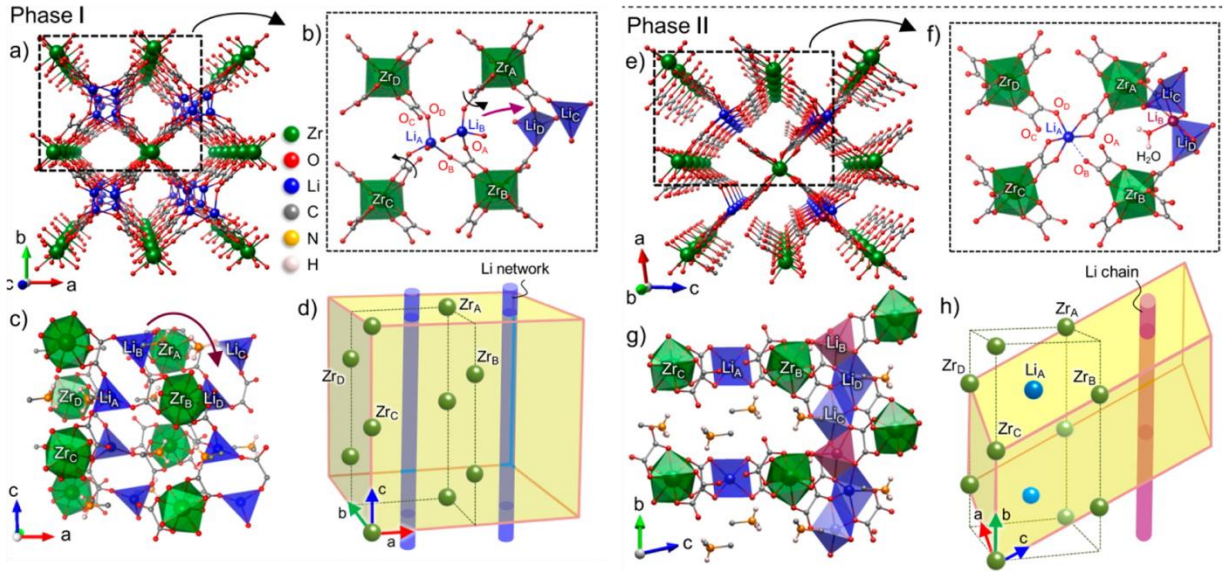

Figure 1.7. Topotactic hydration and transition of phase I (a–d) to phase II (e–h). (a, e) The figure shows the 1-Dsquare shaped channels in the framework. (b, f) Shows the rotation of Zr polyhedral which is triggered by the hydration of Li. In phase II, the hydrated Li is shown in red. (c, g) the side view of the channels showing dma cations. (d, h) Crystallographic orientation relationships. The unit cell is shown in yellow and cuboids formed by chains of Zr polyhedra are shown in black dotted line. (Adapted from ref. 207)

In one of the very earlier reports, Kitagawa and coworkers[189] proposed three kinds of rational designs to incorporate proton carriers in MOFs.One, by simply introducing them directly as counter-ions such as H_3O^+, NH_4^+, and HSO_4^- in the pores of the MOFs (type I), second by incorporating proton bearing acidic groups in the frameworks (type II), and third by introducing acidic moieties into the voids of the MOFs (type III). The authors constructed a highly proton-conducting MOF, $(NH_4)_2(adp)[Zn_2(ox)_3].3H_2O$ (adp =adipic acid, ox = oxalate) by introducing protons in the form of NH_4^+ in addition to water molecules into the voids of an anionic, layered oxalate framework, $[Zn_2(ox)_3]_2^-$ (Figure 1.8). They adopted a combination of type I (introducing

NH_4^+ as counter cations) and type III (introducing adipic acid in the voids). This strategy helped them achieve a super-protonic conductivity of 10^{-2} S/cm at ambient temperature, which is comparable to nafion.

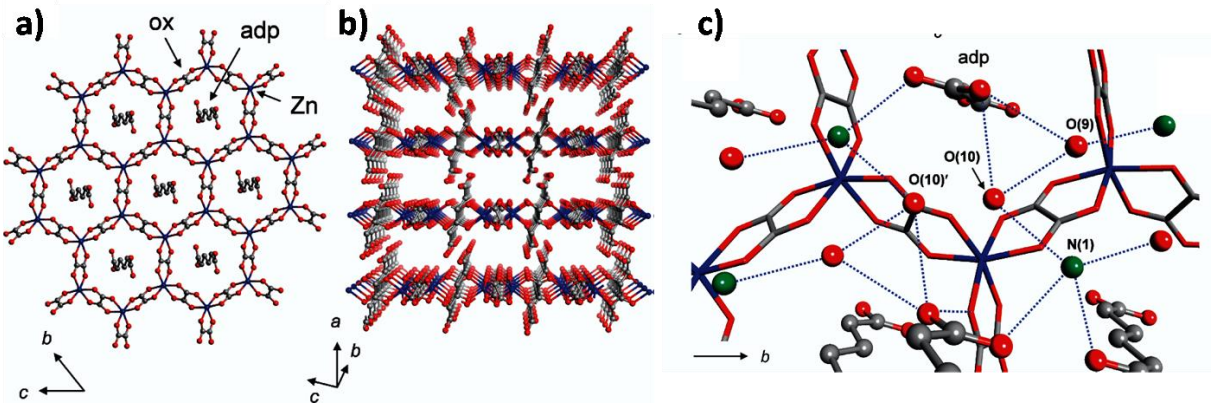

Figure 1.8. (a) Honeycomb layer structure of the MOF. (b) View along the b-axis. For clarity, the guest molecules have been omitted. (c) Hydrogen-bonding between -COOH, H_2O, and NH_4^+ is shown in blue dotted lines. Colour code: Red: oxygen, green: nitrogen, gray: Carbon and blue: Zinc. (Adapted from ref. 189)

The authors later reported a work[209] using the same material focusing on the control of conductivity by varying the guest molecules to understand the relationship between conducting pathways and the proton conductivities (Figure 1.9). Because $(NH_4)_2(adp)[Zn_2(ox)_3].nH_2O$(ox: oxalate, adp: adipic acid, n = 0, 2, 3) can show reversible structural transformations between the anhydrate, dihydrate, and trihydrate phases, the authors could easily study the effect of hydrogen bonding pathway on the proton conduction. NH_4^+, H_2O, and carboxylic groups of adipic acid form hydrogen bonding in the dihydrate and trihydrate. Water plays an important role in influencing the proton conductivity by reforming and rearranging hydrogen-bonded networks through water adsorption/desorption processes. Proton conductivity could be controlled in the range of $\sim 10^{-12}$ S/cm for anhydrate to $\sim 10^{-2}$ S/cm for the trihydrate by varying the humidity and number of water molecules in the structure.

Proton conductivity in this MOF could also be controlled by cation substitution[210]. The ammonium ions were substituted with potassium ions to form $K_2(H_2adp)$-$[Zn_2(ox)_3].3H_2O$, wherein a very well defined hydrogen-bonded pathway was interrupted by non-hydrogen-bonding K^+. This substitution didn't cause any apparent change in the structure of the MOF. The

proton conductivity could successfully be controlled by disrupting the proton-conducting pathway, implying that the two-dimensional hydrogen-bonding networks in the system truly contribute to the proton conductivity. The proton conductivity decreased to 1.2×10^{-4} S/cm at 98% RH and 25°C, which is two orders of magnitude lower than that of the NH_4^+ containing MOF.

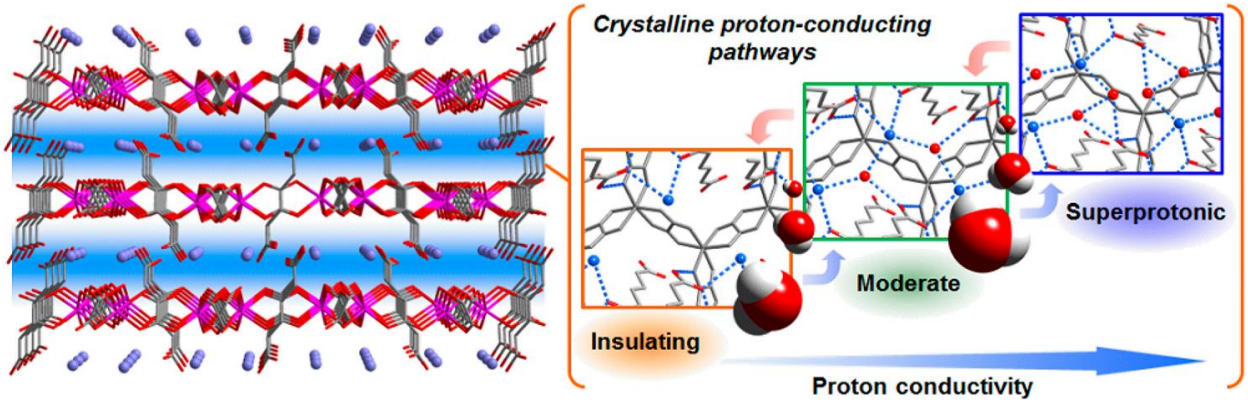

Figure 1.9. Left: Figure showing the presence of water, ammonium cations and adipic acid in the interlayer space. Right: The conductivity of the MOF increases as the level of hydration/number of the water molecule in the structure increase from 0 to 3. (Adapted from ref. 210)

Another Zn oxalate based MOF[231], $(Hpy)_2[Zn_2(ox)_3].nH_2O$ (n = 0, 1; Hpy = pyridinium cation), has been reported which shows a high conductivity of 2.2×10^{-3} S/cm at RT and 98% RH and an activation energy of 0.36 eV. The structure is made up of 2-D Honeycomb zinc oxalate sheets. Multiple sheets stack together in "eclipse" fashion along the c-axis, similar to the $(NH_4)_2[Zn_2(ox)_3](adp).3H_2O$. Two pyridinium cations are located in the interlayer space of the zinc oxalate sheets.

Many lanthanide oxalates have also been reported. A three-dimensional, water stable Eu-MOF, $[Me_2NH_2][Eu(ox)_2(H_2O)].3H_2O$[232], has a dia net topology and a dense hydrogen-bonded network formed by dimethyl ammonium and H_2O in the one-dimensional channels. The conductivity value for this MOF was found to be 4.0×10^{-6} S/cm at 45% RH, which increased quickly with an increase in humidity. It reached a value of 8.6×10^{-5} S/cm at 70% RH and attained a maximum value of 7.3×10^{-4} S/cm at 95% RH. The strong dependence of conductivity on humidity suggested the important role of water molecules present in the channels. The temperature dependence of the conductivity for the MOF was also studied from 15 to 55˚C at

95% RH. The MOF showed the highest conductivity of $2.73x10^{-3}$ S/cm at 55˚C and 95% RH. Recently, two water stable lanthanide–oxalate MOFs, namely MOF-1, $(N_2H_5)[CeEu(C_2O_4)_4(N_2H_5)].4H_2O$ and MOF-2, $(N_2H_5)[Nd_2(C_2O_4)_4(N_2H_5)].4H_2O$[233], were reported to show, by far, the highest RT conductivity (3.42×10^{-3} S/cm for MOF-1) at 100% RH among the lanthanide-based MOFs. The short distances (<3.0 Å) between the oxalates, lattice water molecules, and hydraziniums help form a very extensive hydrogen-bonding network, thereby facilitating high proton conductivity. MOF-1 has a very low activation energy of 0.10 eV which implies that the transfer of protons takes place by Grotthuss mechanism.

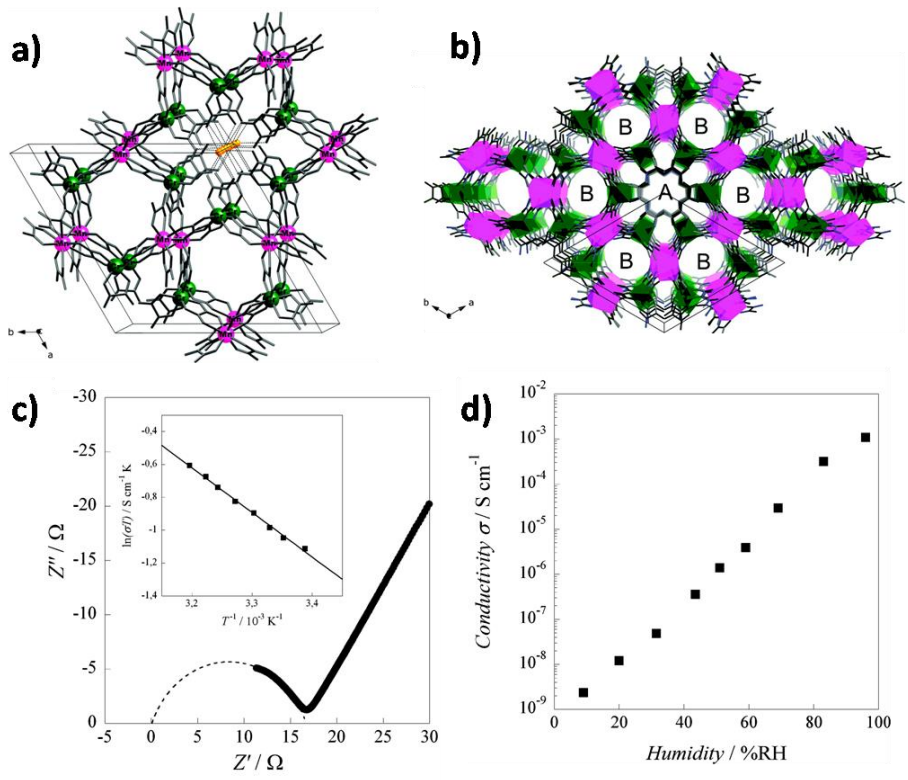

Figure 1.10. (a) Perspective view of the 3-D anionic framework of the MOF. Water molecules in the A-channels are shown in orange. (b) Right: View along the c axis showing the presence of two types of channels. (c) Nyquist plot for the MOF at 295 K and 96% RH with the inset showing an Arrhenius plot for calculating activation energy. (d) RH dependence of the conductivity at 295 K. Color code: green: Cr and purple: Mn, purple. (Adapted from ref. 234)

Bimetallic oxalates also deserve mention because of their exceptional stability. $(NH_4)_4[MnCr_2(ox)_6].4H_2O$[234] has a chiral 3-D quartz-like structure formed by anionic bimetallic coordination network. Ammonium cations and H_2O molecules are present in the functionalized

channels. The material exhibits a high proton conductivity of $1.1x10^{-3}$ S/cm at RT and activation energy of 0.23 eV (Figure 1.10). The structure is formed by each chromium ion coordinated to three oxalates which forms a six-coordinated distorted octahedron formed by the oxygens. One of the oxalates directly points toward the crystallization water along the helical axis and the other two oxalates bridge Cr(III) to Mn(II) ions in a bidentate manner. In turn, each Mn(II)is linked to four Cr(III) by bridging oxalate ligands. Two types of channels are present in this MOF, namely A-channels and B-channels (Figure 1.10). The A-channels are filled with guest water molecules which form 1-D ribbons/chains. The B-channels also have water molecules but could not be located because of them being highly disordered. A striking feature is that around the A-channels a well-defined helical chain of NH_4^+ forms. These exhibit strong H-bonding interactions with the oxygen atoms of the oxalates, which in turn are connected to the guest water molecules present in the A-channel.

Soon after, an analogue with imidazolium ions instead of NH_4^+, $((C_3N_2H_5)_4[MnCr_2(ox)_6].5H_2O)$[235] was reported by Pardo and coworkers which exhibited a high conductivity value of 1.86×10^{-3} S/cm at 295 K, 88% RH. Comparison of this MOF with the NH_4^+ analogue gave an insight on the effect of the guest's pKa on proton conduction.

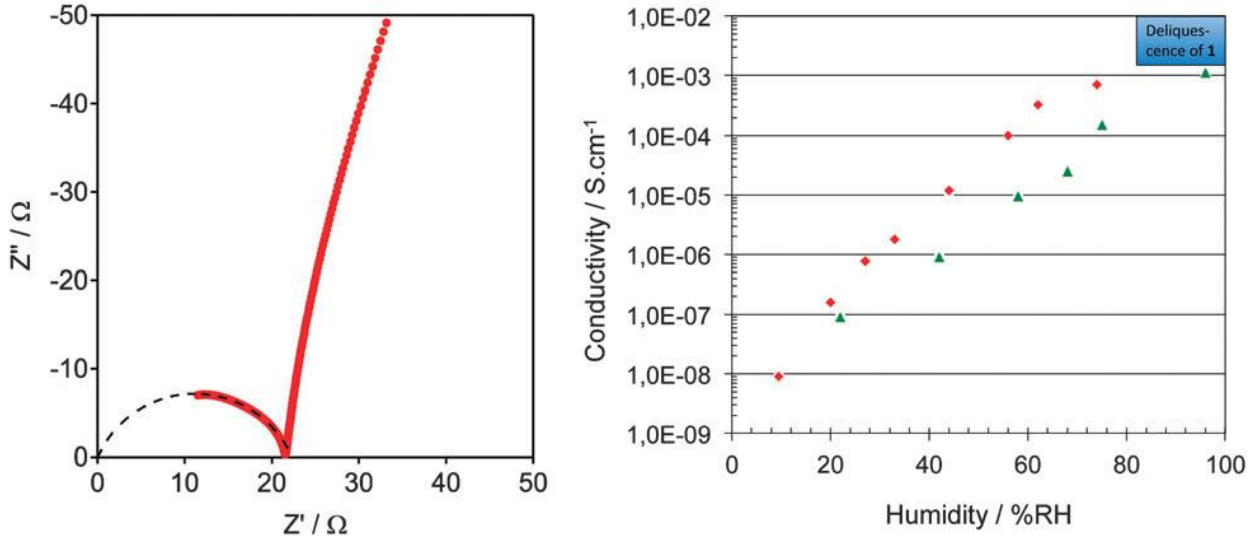

Figure 1.11. Cole-Cole plot for the conductivity of the MOF measured at 298 K, and 74% RH (left) and the comparison of the dependence of the conductivity of the MOF studied (red losange) and the parent compound (green triangle) on the relative humidity at 298 K. (Adapted from ref. 206)

Another $(NH_4)_5[Mn_2^{II}Cr_3^{III}(ox)_9].10H_2O$, with an unusual Mn^{II}/Cr^{III} ratio, reported by Train and coworkers[206] has a conductivity value of 7.1 x 10^{-4} S/cm at 74% RH (Figure 1.11). The conductivity measurements could not be done above 74% RH because the crystals are deliquescent above 80% RH. On decreasing the relative humidity, the conductivity values decrease dramatically by five orders of magnitude and reaching 9.1 x 10^{-9} S cm at 9.5% RH. In comparison with the parent compound[234], the conductivity of this MOF is found to be slightly higher at comparable relative humidity and can probably be explained by the presence of larger channels. In turn, the deliquescent behavior of this MOF at high RH can also be due to the enhanced accessibility to water molecules.

Proton conduction of the $La^{III}M^{III}$ compounds, $LaM(ox)_3.10H_2O$ (abbreviated as LaM; M = Cr, Co, Ru, La)[212] have been studied with respect to their networks. LaCr and LaCo have a ladder-like structure. LaCr has a coplanar ladder structure having an alternate array of the Cr and La ion (Figure 1.12 a). The ladder chain is zigzag-shaped with La ions at the projecting sites and Cr ions at the vacant sites. The ladders are knitted to form channels running along the b-axis filled with water molecules which form a hydrogen-bonded network for proton transfer (Figure 1.12 b, c).

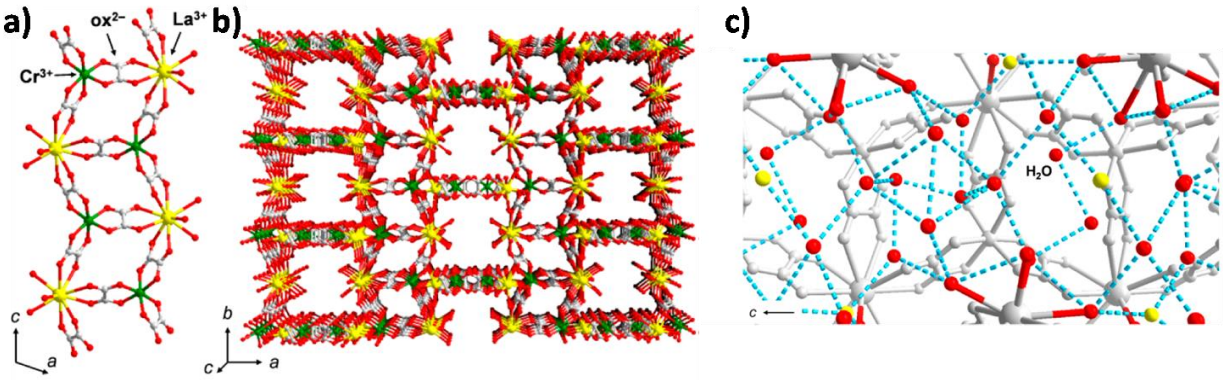

Figure 1.12. Crystal structure of LaCr. (a) The ladder structure and (b) 1-D channels with water molecules omitted for clarity. Color code: yellow: La, green: Cr, gray: C, and red: O. (c) Hydrogen-bonded network formed by the water molecules shown in blue dotted line. Yellow spheres: water molecules with 50% occupancy. (Adapted from ref. 212)

LaRu and LaLa have a honeycomb layered structure (Figure 1.13). La in these structures is nine-coordinated $\{La(ox)_3(H_2O)_3\}$. Large, continuous channels are not formed in these cases

because of the offsets of the layers. The water molecules are present in the channels running along the [011] direction. Unlike LaCr, these uncoordinated water molecules do not form an infinite hydrogen-bonded network.

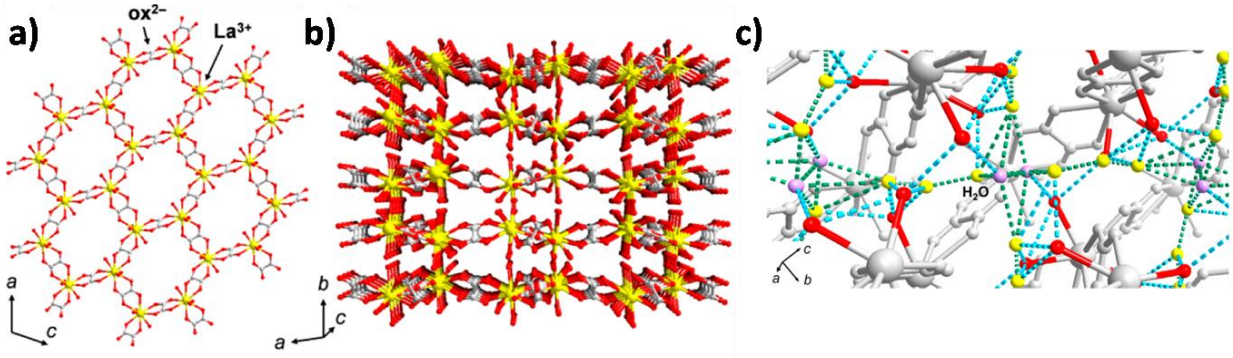

Figure 1.13. Crystal structure of LaLa. (a) The honeycomb layer structure and (b) 1-D channels where the water molecules are omitted for clarity. Color code: yellow: La, gray: C, and red: O. (c) Hydrogen-bonded network formed by the water molecules shown by blue dotted lines. Yellow and purple spheres: water molecules with 50 and 25% occupancy, respectively. (Adapted from ref. 212).

Authors have explained the formation of these structures on the basis of the rigidity versus flexibility of $[M(ox)_3]^{3-}$ in the framework with La^{III}. The ladder structure is related with the 4f/3d combination, whereas the layered structure is related with the 4f/4d combination. Therefore, the transition M^{III} seems to be playing a role in determining the favored structure. LaCr and LaCo show proton conductivity, in the range of 1×10^{-6} to 1×10^{-5} S/cm at 298 K over 40−95% RH, whereas the layer networks of LaRu and LaLa show low proton conductivity of $\sim 3 \times 10^{-8}$ S/cm at 298 K over 40−95% RH (Figure 1.14). While LaCr has a low activation energy of 0.32 eV, LaRu has a high activation energy of 0.90 eV probably due to the absence of extensive hydrogen-bonded network in case of LaRu.

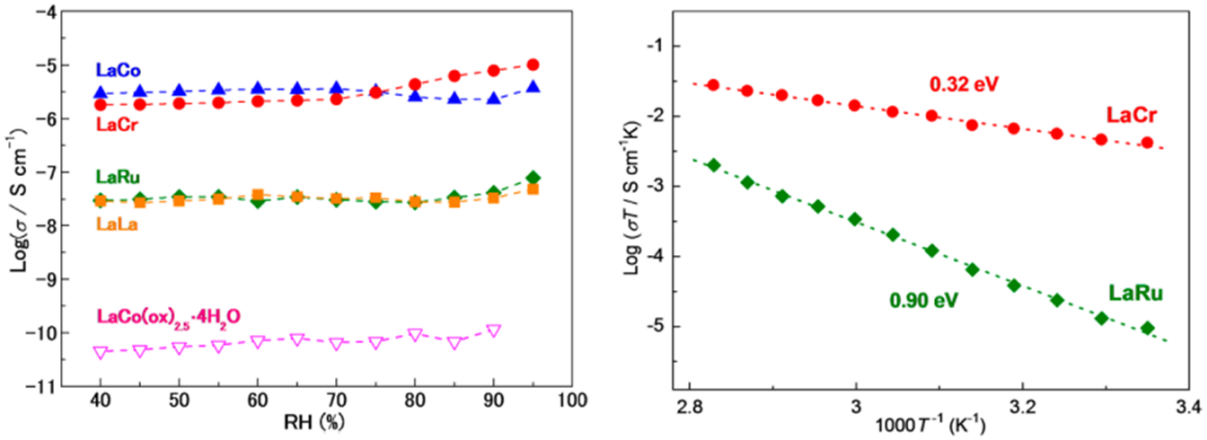

Figure 1.14. Left: Log(σ/S/cm) vs. RH profiles for LaM and $LaCo(ox)_{2.5}\cdot 4H_2O$ at 298 K. Right: Arrhenius plots for LaCr (red) and LaRu (green) at 298−355 K under 95% RH. (Adapted from ref. 212).

Carboxylate-based MOFs

Kitagawa and coworkers[236] reported a study where they observed correlations between the pKa, proton conductivity, and the activation energy. M(OH)(bdc-R) [MIL-53(M); H_2bdc = 1,4-benzene dicarboxylic acid; M = Al, Fe; R = H, NH_2, OH,$(COOH)_2$] were studied for proton conduction under humid conditions. Al(OH)(bdc)(H_2O) [MIL-53(Al)], Al(OH)(bdc-NH_2)(H_2O) [MIL-53(Al)-NH_2], Al(OH)(bdc-OH)$(H_2O)_{1.5}$ [MIL-53(Al)-OH], and Fe(OH)(bdc-$(COOH)_2$)(H_2O) [MIL-53(Fe)-$(COOH)_2$] have been denoted as **1**, **2**, **3** and **4** respectively.

Their structure is formed of infinite chains of corner-sharing $MO_4(OH)_2$ octahedra which are interconnected via carboxylate groups and have 1-D diamond-shaped channels (Figure 1).The proton conductivities and activation energies were calculated to be 2.3 x 10^{-8}, 2.3 x 10^{-9}, 4.2 x 10^{-7}, and 2.0 x 10^{-6} S/cm, 0.47, 0.45, 0.27, and 0.21 eV for **1**-**4** respectively, at 298 K and 95% RH. MIL-53(Fe)-$(COOH)_2$ showed the highest conductivity amongst all and the lowest activation energy owing to its lowest pKa value in this system. This was the first example where the conductivity was widely controlled by ligand substitution in a series of proton conducting MOFs.

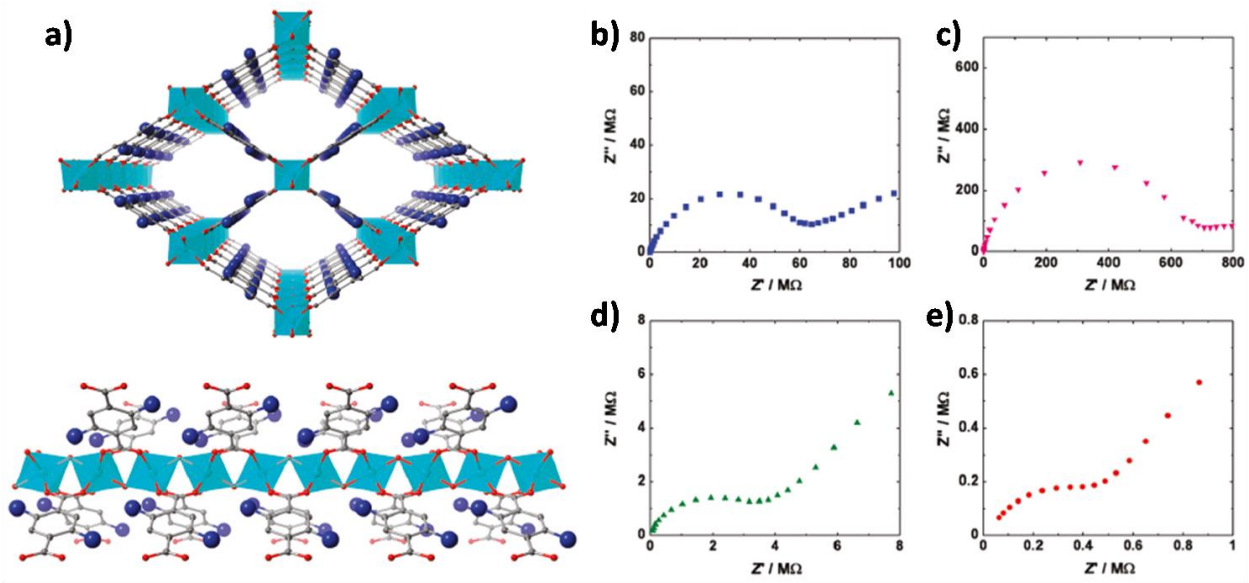

Figure 1.15. (a) Figure showing chains of corner sharing $MO_4(OH)_2$ octahedra and the structure along the channel axis. Light-blue: Al or Fe, gray: C, red: O, and the blue atoms represent the functional groups (-NH_2, -OH, or -COOH). Nyquist plots of (b) **1**, (c) **2**, (d) **3**, and (e) **4** at 298 K and 95% RH. (Adapted from ref. 236)

In another study, Hupp and coworkers[237] assessed the effect of solvent on the proton conduction. The well-known MOF, HKUST-1, which has coordinated, acidic water in the framework was used for the study. The pore-filling guest solvent molecules and the chemical identities coordinated to the metal could be independently varied, thus enabling the reversible modulation of proton conductivity. For example, the proton conductivity increased by ~75-fold when the coordinated acetonitrile molecules were replaced with water. In contrast, the conductivity became almost negligible when methanol present in the pores was replaced by hexane.

A functional calcium phosphonate framework $Ca_2[(HO_3PC_6H_3COOH)_2]_2[(HO_3PC_6H_3(COO)_2H)(H_2O)_2].5H_2O$ [$4.4H_2O$; ligand: PiPhtA = 5-dihydroxy phosphoryl-isophthalic acid] which is responsive to the guest molecules has been reported by Cabeza and coworkers[221]. The MOF has a complex layered-pillared structure having hydrophilic 1-dimensional channels running along the b-axis (Fig. 1.16a). Owing to the partial dehydration of the MOF at 75˚C, another framework with the formula $Ca_2[(HO_3PC_6H_3$-$COOH)_2]_2[(HO_3PC_6H_3(COO)_2H)(H_2O)_2]$ (**4**) is formed which upon exposure to 28% ammonia

vapour changes to poorly crystalline **4**@NH_3.The conductivity values for **4**.H_2O and **4** are 5.7 x 10^{-4} and 3.6 x 10^{-4} S/cm at 24˚C and 98% RH, respectively. **4**@NH_3 exhibits the highest conductivity of 6.6 x 10^{-3} S/cm at 24˚C and 98% RH (Fig. 1.16b). Authors assign the difference in the conductivity to the disruption of the interlayer phosphonate/Ca^{2+} or carboxylate/Ca^{2+} bonds of **4**.H_2O on exposure to NH_3 which results in a **4**@NH_3 multiphase compound, increasing proton conduction.

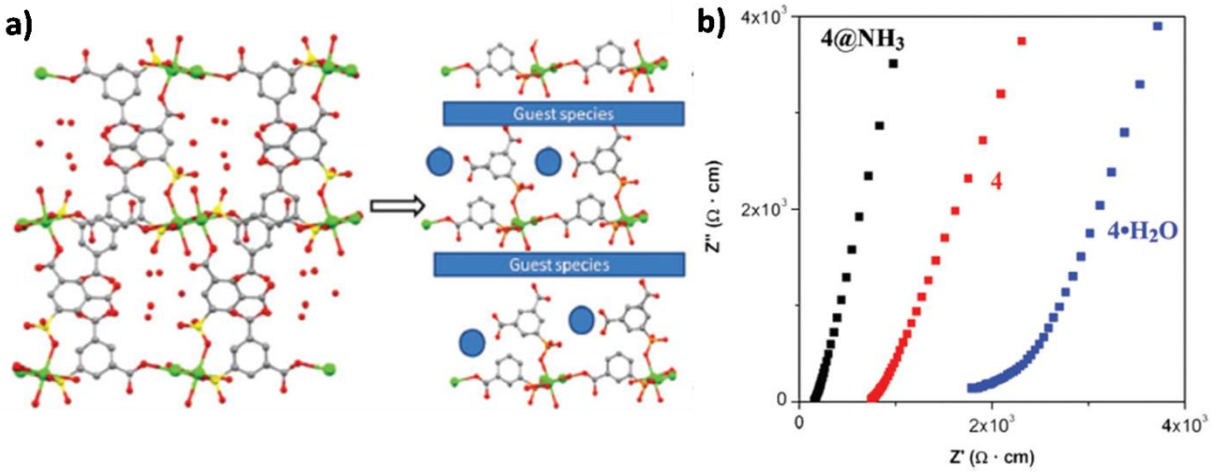

Figure 1.16. (a) Representation of the disruption of the 3-D framework to form a 2-D intercalated structure. (b) Impedance plot for the compounds at 24˚C and 98% RH. (Adapted from ref. 221)

A Nd-based bimetallic MOF [Nd(mpca)$_2$Nd(H_2O)$_6$Mo(CN)$_8$].nH_2O (mpca = 5-methyl-2-pyrazine carboxylate) has been shown to conduct protons[222]. This MOF exhibits dense and extensive hydrogen bonds formed by the carboxylate groups of the ligand with the coordinated as well as free water molecules, enabling high proton conductivity of 10^{-3} S/cm.

Zhang's group reported lanthanide(III) based MOFs [LnL(H_2O)$_3$].2H_2O (Ln = Y, Pr–Yb; L = N-phenyl-N0-phenylbicyclo[2,2,2]-oct-7-ene-2,3,5,6-tetracarboxdiimide tetracarboxylicacid) having 3-D framework which exhibit tunable emission, and proton-conduction[223]. The highest proton conductivity is 1.6 x 10^{-5} S/cm at 75˚C and 97% RH, and the activation energy is more than 0.4 eV indicating conduction through the vehicular mechanism.

Other lanthanide carboxylate MOFs {[LnK(BPDSDC)(DMF)(H_2O)].x(solvent)}$_n$ (Ln = Sm^{3+}, Eu^{3+}, and Pr^{3+}; BPDSDC =biphenyl-3,30-disulphonyl-4,40-dicarboxylic acid) have also been studied as proton-conducting materials[198]. The rod-shaped SBUs made up of Ln^{3+}, and K^+

ions are linked by the ligand, $BPDSDC^{4-}$, generating a 3-dimensional framework. The final 3-D structure two different types of 1-D channels running along the c-axis: the smaller trigonal channels and larger hexagonal shaped channels (Fig. 1.17). The Sm analogue shows proton conductivity of 1.11 x 10^{-3} S/cm at 80˚C and 98% RH. The presence of the channels lined by sulphonate groups and full of water molecules facilitates the proton conduction in this material.

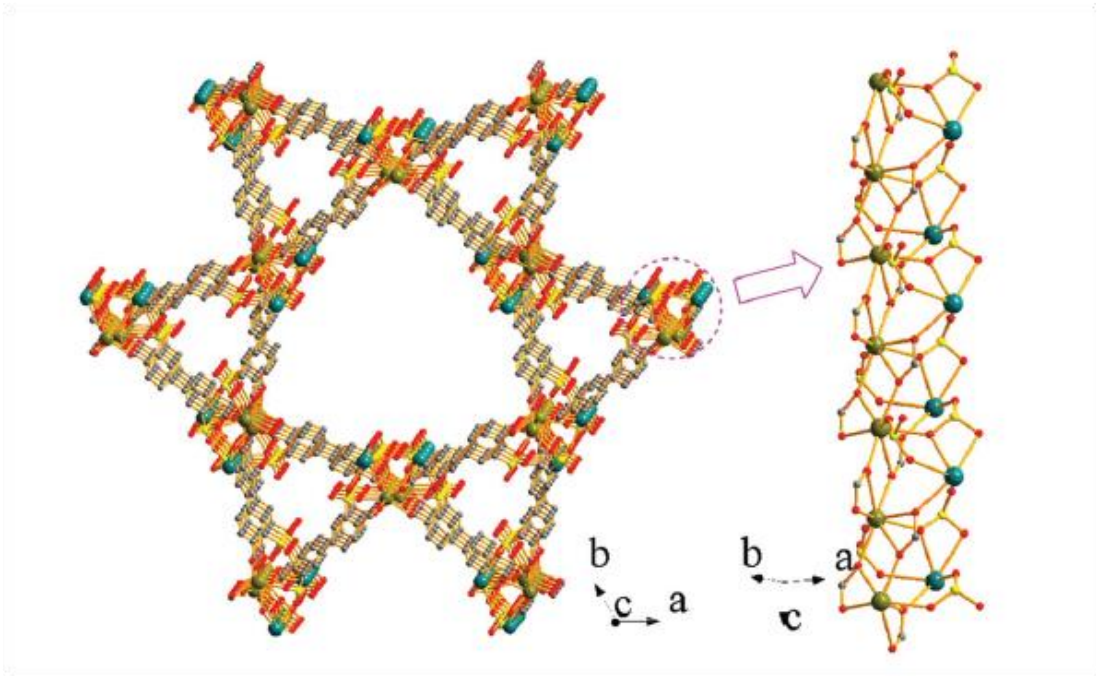

Figure 1.17. The 3-D framework showing trigonal and hexagonal channels, and the rod-shaped secondary building unit. (Adapted from ref. 198)

A new framework $\{[H_3O][Cu_2(DSOA)(OH)(H_2O)].9.5H_2O\}_n$ (DSOA = disodium-2,20-disulphonate-4,40-oxydibenzoicacid) has a tetranuclear-based network and has been investigated for its proton conductivity[199]. It has a tetrameric copper cluster with a $[Cu_4(\mu 3\text{-}OH)_2]^{6+}$ core connected by six DSOA ligands, producing a 3-D anionic framework (Figure 1.18). The channels are filled with hydronium ions and disordered solvent molecules. It exhibits proton conductivity >10^{-3} S/cm at 85–100˚C and 98% RH.

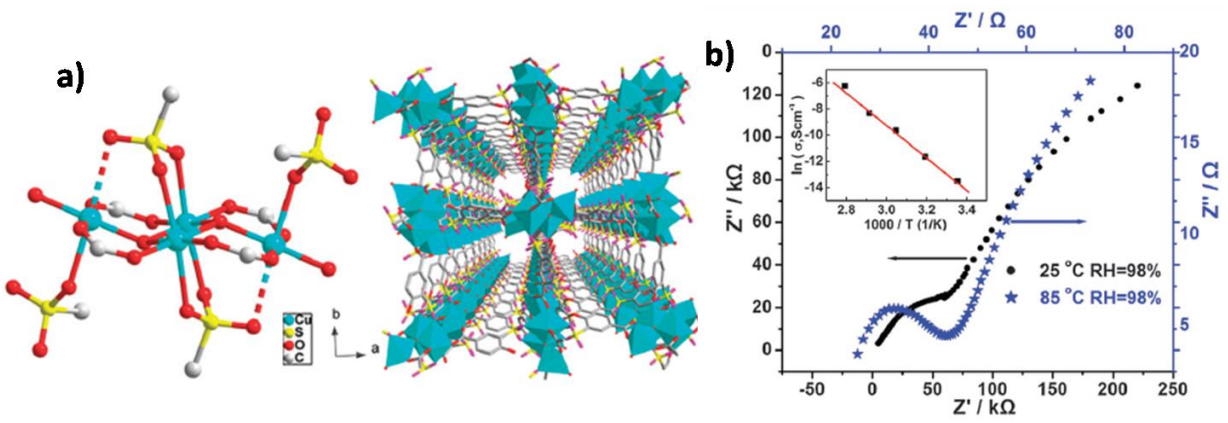

Figure 1.18. (a) Figure showing tetrameric Cu cluster and the central projection of the MOF viewed along the c-axis. (b) Nyquist plot for Cu-DSOA at 25˚C, and 85˚C and 98% RH. The inset shows the Arrhenius plot for Cu-DSOA. (Adapted from ref. 199)

A MOF, $Fe_4(BDC)_2(NDC)(SO_4)_4(DMA)_4$ (NDC = naphthalene-2,6-dicarboxylate; BDC =benzene-1,4-dicarboxylate) is made up of infinite rod SBUs ($[Fe_2(CO_2)_3(SO_4)_2(DMA)_2]_n$ connected with an NDC^{2-} and two BDC^{2-} ligands to form a 3-D framework fob topology[226]. DMA ions are present near the SBUs in the channels and form very strong hydrogen bonding with the sulfate ligands, giving a closely-packed hydrogen-bonded pathway. The proton conductivity of the MOF is 2.90 x 10^{-2} S/cm at 95˚C and 60% relative humidity. Most importantly, this conductivity is easily maintained for 40 h with no obvious loss.

Feng and Bu have combined oxalate and 4,5-imidazoledicarboxylate(imdc) with In^{3+} metal ions to form a MOF with the formula $[In(imdcH)(ox)].(NH_4)(H_2O)_{1.5}$[227]. It exhibits a unique layered structure where two types of proton containing channels coexist (Fig. 1.19). The type I channel passes through the interlayer space generated by the two oxalate ligands from neighboring layers whereas the type II channel passes through the interlayer space formed by two adjoining imdc ligands. These two channels have an alternate arrangement in the same layer and are perpendicular to each other. Type I channels host NH^{4+} ions as the major proton carriers, and the proton in type II channels can transfer between carboxylic groups of adjacent imdc ligands to achieve conduction.

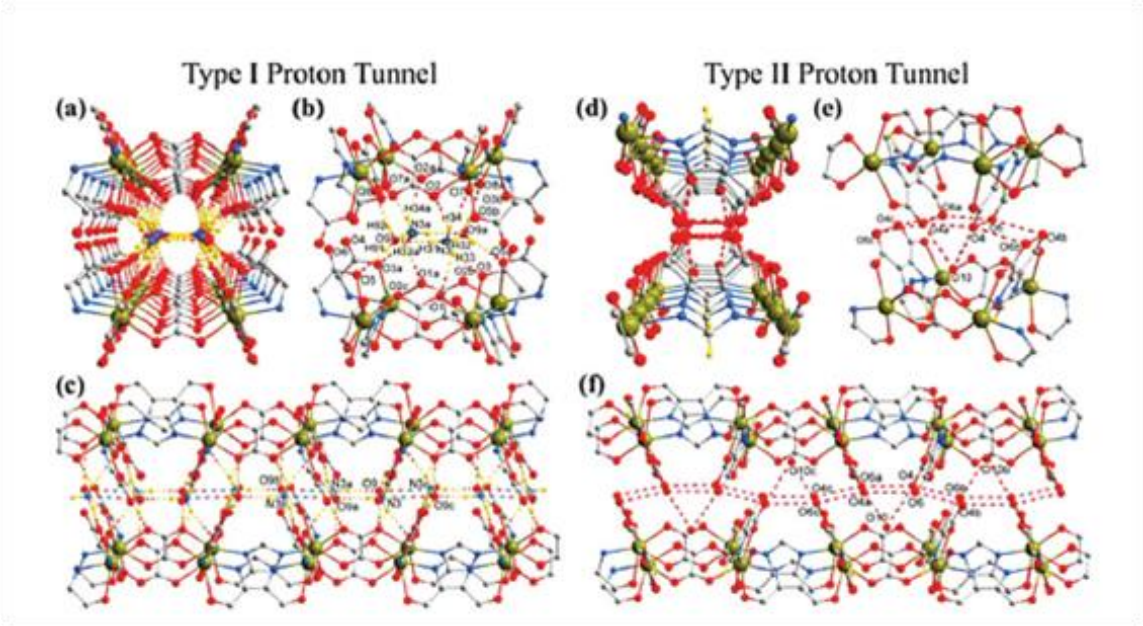

Figure 1.19. Figure showing (a) perspective view of type I channels along the [110] direction, (b) the interlayer space between type I and type III rings and the related hydrogen bonds; (c) hydrogen bonds along the type I channel;(d) perspective view of the type II channels along the [110] direction, (e) the interlayer space between type II and type III rings; and (f) hydrogen bonds along the type II channel. Color code: Gold: In; red: O; blue: N; grey: C; yellow: H. (Adapted with from ref. 227).

1.5.2. MOFs having anhydrous proton conduction

A large number of MOFs having water-assisted proton-conduction have been reported, but their low-temperature operation limits their use in practical application. Many attempts have been made to develop MOFs having anhydrous proton conduction which can be used at higher temperatures (>90˚C). One of the strategies includes encapsulating proton carriers in the pores of the MOF. Heterocyclic molecules like imidazole, triazole, and benzimidazole have been employed because they are nonvolatile molecules having high boiling points. Thus, the incorporation of such molecules into the pores of the MOFs, help achieve proton conduction, even in the absence of water. Quite a few examples will be discussed in the following section.

One of the earliest reports was by Kitagawa and coworkers[190] where they used imidazole molecules as the proton carriers. They used two different aluminum MOFs, $Al(\mu2\text{-}OH)(1,4\text{-}ndc)_n$ (1,4-ndc = 1,4-naphthalene dicarboxylate) and $Al(\mu2\text{-}OH)(1,4\text{-}bdc)_n$ (1,4-bdc = 1,4-benzene dicarboxylate) because their pores had similar dimensions that could host imidazole molecules,

but were different in shapes and had different surface potentials. The proton conductivity of the ndc analogue was always higher than that of the bdc analogue, under anhydrous conditions. The authors claimed that the different features of the channels were responsible for the different interactions between the guest and the framework. The channels in the ndc and the bdc analogues have nonpolar and polar potential surfaces, respectively resulting in a free movement of imidazoles in the ndc MOF. The ndc analogue exhibited a conductivity of 2.2 x 10^{-5} S/cm at 120˚C, whereas the bdc analogue exhibited a conductivity of 1.0 x 10^{-7} S/cm at 120˚C. They also prepared an $[Al(OH)(ndc)]_n$ having histamine in the pore (Figure 1.20)[238]. It had a high proton conductivity of 1.7x 10^{-3} S/cm at150˚C and activation energy of 0.25 eV. On reducing the loading amount of histamine to half, the conductivity decreased to 2.1 x 10^{-4} S/cm at 150˚C emphasizing the importance of the concentration of the proton carriers for the conductivity.

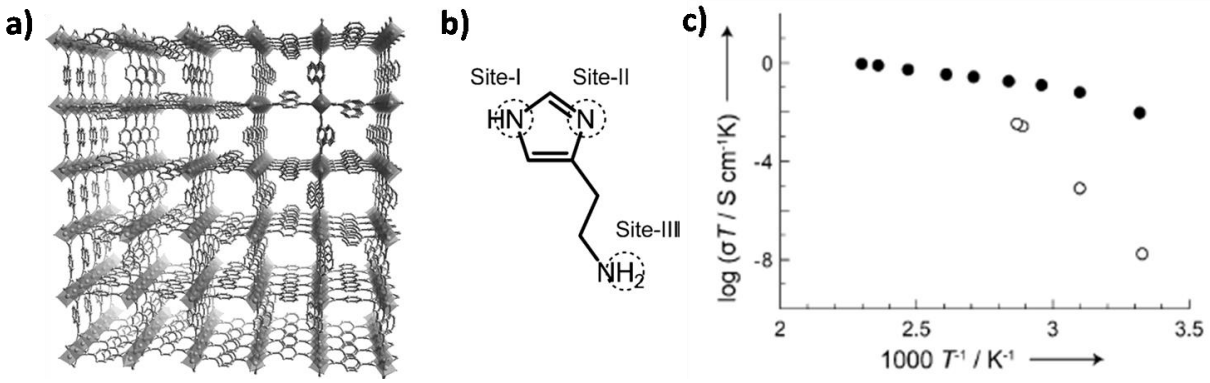

Figure 1.20. (a) Crystal structure of $[Al(OH)(ndc)]_n$. (b) The schematic view of histamine with three proton-hopping sites. (c) The Arrhenius plots for MOF with histamine in the pore (solid circle) and the bulk histamine (open circle) under anhydrous conditions. (Adapted from ref. 238)

Motivated by this work, Joswig and coworkers reported the computational results for the proton transfer between the imidazole molecules and the bdc analogue via molecular-dynamics simulations and a tight binding density-functional method[239]. Their results suggested that the structure of the MOF allowed imidazole molecules to transfer protons by the grotthus mechanism but also had strong interactions with them, influencing their free movement. They also proposed a well-balanced relationship between the two effects.

$[Zn_2(2,5\text{-DOTP})]_n$ (DOTP = 2,5-dioxidoterephthalate, MOF-74 or CPO-27(Zn))[240] with a honeycomb structure having one-dimensional straight micropores of ~11 Å and coordinatively

unsaturated metal sites was studied for proton conduction after loading it with 0.77 histamines per one Zn^{2+}. From the HETCOR experiments, the authors proposed that the imidazole rings of histamine were centrally located in the pore (Figure 1.21). They reported an anhydrous conductivity of 4.3×10^{-9} S/cm at 146 °C.

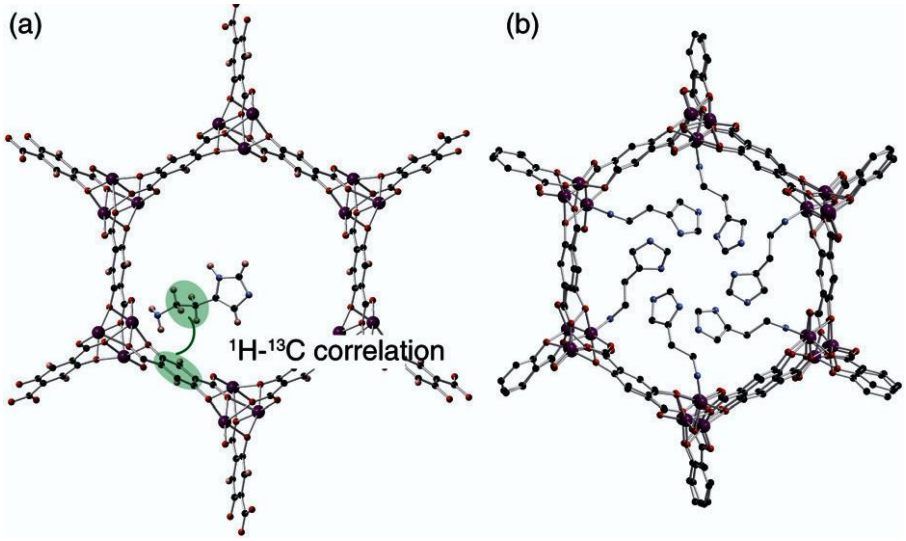

Figure 1.21. (a) A schematic representation of the proximity between the MOF's framework and histamine. (b) The typical simulated configuration of packed histamines in MOF. (Adapted from ref. 240).

Proton conductivity has also been studied in an In(III)-isophthalate MOF[241]. It showed an anhydrous proton conductivity of 1.18×10^{-5} S/cm at 90˚C.

1.6. Proton conduction mechanisms

Developing electrolytes for FCs require a thorough understanding of the mechanism by which the proton is transported within a material. On the application of a potential difference, the charged species travel from a site that is taken by the charge to the vacant site in the solid-state conductor. This applied potential creates vacant sites in the material which are lower in energy, and the difference in energy among the two sites leads to the net movement of the charged species in the direction of applied potential, resulting in the generation of current and observation of ionic conductivity (σ). The ionic conductivity is expressed mathematically by Equation 1.3. It is described in terms of the charge (q), the number of mobile charged species/unit volume (n), and mobility of charge carrier (μ).

$\sigma = nq\mu$ **…Equation 1.3**

To increase the proton conductivity, only n and μ can be varied, as the charge on the proton is constant (1.602 x 10^{-19} C). Tuning the mobility of a proton is a tricky task to achieve because the control of structure at Å-level is difficult. On top of presence of mobile protons, an energetically favored and accessible site should also be present in the structure for the facile transfer of protons. These sites must be inside a practical hydrogen-bonding distance and should provide an unhindered path to offer low activation energy (Ea) barrier to the movement of the proton. This type of proton movement happens via a mechanism called the Grotthuss mechanism (Figure 1.22). It involves the transportation of a proton by hopping via an extensive and infinite hydrogen-bonded network[242]. This mechanism is also known as the hopping mechanism. The charged species or the proton bearing species transfers its proton to the next which then structurally reorients itself and again transfers the proton in question to the next species. The proton hops from one available site to the other, and this hopping involves breaking and formation of hydrogen bonds.

Figure 1.22. A schematic representation of the two mechanisms for the transfer of protons within a material. (Adapted from Polymers 2012, 4, 1627-1644; doi:10.3390/polym4041627)

Another mechanism for the transfer of protons, called the vehicular mechanism[243], is normally prevalent in larger pore systems. It involves the diffusion of a protonated species (such as H_3O^+), which carries the proton across and is called. This mechanism requires larger activation energy because the diffusion is limited by various factors such as the channel size, the vehicle size, the solvation extent, and the coefficient of diffusion. Notably, the conduction in a material need not be restricted to either of the two mechanisms, but can very well be a combination of the two. The determination of the mechanism responsible for the proton conduction in a material is done by the analysis of the activation energy involved with the process. Lower activation energy, usually lower than ~0.40 eV is normally designated to the

Grotthuss mechanism, whereas the activation energy is higher than 0.4 eV for the vehicular mechanism[243,244].

1.7. Measuring proton conduction and calculating the activation energy

1.7.1. Alternating-Current (AC) Impedance Spectroscopy

AC impedance spectroscopy is the technique generally used to measure proton conduction. In a DC circuit, Resistance is defined by Ohm's law, Equation (1.4), as the ratio between voltage (V) and current (I).

$$R = V/I \qquad \textbf{…Equation 1.4}$$

Ohm's law is only valid for an ideal resistor. Also, the voltage and current are in phase with each other and independent of the frequency applied. But in the real world, the circuits have much complex behavior, and the impedance (Z) becomes the AC equivalent of this resistance. Impedance is measured by applying a small AC potential to an electrochemical cell and monitoring the current as an output. The application of a small pulse of potential ensures the pseudo-linearity of the system (Figure 1.23). The current response to the AC (sinusoidal) potential is also sinusoidal in nature at the same frequency but is shifted in phase (φ). For a resistor, there is no phase shift, and therefore φ is 0 (Figure 1.23 b). For a capacitor, the current leads the voltage by +90˚ (Figure 1.23 c) and for an inductor voltage leads the current by +90˚ (Figure 1.23 d). In the real world, the electrical circuits are a combination of these components, and therefore the Ohm's law needs to be modified for the relation to be valid and fit these circuits.

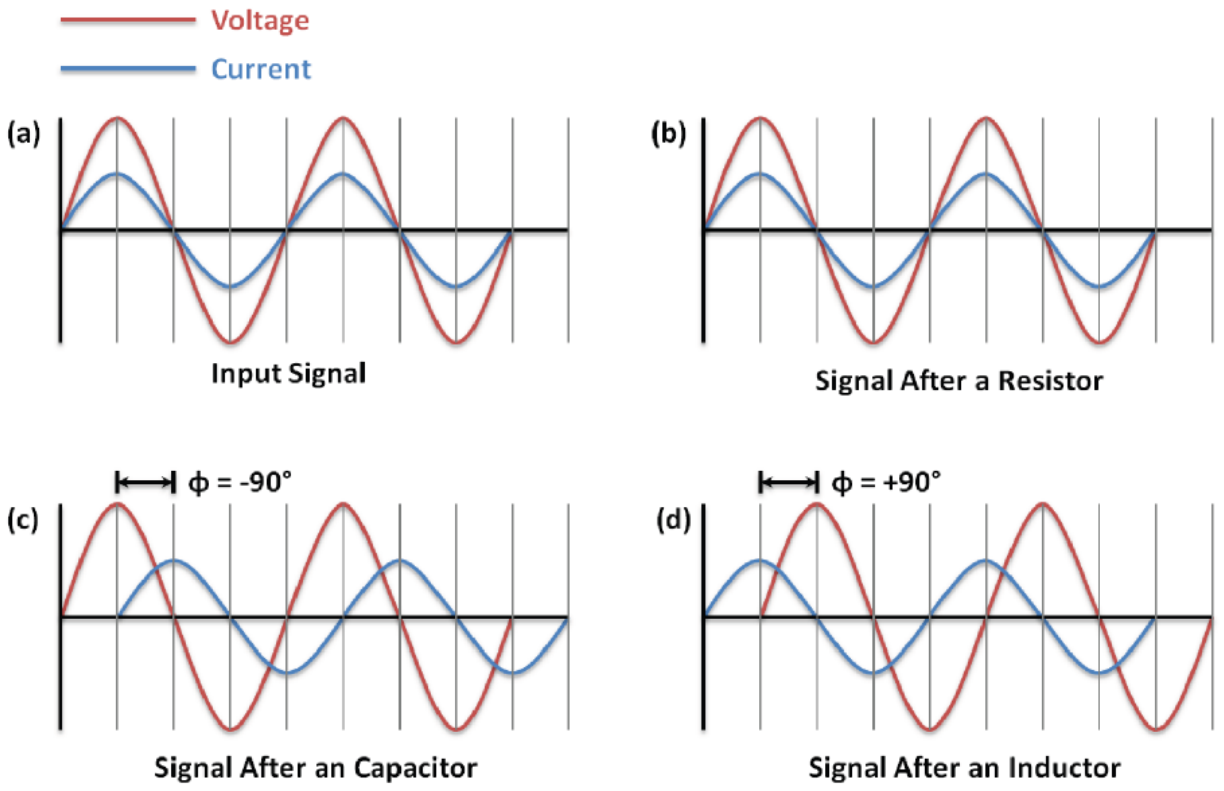

Figure 1.23. AC phase diagrams of current and voltage in the input signal (a), after passing through an ideal resistor (b), a capacitor (c) and an inductor (d). (Adapted from ref. 245)

The applied potential as a function of time is now expressed in the form:

$$Vt = Vosin(\omega t) \quad \textbf{...Equation 1.5}$$

Where Vt: Potential at time t,

Vo: Amplitude of the signal

ω: Radial frequency.

For a linear/pseudo-linear system, the response signal, i.e., current (I_t) is phase shifted and has different amplitude than I_o.

$$It = Iosin(\omega t + \varphi) \quad \textbf{...Equation 1.6}$$

The expression for impedance can therefore be written as:

$$Z = \frac{Vt}{It} = \frac{Vo\sin(\omega t)}{Iosin(\omega t+\varphi)} = Zo.\frac{Sin(\omega t)}{sin(\omega t+\varphi)} \quad \textbf{...Equation 1.7}$$

Z, as shown in equation 1.7 is made up of two components; magnitude (Zo) and phase shift (φ). Equation 1.7 can also be written in the form:

$Z = Z' + Z''$ **…Equation 1.8**

Where Z' is the in-phase component (real number) and Z'' is the out-of-phase component (imaginary number) of impedance. These values are then plotted on different axes to give the value of Z, which is a vector. The angle between the axis having Z' component and the vector and the real-axis represents the shift in phase, φ (Figure 1.24). The phase shift can vary from -90˚ to +90˚, therefore the Z" has both negative and positive values whereas Z' only has positive values. Measuring these values at different frequencies and plotting them gives a semi-circle and the plot is called a Nyquist plots. The high frequency data is plotted on the right side and low frequency data is plotted on the left side of the plot. The major drawback of a nyquist plot is that it doesn't give any information of the frequency at which the data point was taken.

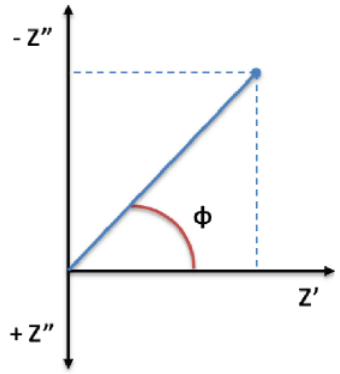

Figure 1.24. A Nyquist plot showing a single point from AC impedance spectroscopy. (Adapted from ref. 245)

The impedance measurements can be done either on a single crystal or pelletized microcrystalline powdered samples. Carrying the measurement on single crystal poses a great challenge as it is very difficult to grow defect-free, air stable crystals which are large enough to conduct measurement on. The crystal morphology also poses complications in measurements. Needle and platy crystals are very thin in one or more dimensions and can, therefore, crack while handling. Also, multiple measurements need to be done on a crystal to get data for different orientations because the conduction in a single crystal is anisotropic. This increases the measurement time. Moreover, the use of single crystal has only a remote relevance with commercialization as using a single crystal in a FC is very unlikely; however, the study on a single crystal is important to draw structure-conductivity relationship which is of value to future developments.

In case of single crystal one should ideally get a semi-circle in the nyquist plot, but it is perturbed by several effects. When the measurement is done at low frequency, the electrons and protons accumulate at the electrode/electrolyte interface because of the proton blocking and electron blocking nature of electrodes and electrolyte, respectively. This gives rise to a vertical line in the graph due to double layer capacitance (Figure 1.25). If required, conducting the measurement under a hydrogen atmosphere and using non-blocking electrodes can help eliminate the capacitative tail.

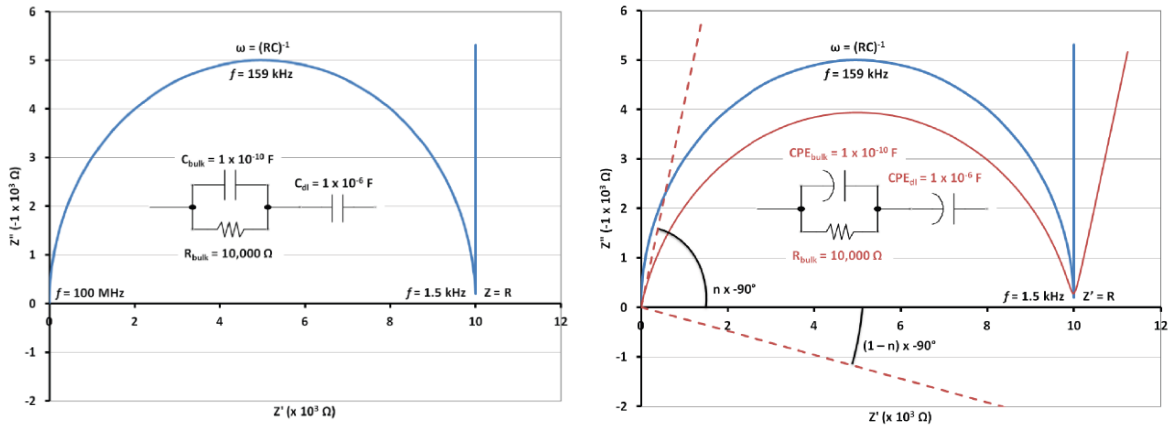

Figure 1.25. Left: Nyquist plot for a single crystal showing capacitative tail at low frequencies. Right: Nyquist plot comparison of ideal single crystal (blue) and simulated realistic plot (red) due to CPE. The dashed line shows the effect of depression on Z,' and Z. (Adapted from ref. 245)

Another perturbation is because of the deviation of the capacitances from their ideal behavior, due to current leakage, the surface roughness of the components, and anisotropic current effects at sample edges, which gives rise to constant phase element (CPE)[246]. It leads to depression, which is basically the clockwise rotation of the Nyquist plot that results in a depressed semi-circle (Figure 1.25).

Due to the challenges associated with the measurements on single crystal, AC impedance is usually run on pelletized microcrystalline powder samples. On pressing a pellet, formation of microscopic grain boundaries takes place resulting in an additional parallel RC circuit element owing to transfer resistance along the grain boundaries (Figure 1.26).

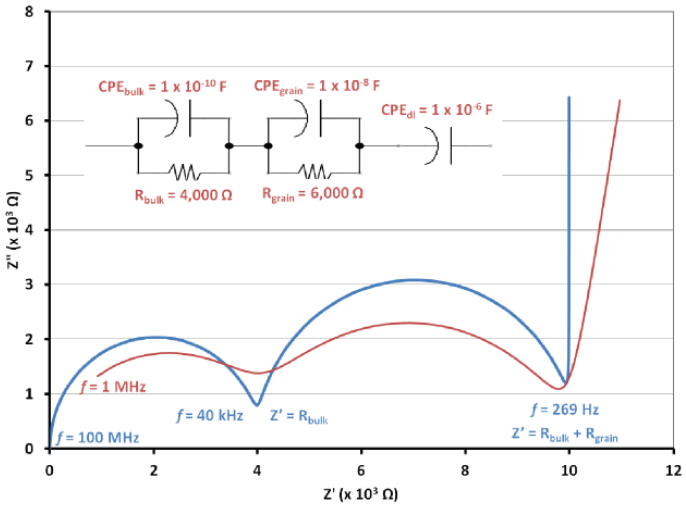

Figure 1.26. Nyquist plot comparing the behavior of an idealized pelletized sample conductor (blue) with simulated realistic behavior (red). (Adapted from ref. 245)

1.7.2. Sources of potential errors in proton conduction measurements.

Special attention needs to be paid to the stability of the sample under measurement conditions. One of the biggest concerns is water stability of the material, as the sample dissolution may give flawed results. As the sample dissolves, the contact between the sample and the electrodes is lost. The same happens in another phenomenon called 'sample settling' due to the vibrations during the measurement and the two are normally confused with each other. But the two can be easily differentiated as the sample dissolution continues until the entire sample dissolves whereas the settling of the sample is momentary.

Sample decomposition is also a big concern. If the samples decompose or undergo phase changes during measurements, it might lead to an unexpected change in conductivity during the cycles. It can easily be monitored using analysis techniques like Post-impedance PXRD and elemental analysis. These techniques also substantiate any loss in crystallinity, and phase change. But sample equilibration is another factor that might lead to these changes and hugely impact the measurements.

Other errors include the errors in the measurement of the thickness of the pellet, modeling of equivalent circuit, temperature, and RH. Measuring the thickness of the pellet multiple times helps avoid the associated error. Uncertainty in temperature is relatively very

small (< 1%), and can be easily taken care of by bringing the sample and the thermocouple as close as possible. The uncertainties for equivalent circuit fittings usually depend on the quality of the data collected and is usually <10%. However avoiding the error in the measurement of the exact RH seen by the sample is little difficult.[245]

1.7.3. Calculation of activation energy

The activation energy calculations are rather simple and are done using the Arrhenius equation[85] (Equation 1.9).

$$\ln(\sigma T) = -\frac{Ea}{kT} + \ln(\sigma o) \qquad \textbf{…Equation 1.9}$$

Measuring the conductivities at different temperatures and plotting them as a function of temperature provides the activation energy associated with the conduction process in a material. On plotting ln(σT) on y-axis and 1/T on x-axis, one gets a straight line in the graph which has a slope of $-\frac{Ea}{k}$ (Figure 1.27).

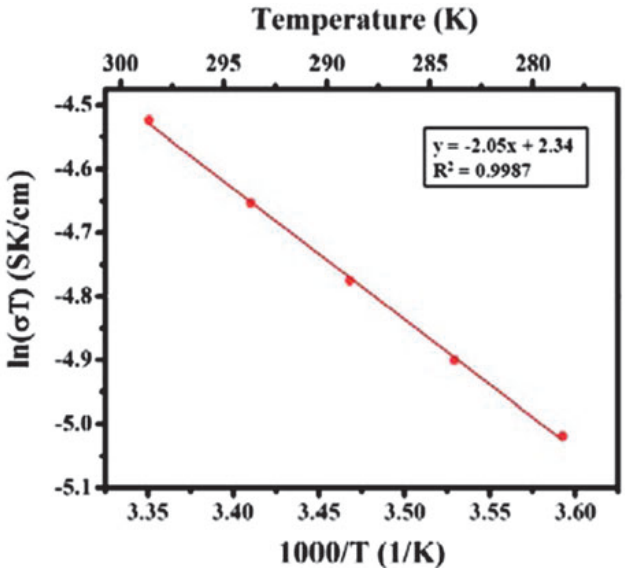

Figure 1.27. Arrhenius plot to determine activation energy for proton conduction. (Adapted from J. M. Taylor, Ph.D. thesis, University of Calgary, 2012)

1.8. Overview of the thesis

Herein, our objective is to develop new scalable, stable, and dense MOFs from cheap and readily available components and to investigate them for proton conduction applications. The main target is to develop a wide temperature range proton conductor. The thesis is built up towards that goal by gaining insights from different systems developed during this study. In our design strategy, we have resorted to only dense MOFs which are synthesized from single metal. This approach makes the formation of pure phases easier as it eliminates the probability of multiple phases precipitating during the synthesis. Also, dense MOF ensures that the electrolyte material, being impermeable to gases, doesn't permit fuel-crossover. The ligands thus chosen are small linkers, namely terephthalic acid, and oxalic acid. The guests used as proton source as well as carriers are amphoteric in nature.

The thesis is divided into four chapters. The first chapter presents a brief account of fuel cells, impedance spectroscopy and a detailed account of oxalate and carboxylate based proton conducting MOFs reported in the literature. The rest of the three chapters deal with the work that has been done by the authors from Advanced Porous Materials Lab, Department of Chemistry, IISER Pune (in some cases via collaboration with researchers from other institutes). Chapter 2 describes the structure and proton conduction of three structurally related metal organic frameworks. The difference in the humidity-dependent conductivity of three metal terephthalates (metal: Mg, Cd, and Nd) has been explained on the basis of their structural similarities and differences. The protic species, i.e., zwitterionic pyridinol, is incorporated as a part of the framework to avoid its leaching during the operating conditions. Chapter 3 discusses the enhancement in the proton conductivity of the metal organic frameworks described in chapter 2 by post-synthetic modification. It is divided into two parts: The first part, chapter 3I, is about 1000-fold enhancement in proton conductivity of a MOF using post synthetically anchored proton transporters, i.e. ethylene glycols and the second part, chapter 3II, is about 10000-fold enhancement in proton conductivity of a MOF by post-synthetic doping of Cesium ions in the framework. Proton conducting MOFs with heterocyclic guests as proton carriers have been described in chapter 4. A family of 3-D Nd-oxalate MOF with different azoles has been synthesized. The proton conductivity of the three MOFs is related to the basicity of the azoles

loaded in the pore. Finally, by a post-synthetic approach, a wide-temperature range (RT to 150°C) proton conductor has been developed.

1.9. References:

1. U.S. Department of Energy, U.S. Energy Information Administration: International Energy Outlook 2013 (Report: DOE/EIA-0484(2013)), **2013**.
2. https://www.renewableresourcescoalition.org.
3. Creutzig, F.; Papson, A.; Schipper, L.; Kammen, D. M. *Environ. Res. Lett.* **2009**, *4*, 044011.
4. Whittingham, M. S. *MRS Bull*. **2011**, *33*, 411.
5. Kirubakaran, A.; Jain, S.; Nema, R. K. *Renew. Sust. Energ. Rev*. **2009**, *13*, 2430.
6. Schoenbein, C. F. X. *Philos. Mag*. **1839**, *14*, 43.
7. Grove, W. R. *Philos. Mag*. **1839**, *14*, 127.
8. Grove, W. R. *Philos. Mag*. **1842**, *21*, 417.
9. Wang, Y.; Chen, K. S.; Mishler, J.; Cho, S. C.; Adroher, X. C. *Appl. Energy*. **2011**, *88*, 981.
10. Cohn, E. M. In Fuel Cell Systems; Young, G. J.; Linden, H. R., Eds.; American Chemical Society: Washington, DC, **1969**; pp. 1–8.
11. Grot, W. *Chem. Ing. Tech*. **1972**, *44*, 167.
12. Grot, W. *Chem. Ing. Tech*. **1978**, *50*, 299.
13. Shaigana, N.; Qua, W.; Ivey D. G.; Chen, W. *J. Power Sources*, **2010**, *195*, 1529.
14. Antolini, E. *Appl. Energy*, **2011**, *88*, 4274.
15. Elmer T.; Riffat S. B. Progress in Sustainable Energy Technologies, ed. I. Dincer, A. Midilli and H. Kucuk, Springer International Publishing, Switzerland, **2014**, vol. II, pp. 247–271.
16. Kraytsberg A.; Ein-Eli Y. *Energy Fuels*, **2014**, *28*, 7303.
17. Fuel Cell and Battery Electric Vehicles Compared, Thomas C. E., https://www.energy.gov/sites/prod/files/2014/03/f9/thomas_fcev_vs_battery_evs.pdf).
18. Appleby, A. J. Fuel Cells: Trends in Research and Application, Hemisphere Publishing Corp, Washington DC, **1987**.
19. D. Linden, Handbook of Batteries and Fuel Cells, McGraw-Hill, New York, **1984**.
20. Lim J. W.; Lee, D. G. *Int. J. Hydrogen Energy*, **2012**, *37*, 12504.
21. Kim, B. G.; Lim J. W.; Lee, D. G. *Int. J. Hydrogen Energy*, **2011**, *36*, 3087.
22. Neto, R.C.; Teixeira, J.C.; Azevedo, J. L. *J. Hydrog.Energy*, **2013**, *38*, 5348.

23. Hamrock S. J.; Yandrasits M. A. *Polym. Rev*., **2006**, *46*, 219.
24. O'Hayre, R.; Cha, S.-W.; Colella, W.; Prinz, F. B. Fuel Cell Fundamentals; John Wiley & Sons, Inc.: Hoboken, NJ, **2006**.
25. Thangadurai, V.; Kan, W. H. H.; Mirfakhraei, B.; Bhella, S.; Trinh, T. T. *ECS Trans*. **2011**, *35*, 483.
26. Liu, M.; Lynch, M. E.; Blinn, K.; Alamgir, F. M.; Choi, *Y. Mater. Today*, **2011**, *14*, 534.
27. Farooque M.; Maru H. C. Fuel cells—the clean and efficient power generators. IEEE Proc **2001**, *89*, 1819.
28. Swider-Lyons K. E.; Carlin R. T.; Rosenfeld R. L.; Nowak R. J. Technical issues and opportunities for fuel cell development for autonomous underwater vehicles. In: Proceedings of the 2002 workshop on autonomous underwater vehicle; **2002**, 61.
29. Srinivasan, S. Fuel Cells: From Fundamentals to Applications; Springer Science+Business Media, LLC: New York, NY, **2006**.
30. O'Sullivan JB. Fuel cells in distributed generation. IEEE Proc **1999**, 568.
31. U.S. Dept. of Energy. Fuel cell hand book, 7th ed., West Virginia: Office of Fossil Fuel, National Energy Technology Laboratory; October **2000**.
32. Pourcelly, G. *Pet. Chem*. **2011**, *51*, 480.
33. Asensio, J. A.; Sánchez, E. M.; Gómez-Romero, P. *Chem. Soc. Rev*. **2010**, *39*, 3210.
34. Dupuis, A.-C. *Prog. Mater. Sci.* **2011**, *56*, 289.
35. Bose, S.; Kuila, T.; Nguyen, T. X. H.; Kim, N. H.; Lau, K.; Lee, J. H. *Prog. Polym. Sci*. **2011**, *36*, 813.
36. Alberti, G.; Casciola, M. *Annu. Rev. Mater. Res*. **2003**, *33*, 129.
37. Jourdani, M.; Mounir, H.; Marjani, A. E. *The Open Fuels & Energy Science Journal*, **2017**, *10*, 96.
38. Colomban, P. Proton Conductors: Solids, Membranes and Gels—materials and Devices. Series: Chemistry of Solid State Materials, Cambridge University Press, Cambridge, UK, **1992**.
39. Kreuer, K. D. *Chem. Mater*. **1996**, *8*, 610.
40. Kreuer, K. D.; Paddison, S. J.; Spohr E.; Schuster, M. *Chem. Rev*., **2004**, *104*, 4637.
41. Rolison, D. R.; Long, J. W.; Lytle, J. C.; Fischer, A. E.; Rhodes, C. P.; McEvoy, T. M.; Bourg M. E.; Lubersa, A. M. *Chem. Soc. Rev*., **2009**, *38*, 226.

42. Malavasi, L. C.; Fisher A. J.; Islam, M. S. *Chem. Soc. Rev*., **2010**, *39*, 4370.
43. Peron, J.; Shi Z.; Holdcroft, S. *Energy Environ. Sci.*, **2011**, *4*, 1575.
44. Smitha, B.; Sridhar, S.; Khan, A. A. *J. Membr. Sci*. **2005**, *259*, 10.
45. Rikukawa M.; Sanui, K.; *Prog. Polym.Sci*., **2000**, *25*, 1463.
46. Hoel D.; Grunwald, E. *J. Phys. Chem.* **1977**, *81*, 2135.
47. Steininger, H.; Schuster, M.; Kreuer, K. D.; Kaltbeitzel, A.; Bingol, B.; Meyer, W. H.; Schauff, S.; Brunklaus, G.; Maier J.; Spiess, H. W. *Phys. Chem. Chem. Phys.* **2007**, *9*, 1764.
48. Kawada, A.; McGhie, A. R.; Labes, M. M. *J. Chem. Phys.* **1970**, *52*, 3121.
49. Li, S.; Zhou, Z.; Zhang, Y.; Liu, M.; Li, W. *Chem. Mater*. **2005**, *17*, 5884.
50. Basak, D.; Christensen, S.; Surampudi, S. K.; Versek, C.; Toscano, D. T.; Tuominen, M. T.; Hayward, R. C.; Venkataraman, D. *Chem. Commun*. **2011**, *47*, 5566.
51. Schuster, M. F. H.; Meyer, W. H.; Schuster, M.; Kreuer, K. D. *Chem. Mater*. **2004**, *16*, 329.
52. Basak, D.; Versek, C.; Toscano, D. T.; Christensen, S.; Tuominen, M. T.; Venkataraman, D. *Chem. Commun*. **2012**, 5922.
53. Kreuer, K. D.; Fuchs, A.; Ise, M.; Spaeth M.; Maier, J. *Electrochim. Acta*, **1998**, *43*, 1281.
54. Casciola, M.; Chieli, S.; Costantino U.; Peraio, A. *Solid State Ionics*, **1991**, *46*, 53.
55. Alberti, G.; Constantino, U.; Casciola, M.; Vivani R.; Peraio, A. *Solid State Ionics*, **1991**, *46*, 61.
56. Mu¨nch, W.; Kreuer, K. D.; Silvestri, W.; Maier J.; Seifert, G. *Solid State Ionics*, **2001**, *145*, 437.
57. Sachdeva, S.; Turner, J. A.; Horan, J. L.; Herring, A. M. *Struct. Bond*. **2011**, *141*, 115.
58. Nakamura, O.; Kodama, T.; Ogino, I.; Miyake, Y. *Chem. Lett*. **1979**, 17.
59. Slade, R.; Barker, J.; Pressman, H. *Solid State Ionics* **1988**, *28*, 594.
60. Goñi-Urtiaga, A.; Presvytes, D.; Scott, K. Int. *J. Hydrogen Energy* **2012**, *37*, 3358.
61. Haile; Baranov, A. I.; Shuvalov, L. A.; Shchagina, N. M. *J. Exp. Theor. Phys*. **1982**, *36*, 381.
62. Haile, S. M.; Boysen, D. A.; Chisholm C. R. I.; Merle, R. B. *Nature*, **2001**, *410*, 910.
63. Alberti, G.; Casciola, M. *Solid State Ionics*, **2001**, *145*, 3.

64. Ponomareva, V. G.; Uvarov, N. F.; Lavrova G. V.; Hairetdinov, E. F. *Solid State Ionics*, **1996**, *90*, 161.
65. Otomo, J.; Minagawa, N.; Wen, C. J.; Eguchi K.; Takahashi, H. *Solid State Ionics*, **2003**, *156*, 357.
66. Ponomareva V. G.; Shutova, E. S. *Solid State Ionics*, **2007**, *178*, 729.
67. Moilanen, D. E.; Spry D. B.; Fayer, M. D. *Langmuir*, **2008**, *24*, 3690.
68. Mauritz K. A.; Moore, R. B. *Chem. Rev*., **2004**, *104*, 4535.
69. Ivanchev, S. S. *Russ. J. Appl. Chem*., **2008**, *81*, 569.
70. Gierke, T. D.; Munn G. E.; Wilson, F. C. J. *Polym. Sci., Part B: Polym. Phys*., **1981**, *19*, 1687.
71. Meng, X.; Wang, H. N.; Song, S. Y.; Zhang, H. J. *Chem. Soc. Rev*., **46**, *2017*, 464.
72. Maréchal, M.; Souquet, J.-L.; Guindet, J.; Sanchez, J.-Y. *Electrochem. Commun*. **2007**, *9*, 1023.
73. Mauritz, K. A.; Moore, R. B. *Chem. Rev*. **2004**, *104*, 4535.
74. Schmidt-Rohr, K.; Chen, Q. *Nat. Mater*. **2008**, *7*, 75.
75. Malis, J.; Paidar, M.; Bystron, T.; Brozova, L.; Zhigunov, A.; Bouzek, K.; *Electrochimica Acta.* **2018,** *262*, 264.
76. Malis, J.; Mazur, P.; Paidar, M.; Bystron, T.; Bouzek, K. *Int. J. Hydrogen Energy* **2016**, *41*, 2177.
77. Kwon, O.; Wu, S.; Zhu, D.-M. J. *Phys. Chem. B* **2010**, *114*, 14989.
78. Barique, M. A.; Wu, L.; Takimoto, N.; Kidena, K.; Ohira, A. *J. Phys. Chem. B* **2009,** *113* 15921.
79. Jia, N.; Lefebvre, M. C.; Halfyard, J.; Qi, Z.; Pickup, P. G. *Electrochem. Solid-State Lett.* **2000**, *3*, 529.
80. Rhee, C. H.; Kim, H. K.; Chang, H.; Lee, J. S. *Chem. Mater*. **2005**, *17*, 1691.
81. Mondal, S.; Soam, S.; Kundu, P. P. *J. Membr. Sci*. **2015**, *474*, 140.
82. He, G.; He, X.; Wang, X.; Chang, C.; Zhao, J.; Li, Z.; Wu, H.; Jiang, Z. *Chem. Commun*. **2016**, 52, 2173.
83. Amjadi, M.; Rowshanzamir, S.; Peighambardoust, S. J.; Sedghi, S. *J. Power Sources* **2012**, *210*, 350.

84. Mohammadi, G.; Jahanshahi, M.; Rahimpour, A. *Int. J. Hydrogen Energy* **2013**, *38*, 9387.
85. Ramaswamy, P.; Wong N. E.; Shimizu G. K. H. *Chem. Soc. Rev*., **2014**, *43*, 5913.
86. Cheng, X.; Zhang, J.; Tang, Y.; Song, C.; Shen, J.; Song, D.; Zhang, J. *Journal of Power Sources* **2007**, *167*, 25.
87. Zhang, J.; Tang, Y.; Song, C.; Zhang, J.; Wang, H. *J. Power Sources* **2006**, *163*, 532.
88. Collier, A.; Wang, H.; ZiYuan, X.; Zhang, J.; Wilkinson, D. P. *Int. J. Hydrogen Energy* **2006**, *31*, 1838.
89. Inaba, M.; Kinumoto, T.; Kiriake, M.; Umebayashi, R.; Tasaka, A.; Ogumi, Z. *Electrochim. Acta* **2006**, *51*, 5746.
90. Teranishi, K.; Kawata, K.; Tsushima, S.; Hirai, S.; *Electrochem. Solid-State Lett*. **2006**, *9*, A475.
91. Yu, J.; Matsuura, T.; Yoshikawa, Y.; Islam, M. N.; Hori, M. *Electrochem. Solid-State Lett.* **2005**, *8*, A156.
92. Chandesris, M.; Medeau, V.; Guillet, N.; Chelghoum, S.; Thoby, D.; Fouda-Onana, F. *Int. J. Hydrogen Energy* **2015**, *40*,1353.
93. Zhang H.; Shen P. K. *Chem. Rev*. **2012**, *112*, 2780.
94. Hogarth, W. H. J.; Diniz da Costa, J. C.; Lu, G. Q. *J. Power Sources* **2005**, *142*, 223.
95. Rusanov, A. L.; Marc, V. K. *Adv. Polym. Sci*. **2008**, 125.
96. Iulianelli, A.; Basile, A. *Int. J. Hydrogen Energy* **2012**, 1.
97. Peighambardoust, S. J.; Rowshanzamir, S.; Amjadi, M. *Int. J. Hydrogen Energy*, **2010**, *35*, 9349.
98. Mader, J.; Xiao, L.; Schmidt, T. J.; Fuel, B.; Ave, V. *Adv. Polym. Sci*. **2008**, 63.
99. Meek, S. T.; Greathouse, J. A.; Allendorf, M. D., *Adv. Mater*. **2011**, *23*, 249.
100. Batten, S. R.; Champness, N. R.; Chen, X.-M.; Garcia-Martinez, J.; Kitagawa, S.; Ohrstrom, L.; O'Keeffe, M.; Suh, M. P.; Reedijk, J. *CrystEngComm* **2012**, *14*, 3001.
101. Farha, O. K.; Eryazici, I.; Jeong, N. C.; Hauser, B. G.; Wilmer, C. E.; Sarjeant, A. A.; Snurr, R. Q.; Nguyen, S. T.; Yazaydın, A. Ö.; Hupp, J. T. *J. Am. Chem. Soc*. **2012**, *134*, 15016.
102. Yun, R.; Lu, Z.; Pan, Y.; You, X.; Bai, J. *Angew. Chem. Int. Ed*. **2013**, *52*, 11282.

103. Gru¨nker, R.; Bon, V.; Mu¨ller, P.; Stoeck, U; Krause, S.; Mueller, U.; Senkovska, I.; Kaskel, S. *Chem. Commun*. **2014**, *50*, 3450.

104. Furukawa, H.; Cordova, K. E.; O'Keeffe, M.; Yaghi, O. M. *Science* **2014**, *341*, 974.

105. Chae, H. K.; Siberio-Pe´rez, D. Y.; Kim, J.; Go, Y.-B.; Eddaoudi, M.; Matzger, A. J.; O'Keeffe, M.; Yaghi, O. M.; *Nature* **2004**, *425*, 523.

106. Banerjee, R.; Phan, A.; Wang, B.; Knobler, C.; Furukawa, H.; O'Keeffe, M.; Yaghi, O. M. *Science* **2008**, *319*, 939.

107. Tanaka, D.; Kitagawa, S., *Chem. Mater*. **2008**, *20*, 922.

108. Lee, J.; Farha, O. K.; Roberts, J.; Scheidt, K. A.; Nguyen, S. T.; Hupp, J. T. *Chem. Soc. Rev.* **2009**, *38*, 1450.

109. Liu, J.; Chen, L.; Cui, H.; Zhang, J.; Zhang, L.; Su, C.-Y. *Chem. Soc. Rev. 2014*, **43**, 6011.

110. Corma, A.; García, H.; Llabrés Xamena, F. X. *Chem. Rev.* **2010**, *110*, 4606.

111. Yoon, M.; Srirambalaji, R.; Kim, K. *Chem. Rev*. **2012**, *112*, 1196.

112. Mueller, U.; Schubert, M.; Teich, F.; Puetter, H.; Schierle-Arndt, K.; Pastre, J. *J. Mater. Chem.* **2006**, *16*, 626.

113. Wu, C.-D.; Lin, W. *Angew. Chem. Int. Ed*. **2007**, *46*, 1075.

114. Dybtsev, D. N.; Nuzhdin, A. L.; Chun, H.; Bryliakov, K. P.; Talsi, E. P.; Fedin, V. P.; Kim, K. A. *Angew. Chem. Int. Ed*. **2006**, *45*, 916.

115. Gao, W.-Y.; Wu, H.; Leng, K.; Sun, Y.; Ma, S. *Angew. Chem. Int. Ed*. **2016**, *55*, 5472.

116. Li, B.; Leng, K.; Zhang, Y.; Dynes, J. J.; Wang, J.; Hu, Y.; Ma, D.; Shi, Z.; Zhu, L.; Zhang, D.; Sun, Y.; Chrzanowski, M.; Ma, S. *J. Am. Chem. Soc*. **2015**, *137*, 4243.

117. Gole, B.; Bar, A. K.; Mallick, A.; Banerjee, R.; Mukherjee, P. S. *Chem. Commun*. **2013**, *49*, 7439.

118. Liu, Y.; Moon, S.-Y.; Hupp, J. T.; Farha, O. K. *ACS Nano*, **2015**, *9*, 12358.

119. Fei, H.; Shin, J.; Meng, Y. S.; Adelhardt, M.; Sutter, J.; Meyer, K.; Cohen, S. M. *J. Am. Chem. Soc.* **2014**, *136*, 4965.

120. Li, H.; Eddaoudi, M.; O'Keeffe, M.; Yaghi, O. M. *Nature* **1999**, *402*, 276.

121. Rosi, N. L.; Eckert, J.; Eddaoudi, M.; Vodak, D. T.; Kim, J.; O'Keeffe, M.; Yaghi, O. M. *Science* **2003**, *300*, 1127.

122. Millward, A. R.; Yaghi, O. M. *J. Am. Chem. Soc*. **2005**, *127*, 17998.

123. Rowsell, J. L. C.; Yaghi, O. M. *Angew. Chem. Int. Ed*. **2005**, *44*, 4670.

124. Ma, S.; Zhou, H.-C. *Chem. Commun*. **2010**, *46*, 44.

125. Peng, Y.; Krungleviciute, V.; Eryazici, I.; Hupp, J. T.; Farha, O. K.; Yildirim, T. *J. Am. Chem. Soc.* **2013**, *135*, 11887.

126. He, Y.; Zhou, W.; Qian, G.; Chen, B. *Chem. Soc. Rev*. **2014**, *43*, 5657.

127. Jayaramulu, K.; Datta, K. K. R.; Shiva, K.; Bhattacharyya, A. J.; Eswaramoorthy, M.; Maji, T. K. *Microporous Mesoporous Mater*. **2015**, *206*, 127.

128. Roy, S.; Chakraborty, A.; Maji, T. K. *Coord. Chem. Rev*. **2014**, *139*, 273.

129. Haldar, R.; Prasad, K.; Samanta, P. K.; Pati, S.; Maji, T. K. *Cryst. Growth Des*. **2016**, *16*, 82.

130. Li, B.; Chrzanowski, M.; Zhang, Y.; Ma, S. *Coord. Chem. Rev*. **2016**, *307*, 106.

131. Samai, S.; Biradha, K. *Chem Mater*. **2012**, *24*, 1165.

132. Dey, A.; Mandal, S. K.; Biradha, K. *CrystEngComm* **2013**, *15*, 9769.

133. Liu, J.; Thallapally, P. K.; McGrail, B. P.; Brown, D. R.; Liu, J. *Chem. Soc. Rev.* **2012**, *41*, 2308.

134. Gygi, D.; Bloch, E. D.; Mason, J. A.; Hudson, M. R.; Gonzalez, M. I.; Siegelman, R. L.; Darwish, T. A.; Queen, W. L.; Brown, C. M.; Long, J. R. *Chem. Mater.* **2016**, *28*, 1128.

135. Mason, J. A.; Veenstra, M.; Long, J. R. *Chem. Sci*. **2014**, *5*, 32.

136. Banerjee, A.; Nandi, S.; Nasa P.; Vaidhyanathan, R. *Chem Commun*., **2016**, *52*, 1851.

137. Nandi, S.; Collins, S. P.; Chakraborty, D.; Banerjee, D.; Thallapally, P. K.; Woo, T. K.; Vaidhyanathan, R. *J. Am. Chem. Soc*., **2017**, *139*, 1734.

138. Qiu, S.; Xue, M.; Zhu, G. *Chem. Soc. Rev*. **2014**, *43*, 6116.

139. Nugent, P.; Belmabkhout, Y.; Burd, S. D.; Cairns, A. J.; Luebke, R.; Forrest, K.; Pham, T.; Ma, S.; Space, B.; Wojtas, L.; Eddaoudi, M.; Zaworotko, M. J. *Nature* **2013**, *495*, 80.

140. Li, J.-R.; Sculley, J.; Zhou, H.-C. *Chem. Rev*. **2012**, *112*, 869.

141. Li, J.-R.; Kuppler, R. J.; Zhou, H.-C. *Chem. Soc. Rev*. **2009**, *38*, 1477.

142. Huang, A.; Chen, Y.; Wang, N.; Hu, Z.; Jiang, J.; Caro, J. *Chem. Commun*. **2012**, *48*, 10981.

143. Herm, Z. R.; Wiers, B. M.; Mason, J. A.; van Baten, J. M.; Hudson, M. R.; Zajdel, P.; Brown, C. M.; Masciocchi, N.; Krishna, R.; Long, J. R. *Science* **2013**, *340*, 960.

144. Biswal, B. P.; Bhaskar, A.; Banerjee, R.; Kharul, U. K. *Nanoscale* **2015**, *7*, 7291.

145. Thallapally, P. K.; Tian, J.; RadhaKishan, M.; Fernandez, C. A.; Dalgarno, S. J.; McGrail, P. B.; Warren, J. E.; Atwood, J. L. *J. Am. Chem. Soc*. **2008**, *130*, 16842.

146. Nandi, S.; Luna, P. D.; Daff, T. D.; Rother J.; Liu M.; Buchanan W.; Hawari, A. I.; Woo T. K.; Vaidhyanathan, R. *Sci. Adv*., **2015**, 1:e1500421.

147. Bhatt, P. M.; Belmabkhout, Y.; Cadiau, A.; Adil, K.; Shekhah, O.; Shkurenko, A.; Barbour, L. J.; Eddaoudi, M. *J. Am. Chem. Soc*. **2016**, *138*, 9301.

148. Kumar, A.; Hua, C.; Madden, D. G.; O'Nolan, D.; Chen, K. –J.; Keane, L. –A. J.; Perry IV, J. J.; Zaworotko, M. J. *Chem. Commun*. **2017**, *53*, 5946.

149. Lin, J. B.; Zhang J.-P.; Chen, X. M. *J. Am. Chem. Soc*. **2010**, *132*, 6654.

150. Mason, J. A.; Sumida, K.; Herm, Z. R.; Krishna, R.; Long, J. R. *Energy Environ. Sci*. **2011**, *4*, 3030.

151. Zhang, Z.; Yao, Z. -Z.; Xiang, S.; Chen, B. *Energy Environ. Sci*. **2014**, *7*, 2868.

152. Xiang, S.; He, Y.; Zhang, Z.; Wu, H.; Zhou, W.; Krishna, R.; Chen, B. *Nat. Commun*. **2012**, *3*, 954.

153. Vaidhyanathan, R.; Iremonger, S. S.; Shimizu, G. K. H.; Boyd, P. G.; Alavi, S.; Woo, T. K. *Science* **2010**, *330*, 650.

154. Kreno, L. E.; Leong, K.; Farha, O. K.; Allendorf, M.; Van Duyne, R. P.; Hupp, J. T. *Chem. Rev*. **2012**, *112*, 1105.

155. Nagarkar, S. S.; Joarder, B.; Chaudhari, A. K.; Mukherjee, S.; Ghosh, S. K. *Angew. Chem., Int. Ed*. **2013**, *52*, 2881.

156. Chen, B.; Wang, L.; Xiao, Y.; Fronczek, F. R.; Xue, M.; Cui, Y.; Qian, G. *Angew. Chem., Int. Ed*. **2009**, *48*, 500.

157. Chen, B.; Xiang, S.; Qian, G. *Acc. Chem. Res*. **2010**, *43*, 1115.

158. Lu, G.; Hupp, J. T. *J. Am. Chem. Soc*. **2010**, *132*, 7832.

159. Sutar, P.; Maji, T. K. *Chem. Commun*. **2016,** *52*, 8055.

160. Roy, S.; Katiyar, A. K.; Mondal, S. P.; Ray, S. K.; Biradha, K. *ACS Appl. Mater. Interfaces* **2014**, *6*, 11493.

161. Cui, Y.; Yue, Y.; Qian, G.; Chen, B. *Chem. Rev*. **2012**, *112*, 1126.

162. Kundu, T.; Mitra, S.; DíazDíaz, D.; Banerjee, R. *ChemPlusChem* **2016**, *81*, 728.

163. Banerjee, K.; Biradha, K. *New J. Chem*. **2016**, *40*, 1997.

164. Marshall, R. J.; Kalinovskyy, Y.; Griffin, S. L.; Wilson, C.; Blight, B. A.; Forgan, R. S. *J. Am. Chem. Soc*. **2017**, *139*, 6253.

165. Yang, Q.-Y.; Pan, M.; Wei, S.-C.; Li, K.; Du, B.-B.; Su, C.-Y. *Inorg. Chem*. **2015,** *54*, 5707.

166. Zhao, Y.; Song, Z.; Li, X.; Sun, Q.; Cheng, N.; Lawes, S.; Sun, X. *Energy Storage Materials* **2016**, *2*, 35.

167. Shao, M.; Chang, Q.; Dodelet, J.-P.; Chenitz, R. *Chem. Rev*. **2016**, *116*, 3594.

168. Mahmood, A.; Guo, W.; Tabassum, H.; Zou, R. *Adv. Energy Mater*. **2016**, *6*, 1600423.

169. Ma, S.; Goenaga, G. A.; Call, A. V.; Liu, D.-J. *Chem. - Eur. J*. **2011**, *17*, 2063.

170. Ke, F.-S.; Wu, Y.-S.; Deng, H. *Journal of Solid State Chemistry* **2015**, *223*, 109.

171. Lin, X.-M.; Ni, J.-L.; Lin, J.; Wei, L.-M.; Hu, L.; Zhang, G.; Cai, Y.-P. *Inorg. Chem*. **2016**, *55*, 8244.

172. Peng, Z.; Yi, X.; Liu, Z.; Shang, J.; Wang, D. ACS *Appl. Mater. Interfaces* **2016**, *8*, 14578.

173. Sun, L.; Campbell, M. G.; Dincă, M. *Angew. Chem, Int. Ed*. **2016**, *55*, 3566.

174. Wang, L.; Han, Y.; Feng, X.; Zhou, J.; Qi, P.; Wang, B. *Coord. Chem. Rev*. **2016**, *307*, 361.

175. Givaja, G.; Amo-Ochoa, P.; Gomez-Garcia, C. J.; Zamora, F. *Chem. Soc. Rev*. **2012**, *41*, 115.

176. Dhara, B.; Nagarkar, S. S.; Kumar, J.; Kumar, V.; Jha, P. K.; Ghosh, S. K.; Nair, S.; Ballav, N. *J. Phys. Chem. Lett*. **2016**, *7*, 2945.

177. Sun, L.; Hendon, C. H.; Park, S. S.; Tulchinsky, Y.; Wan, R.; Wang, F.; Walsh, A.; Dinca, M.; *Chem. Sci*. **2017**, *8*, 4450.

178. Shimizu, G. K. H.; Taylor, J. M.; Kim, S. *Science* **2013**, *341*, 354.

179. Nagarkar, S. S.; Unni, S. M.; Sharma, A.; Kurungot, S.; Ghosh, S. K. *Angew. Chem., Int. Ed.* **2014**, *53*, 2638.

180. Saha, S.; Schön, E.-M.; Cativiela, C.; DíazDíaz, D.; Banerjee, R. *Chem. - Eur. J*. **2013**, *19*, 9562.

181. Sikdar, N.; Dutta, D.; Haldar, R.; Ray, T.; Hazra, A.; Bhattacharyya, A. J.; Maji, T. K. J. *Phys. Chem. C* **2016**, *120*, 13622.

182. Aiyappa, H. B.; Saha, S.; Wadge, P.; Banerjee, R.; Kurungot, S. *Chem. Sci*. **2015**, *6*, 603.

183. Zhang, F.-M.; Dong, L.-Z.; Qin, J.-S.; Guan, W.; Liu, J.; Li, S.-L.; Lu, M.; Lan, Y.- Q.; Su, Z.-M.; Zhou, H.-C. *J. Am. Chem. Soc*. **2017**, *139*, 6183.

184. Yoon, M.; Suh, K.; Natarajan, S.; Kim, K. *Angew. Chem. Int. Ed*. **2013**, *52*, 2688.

185. Pili, S.; Argent, S. P.; Morris, C. G.; Rought, P.; García-Sakai, V.; Silverwood, I. P.; Easun, T. L.; Li, M.; Warren, M. R.; Murray, C. A.; Tang, C. C.; Yang, S.; Schröder, M. *J. Am. Chem. Soc*. **2016**, *138*, 6352.

186. Nandi, S.; Dhavale, V. M.; Shalini, S.; Werner-Zwanziger, U.; Singh, H.; Kurungot S.; Vaidhyanathan, R. *Adv. Mater. Interf*., **2015**, *2*, 1500301.

187. Horike, S.; Umeyama, D.; Kitagawa, S. *Acc. Chem. Res.* **2013**, *46*, 2376.

188. Li, A.; Gao, Q.; Xu, J.; Bu, X. Coord. Chem. Rev. **2017**, *344*, 54.

189. Sadakiyo, M.; Yamada, T.; Kitagawa, H. *J. Am. Chem. Soc*. **2009**, *131*, 9906.

190. Bureekaew, S.; Horike, S.; Higuchi, M.; Mizuno, M.; Kawamura, T.; Tanaka, D.; Yanai N.; Kitagawa, S. *Nat. Mater*. **2009**, *8*, 831.

191. Hurd J. A.; Vaidhyanathan R.; Thangadurai V.; Ratcliffe C. I.; Moudrakovski I. L.; Shimizu G. K. H. *Nat.Chem*., **2009**, *1*, 705.

192. Phang, W. J.; Jo, H.; Lee, W. R.; Song, J. H.; Yoo, K.; Kim B. S.; Hong, C. S. *Angew. Chem., Int. Ed.*, **2015**, *54*, 5142.

193. Laberty-Robert, C.; Vallé, K.; Pereira F.; Sanchez C. *Chem. Soc. Rev*., **2011**, *40*, 961.

194. Sadakiyo M.; Yamada T.; Kitagawa H. *ChemPlusChem* **2016**, *81*, 691.

195. Dong, X. Y.; Wang, R.; Wang, J. Z.; Zang S. Q.; Mak, T. C. W. J. *Mater. Chem. A*, **2015**, *3*, 641.

196. Zhao, S. N.; Song, X. Z.; Zhu, M.; Meng, X.; Wu, L. L.; Song, S. Y.; Wang C.; Zhang, H. J. *Dalton Trans*., **2015**, *44*, 948.

197. Zheng, G. L.; Yang, G. C.; Song, S. Y.; Song X. Z.; Zhang, H. J. *CrystEngComm*, **2014**, *16*, 64.

198. Zhou, L. J.; Deng, W. H.; Wang, Y. L.; Xu, G.; Yin S. G.; Liu, Q. Y. *Inorg. Chem*., **2016**, *55*, 6271.

199. Dong, X. Y.; Wang, R.; Li, J. B.; Zang, S. Q.; Hou, H. W.; Mak, T. C. W. *Chem. Commun*., **2013**, *49*, 10590.

200. Meng, X.; Song, S. Y.; Song, X. Z.; Zhu, M.; Zhao, S. N.; Wu L. L.; Zhang, H. J. *Chem. Commun*., **2015**, *51*, 8150.

201. Taylor, J. M.; Mah, R. K.; Moudrakovski, I. L.; Ratcliffe, C.I.; Vaidhyanathan, R.; Shimizu, G. K. H. *J. Am. Chem. Soc.* **2010**, *132*,14055.

202. Colodrero, R. M. P.; Papathanasiou, K. E.; Stavgianoudaki, N.; Olivera-Pastor, P.; Losilla, E. R.; Aranda, M. A. G.; Leo´n-Reina, L.; Sanz, J.; Sobrados, I.; Choquesillo-Lazarte, D.; Garcı´a-Ruiz, J. M.; Atienzar, P.; Rey, F.; Demadis K. D.; Cabeza, A. *Chem. Mater.*, **2012**, *24*, 3780.

203. Taylor, J. M.; Dawson K. W.; Shimizu, G. K. H. *J. Am. Chem. Soc*., **2013**, *135*, 1193.

204. Bao, S. S.; Li, N. Z.; Taylor, J. M.; Shen, Y.; Kitagawa H.; Zheng, L. M. *Chem. Mater*., **2015**, *27*, 8116.

205. Begum, S.; Wang, Z. Y.; Donnadio, A.; Costantino, F.; Casciola, M.; Valiullin, R.; Chmelik, C.; Bertmer, M.; Krger, J.; Haase J.; Krautscheid, H. *Chem. – Eur. J*., **2014**, *20*, 8862.

206. Maxim, C.; Ferlay, S.; Tokoro, H.; Ohkoshid S. I.; Train, C. *Chem. Commun*., **2014**, *50*, 5629.

207. Tominaka, S.; Coudert, F. X.; Dao, T. D.; Nagao T.; Cheetham, A. K. *J. Am. Chem. Soc.*, **2015**, *137*, 6428.

208. Tang, Q.; Liu, Y. W.; Liu, S. X.; He, D. F.; Miao, J.; Wang, X. Q.; Yang, G. C.; Shi Z.; Zheng, Z. P. *J. Am. Chem. Soc*., **2014**, *136*, 12444.

209. Sadakiyo, M.; Yamada, T.; Honda, K.; Matsui H.; Kitagawa, H. *J. Am. Chem. Soc.*, **2014**, *136*, 7701.

210. Sadakiyo, M.; Yamada T.; Kitagawa, H. *J. Am. Chem. Soc*., **2014**, *136*, 13166.

211. O¯ kawa, H.; Sadakiyo, M.; Yamada, T.; Maesato, M.; Ohba M.; Kitagawa, H. *J. Am. Chem. Soc.*, **2013**, *135*, 2256.

212. O¯ kawa, H.; Sadakiyo, M.; Otsubo, K.; Yoneda, K.; Yamada, T.; Ohba M.; Kitagawa, H. *Inorg. Chem*., **2015**, *54*, 8529.

213. Dong, X. Y.; Hu, X. P.; Yao, H. C.; Zang, S. Q.; Hou H. W.; Mak, T. C. W. *Inorg. Chem*., **2014**, *53*, 12050.

214. Meng, X.; Song, X. Z.; Song, S. Y.; Yang, G. C.; Zhu, M.; Hao, Z. M.; Zhao S. N.; Zhang, H. J. *Chem. Commun*., **2013**, *49*, 8483.

215. Hao, Z.; Yang, G.; Song, X.; Zhu, M.; Meng, X.; Zhao, S.; Song S.; Zhang, H. *J. Mater. Chem. A*, **2014**, *2*, 237.

216. Gil-Herna´ndez, B.; Savvin, S.; Makhloufi, G.; Nu´n˜ez, P.; Janiak C.; Sanchiz, J. *Inorg. Chem*., **2015**, *54*, 1597.

217. Wang, R.; Dong, X. Y.; Xu, H.; Pei, R. B.; Ma, M. L.; Zang, S. Q.; Hou H. W.; Mak, T. C. W. *Chem. Commun*., **2014**, *50*, 9153.

218. Taylor, J. M.; Komatsu, T.; Dekura, S.; Otsubo, K.; Takata M.; Kitagawa, H. *J. Am. Chem. Soc.*, **2015**, *137*, 11498.

219. Yang, F.; Huang, H. L.; Wang, X. Y.; Li, F.; Gong, Y. H.; Zhong C. L.; Li, J. R. *Cryst. Growth Des*., **2015**, *15*, 5827.

220. Taylor, J. M.; Dekura, S.; Ikeda R.; Kitagawa, H. *Chem. Mater*., **2015**, *27*, 2286.

221. Bazaga-Garcı´a, M.; Colodrero, R. M. P.; Papadaki, M.; Garczarek, P.; Zon´, J.; Olivera-Pastor, P.; Losilla, E. R.; Leo´n-Reina, L.; Aranda, M. A. G.; Choquesillo-Lazarte, D.; Demadis K. D.; Cabeza, A. *J. Am. Chem. Soc*., **2014**, *136*, 5731.

222. Gao, Y.; Broersen, R.; Hageman, W.; Yan, N.; Mittelmeijer-Hazeleger, M.C.; Rothenberg G.; Tanase, S. *J. Mater. Chem. A*, **2015**, *3*, 22347.

223. Zhu, M.; Hao, Z. M.; Song, X. Z.; Meng, X.; Zhao, S. N.; Songa S. Y.; Zhang, H. J. *Chem. Commun*., **2014**, *50*, 1912.

224. Sanda, S.; Biswas S.; Konar, S. *Inorg. Chem*., **2015**, *54*, 1218.

225. Kim, S. R.; Dawson, K. W.; Gelfand, B. S.; Taylor J. M.; Shimizu, G. K. H. *J. Am. Chem. Soc.*, **2013**, *135*, 963.

226. Tu, T. N.; Phan, N. Q.; Vu, T. T.; Nguyen, H. L.; Cordova K. E.; Furukawa, H. *J. Mater. Chem. A*, **2016**, *4*, 3638.

227. Zhao, X.; Mao, C. Y.; Bu X. H.; Feng, P. Y. *Chem. Mater*., **2014**, *26*, 2492.

228. Yamada, T.; Sadakiyo, M; Kitagawa, H. *J. Am. Chem. Soc*. **2009**, *131*, 3144.

229. Sadakiyo, M.; Okawa, H.; Shigematsu, A.; Ohba, M.; Yamada, T.; Kitagawa, H. *J. Am. Chem. Soc.* **2012**, *134*, 5472.

230. Okawa, H.; Shigematsu, A.; Sadakiyo, M.; Miyagawa, T.; Yoneda, K.; Ohba, M.; Kitagawa, H. *J. Am. Chem. Soc*. **2009**, *131*, 13516.

231. Yamada T.; Nankawa, T. *Inorg.Chem*. **2016**, *55*, 8267.

232. Wang, X.; Qin, T.; Bao, S.; Zhang, Y.; Shen, X.; Zhengband L.; Zhu, D. *J. Mater. Chem. A*, **2016**, *4*, 16484.

233. Zhang, K.; Xie, X.; Li, H.; Gao, J.; Nie, L.; Pan, Y.; Xie, J.; Tian, D.; Liu, W.; Fan, Q.; Su, H.; Huang, L.; Huang, W. *Adv. Mater*. **2017,** *29*, 1701804.

234. Pardo, E.; Train, C.; Gontard, G.; Boubekeur, K.; Fabelo, O.; Liu, H.; Dkhil, B.; Lloret, F.; Nakagawa, K.; Tokoro, H.; Ohkoshi, S.; Verdaguer, M.; *J. Am. Chem. Soc*. **2011**, *133*, 15328.

235. Mon, M.; Vallejo, J.; Pasán, J.; Fabelo, O.; Train, C.; Verdaguer, M.; Ohkoshi, S.; Tokoro, H.; Nakagawae K.; Pardo, E. *Dalton Trans*., **2017**, *46*, 15130.

236. Shigematsu, A.; Yamada, T.; Kitagawa, H.; *J. Am. Chem. Soc*. **2011**, *133*, 2034.

237. Jeong, N. C.; Samanta, B.; Lee, C. Y.; Farha, O. K.; Hupp, J. T. *J. Am. Chem. Soc*. **2012**, *134*, 51.

238. Umeyama, D.; Horike, S.; Inukai, M.; Hijikata Y.; Kitagawa, S. *Angew. Chem., Int. Ed*., **2011**, *50*, 11706.

239. Eisbein, E.; Joswig J.-O.; Seifert, G. *J. Phys. Chem. C*, **2014**, *118*, 13035.

240. Inukai, M.; Horike, S.; Umeyama, D.; Hijikata Y.; Kitagawa, S.; *Dalton Trans*., **2012**, *41*, 13261.

241. Panda, T.; Kundu T.; Banerjee, R. *Chem. Commun*., **2013**, *49*, 6197.

242. Agmon, N. *Chem. Phys. Lett*. **1995,** *244*, 456.

243. Kreuer, K.-D.; Rabenau, A.; Weppner, W. *Angew. Chem. Int. Ed*. **1982**, *21*, 208.

244. Colomban, P.; Novak, A. *J. Mol. Struct*. **1988**, *177*, 277.

245. Dawson, K. W. Thesis, **2013**, Department of Chemistry, Calgary.

246. Xu, H.-R.; Zhang, Q.-C.; Zhao, H.-X.; Long, L.-S.; Huang, R.-B.; Zheng, L.-S. *Chem. Commun.* **2012**, *48*, 4875.

Chapter 2

Structure and Proton Conduction of Three Structurally Related Metal Organic Frameworks

2018

Content of this chapter is published in the following article:

Scientific Reports, **2016**, *6*, Article number: 32489 https://www.nature.com/articles/srep32489

2.1. Introduction

As discussed in chapter 1, the fuel cells are a key candidate in the quest of alternative renewable, safe, clean, and plentiful energy resources[1]. Various attempts are being made to improve the performance of the existing fuel cell technology which involves research to improve the properties of catalysts/electrodes, membranes/electrolytes, Membrane Electrode Assemblies (MEA), cells and other stack components[2]. New materials are being explored as electrode or electrolyte candidates for the same.

Metal Organic Frameworks (MOFs) have been studied for many applications[3-8], but their use as proton-conducting electrolyte membranes is very recent and is being studied expansively[9-12]. Being stable crystalline materials, they have proven to be great systems for compartmentalizing the effects of various structural components on the overall proton conductivity of such materials[11,13,14]. A facile and very effective approach to alter the proton conduction is by introducing amphoteric guests which can provide a continuous proton conducting pathway via dense, and extensive hydrogen-bonding interactions. These strategies have allowed the realization of noteworthy improvement in the proton conductivity values even in many classical polymers[15-19]. Although this has been achieved in polymers, there still is a problem that their amorphous character makes it very difficult to get structural insights and therefore restricts the ability to get a structure-property correlation. On the contrary, MOFs have highly ordered porous and crystalline structure which can easily be exploited. Shimizu and co-workers[20] and Kitagawa and co-workers[21] in their pioneering works incorporated extra-framework amphoteric proton-bearing species to achieve high temperature (100–200˚C) proton conductivity. Most importantly, their approach when coupled with the enormous wealth of atomic level details presented from the single-crystal structure of these MOFs led to the generation of superior Proton Conducting MOFs (PCMOFs)[22,23] via customized hydrogen-bonding pathways.

The protic guests can be loaded in the MOFs in two ways. They can either be made a part of the framework so that they coordinate with the metal and line the pore walls or they can be incorporated as extra-framework species in the pores of the MOF (Figure 2.1).

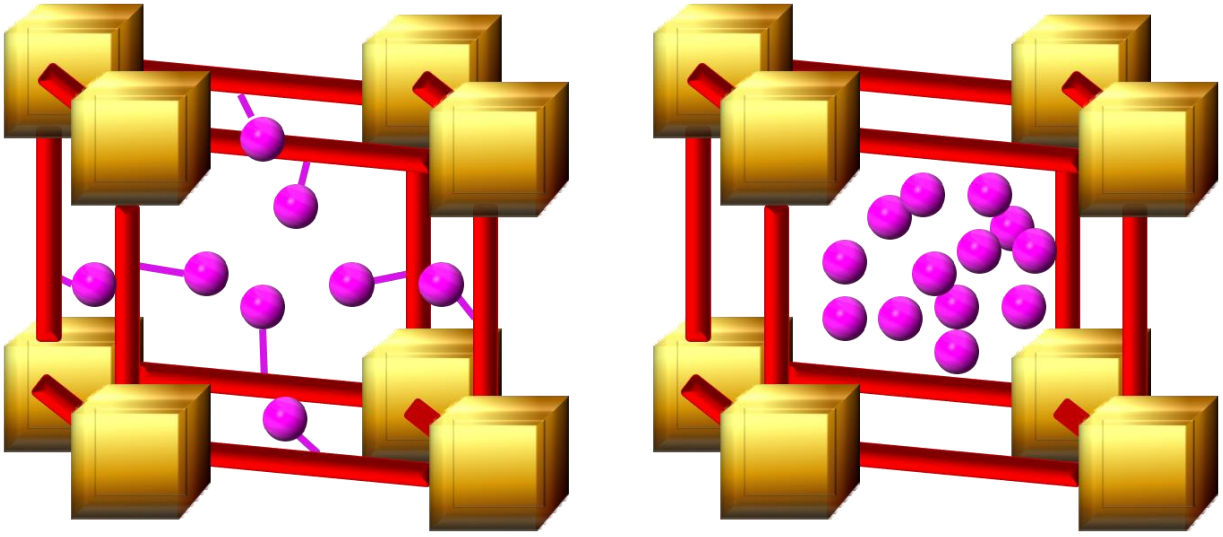

Figure 2.1. Two ways to incorporate the protic species in a MOF; either as a part of the framework (left) or as an extra-framework guest (right).

Due to the availability of a vast number of guest species and easy loading methods, which is generally achieved by soaking the MOF in the guest-solution or exposing the MOF to the guest in the vapor phase, these approaches certainly have versatility[20,21]. The basicity of these guests, their orientation with respect to the framework moieties, and position seem to play a very key role in achieving the low activation energies and high proton conductivity values[9,11,12,14]. Achieving the loading of guest as an extra-framework species is easier, but that might lead to the leaching of these guests under the fuel cell operating conditions. In most of the reported cases, the hydrogen-bond pathway has a protic guest which is not coordinated to the metal and acts as an 'extra-framework' hydrogen-bond point[14,24,25]. However, if the protic groups can be made a part of the framework by coordinating it to the metal node, it brings in additional advantages[26], particularly in achieving no-leaching and consistent guest loading regarding its composition. This supports stoichiometric loading of the proton bearing species, which in turn impacts the consistent and reproducible performance and life of the electrolyte material. Also, the guests normally used by the many research groups are very acidic in nature[27], which prove to be a handling hazard as well as not all the MOFs are stable under such acidic conditions. Therefore, using a coordinating and a relatively mild acid seems to be a good and easy approach to achieve high proton conductivities.

As mentioned earlier, a key role is played by the hydrogen bonds in deciding the extent and the kinetics of the proton transfer for proton conduction in these crystalline materials. For realizing acceptable conductivity values, a major prerequisite is the percolation of these dense hydrogen-bonded pathways and the necessity for the proton-transporting components to have well-suited acid-base character. Recently many MOF electrolytes have been reported with the potential to deliver high proton conductivities of the order of 10^{-2} S/cm[23,27,28-32] which has triggered a real interest to explore these materials to enhance the conductivities and push them to record levels.

With this backdrop, we present an approach wherein the 'zwitterionic' 4-hydroxy-pyridine/4-pyridinol has been used as a coordinating, relatively mildly acidic, protic moiety favoring stoichiometric non-leachable loading and considerable proton conductivities. Terephthalic acid has been used as another ligand to form extended frameworks. We have isolated two isostructural, dense, three-dimensional metal-terephthalate (m = Mg, Cd) frameworks with pyridinol coordinated to metal and also, a Nd-terephthalate which has a different but very closely related structure as pure phases. For easy understanding, the Mg, Cd, and Nd MOFs have been denoted as **1**, **2**, and **3** respectively. These isostructural/structurally related MOFs provide a good platform to grasp the structure-conductivity relationship in these MOFs which is controlled by the different components within them.

2.2. Materials and Methods:

All the organic chemicals were purchased from Sigma Aldrich. The metal salts were procured from Alfa Aesar. All reagents and solvents were used without any further purification.

2.2.1. Synthesis procedure

Milligram scale synthesis:

1 was synthesized hydrothermally using the approximate molar ratios of $Mg(NO_3)_2.6H_2O$, terephthalic acid and 4-hydroxypyridine as 1:1:2. In a Teflon liner, 0.1 g Magnesium nitrate was dissolved in 5 ml DMA. To this solution was about 0.08 g 4-hydroxypyridine was added. The mixture was stirred for 15 minutes at RT. To this 0.065 g of terephthalic acid was added. The contents were sealed in an autoclave and heated at 140˚C for 48

hours. It was slowly cooled down to room temperature. The product containing colorless, rod-shaped crystals was collected by filtration using methanol and acetone.

(Elemental analysis, observed/calculated: C – 54.80%/55.07%; H - 3.076%/3.19%; N– 4.82%/4.94%). The air-dried sample gave a yield of ~ 85% (based on Mg).

2 was synthesized hydrothermally using the approximate molar ratios of $Cd(NO_3)_2.4H_2O$, terephthalic acid and 4-hydroxypyridine as 1:1:2. In a Teflon liner, 0.1 g cadmium nitrate was dissolved in 5 ml DMF. To this solution about 0.06 g 4-hydroxypyridine was added. The mixture was stirred for 15 minutes at RT. To this 0.0538 g of terephthalic acid was added. The contents were sealed in an autoclave and heated at 100°C for 24 hours. It was slowly cooled down to room temperature. The product containing colorless, rod-shaped crystals was collected by filtration using methanol and acetone.

(Elemental analysis, observed/calculated: C – 42.65%/42.01%; H - 2.311%/2.44%; N – 3.73%/3.76%). The air-dried sample gave a yield of ~ 89% (based on Cd).

3 was synthesized hydrothermally using the approximate molar ratios of $Nd_2(CO_3)_3.xH_2O$, HNO_3, terephthalic acid and 4-hydroxypyridine as 1:3:1.5:3. In a Teflon liner, 60 µ l nitric acid was added to 0.1 g Neodymium carbonate and 5 ml DMF. To this solution about 0.12 g 4-hydroxypyridine was added. The mixture was stirred for 15 minutes at RT. To this 0.106 g of terephthalic acid was added. The contents were sealed in an autoclave and heated at 100˚C for 24 hours. It was then slowly cooled down to room temperature. The product containing bluish-pink very thin rod-shaped crystals was collected by filtration using methanol and acetone.

(Elemental analysis, observed/calculated: C – 42.18%/42.56%; H - 2.144%/2.80%; N – 3.99%/4.02%). The air-dried sample gave a yield of ~ 75% (based on Nd).

We could also prepare these samples on a gram scale with an easy scale-up procedure.

Gram scale synthesis:

1 was synthesized hydrothermally using the approximate molar ratios of $Mg(NO_3)_2.6H_2O$, terephthalic acid and 4-hydroxypyridine as 1:1:2. In a Teflon liner, 2 g

Magnesium nitrate was dissolved in 50 ml DMA. To this solution was added 1.6 g 4-hydroxypyridine. The mixture was stirred for 15 minutes at RT. To this 1.3g of terephthalic acid was added. The contents were sealed in an autoclave and heated at 140˚C for 48 hours. It was slowly cooled down to room temperature. The product containing colorless, rod-shaped crystals was collected by filtration using methanol and acetone.

2 was synthesized hydrothermally using the approximate molar ratios of $Cd(NO_3)_2.4H_2O$, terephthalic acid and 4-hydroxypyridine as 1:1:2. In a Teflon liner, 2 g cadmium nitrate was dissolved in 50 ml DMF. To this solution was added 1.2 g 4-hydroxypyridine. The mixture was stirred for 15 minutes at RT. To this 1.7g of terephthalic acid was added. The contents were sealed in an autoclave and heated at 100˚C for 24 hours. It was slowly cooled down to room temperature. The product containing colorless, rod-shaped crystals was collected by filtration using methanol and acetone.

3 was synthesized hydrothermally using the approximate molar ratios of $Nd_2(CO_3)_3.xH_2O$, HNO_3, terephthalic acid and 4-hydroxypyridine as 1:3:1.5:3. In a Teflon liner, 1.2 ml nitric acid was added to 2 g Neodymium carbonate and 50 ml DMF. To this solution about 2.4 g of 4-hydroxypyridine was added. The mixture was stirred for 15 minutes at RT. To this 2.12 g of terephthalic acid was added. The contents were sealed in an autoclave and heated at 100˚C for 24 hours. It was then slowly cooled down to room temperature. The product containing bluish-pink, very thin rod-shaped crystals was collected by filtration using methanol and acetone.

2.2.2. Characterization and analytical methods:

Single crystal structure determination:

Single-crystal data was collected on a Bruker SMART APEX four-circle diffractometer equipped with a CMOS photon 100 detector (Bruker Systems Inc.) and with a Cu Kα radiation (1.5418Å). The incident X-ray beam was focused and monochromated using Micro focus system (IμS). Crystal of **1**, **2** and **3** was mounted on nylon Cryo loops with Paratone-N oil. Data was collected at 173(2) K for **1** and **3**, and at 298 K for **2**. Data was integrated using Bruker SAINT Software and was corrected for absorption using SADABS. The structure was solved by Intrinsic Phasing module of the Direct methods and refined using the SHELXTL 2014 software suite. All

non-hydrogen atoms were located from an iterative examination of difference F-maps following which the structure was refined using the least-squares method. Hydrogen atoms were placed geometrically riding mode (CIF file: CCDC 1041840-1041842).

Powder X-ray diffraction:

Powder XRD was carried out using a Rigaku Miniflex-600 instrument and processed using the PDXL2 software. Variable temperature PXRDs were measured under vacuum on Bruker instrument.

Thermogravimetric analysis:

Thermogravimetry was carried out on NETSZCH TGA-DSC system. The TGAs were done under N_2 gas flow (20ml/min) (purge + protective), and samples were heated from RT to 550˚C at 2 K/min.

Impedance measurements:

The Bio-Logic (VMP-3) model was used to carry out the impedance measurements. The impedance spectra were recorded by applying a range of frequency from 1 MHz to 100 mHz with an amplitude of 10 mV. Moreover, ESPEC chamber was used to maintain the temperature and humidity during measurement.

Field emission SEM:

Ultra Plus Field Emission Scanning Electron Microscope with integral charge compensator and embedded EsB and AsB detectors was used to record the images. Oxford X-max instruments 80mm^2. (Carl Zeiss NTS, Gmbh), Imaging conditions: 2kV, WD=2 mm, 200 kX, Inlens detector.

Gas adsorption analysis:

The gas sorption isotherms were measured on a 3-FLEX (Micromeritics) instrument using ultra-high purity gases (≥ 4.8 grade). ~100 mg of the sample was transferred to analysis glass tube and evacuated at 120°C on the degas port for 24 hrs (10-6mbar), at which point the outgas rate was ≤ 2 μbar/min.

2.3. Results and Discussion

2.3.1. Structure of the proton conducting metal organic frameworks (1–3)

1 and **2** crystallize in monoclinic C2/c space group (**1:** a= 19.7578 Å, b= 9.1256 Å, c= 7.2153 Å, β= 106.366˚, V = 1248.22 $Å^3$; **2**: a= 20.1275 Å, b= 9.38985 Å, c= 7.3994 Å, β= 105.333˚, V = 1349.91 $Å^3$). The structure of **1**, i.e., $Mg(C_8O_4H_4)(C_5NOH_5)$ is formed by metal-oxygen chains, running along c-axis, made up of the metal and the oxygens of μ-2 bridging 4-pyridinol (PyOH) and the carboxylates of terephthalic acid (Figure 2.2 a). Four of these chains are connected by the terephthalate units to form 1-D channels along the c-axis (Figure 2.2 b). These channels are rhombic shaped and are filled with terminally coordinated 4-pyridinol units. The pyridinols protrude into the channels and are positioned along the c-axis. Being coordinating in nature, they line the bottom and top of the channel giving a zig-zag arrangement to the pyridyl groups running along the 1-dimensional channels. More importantly, these pendant pyridinols are protonated. Compound **2**, $Cd(C_8O_4H_4)(C_5NOH_5)$ is isostructural to**1** (Figures 2.2 c and d).

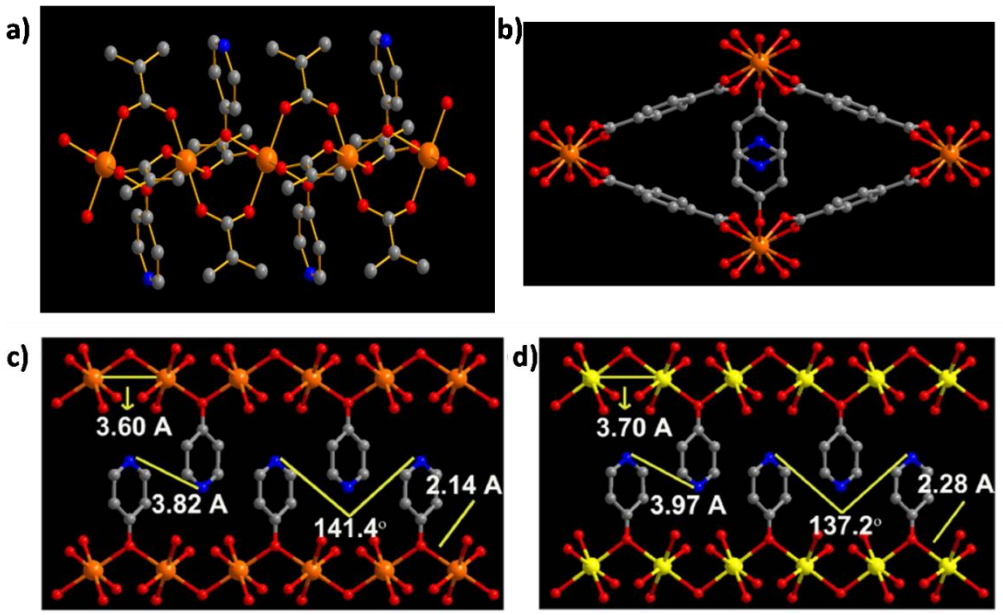

Figure 2.2. (a) Structure of **1** showing the chains formed by the metal and oxygen from pyridinol and terephthalates. (b) The rhombic shaped channels filled with terminally coordinated pyridinol units. (c and d) Figure showing the chains in **1** and **2** and the similarity between them can be seen from the distances and angles. The terephthalate ligands have been omitted for clarity. Color code: Mg– Orange; Cd– Yellow; C– Grey; O– Red; N– Blue.

Meanwhile, **3** crystallizes in triclinic P-1 space group (a= 10.2815 Å, b= 10.3597 Å, c= 11.1009 Å, α= 98.924˚, β= 90.1562˚, γ= 14.995˚, V = 1055.60 $Å^3$). **3**, $Nd_2(C_8O_4H_4)_3(C_5NOH_5)_2.(DMF)_X$ has a slightly different structure. It has a different building unit, i.e., a Nd_2 dimer. The dimers are made of two 9-coordinated Nd centers, both having three different types of carboxylates: a μ-2 bridging monodentately chelating, a bidentately coordinated, and a μ-2 bridging mono and bidentately chelating carboxylate. (Figure 2.3 a). In addition, both the Nd centers have coordination from a DMF molecule and a terminal pyridinol unit. The terephthalate ligand connects these dimers to complete the 3-dimensional structure with a narrow 1-dimensional channel running along the c-axis. The channels are filled by pyridinol and coordinated DMF molecules (Figure 2.3 b).

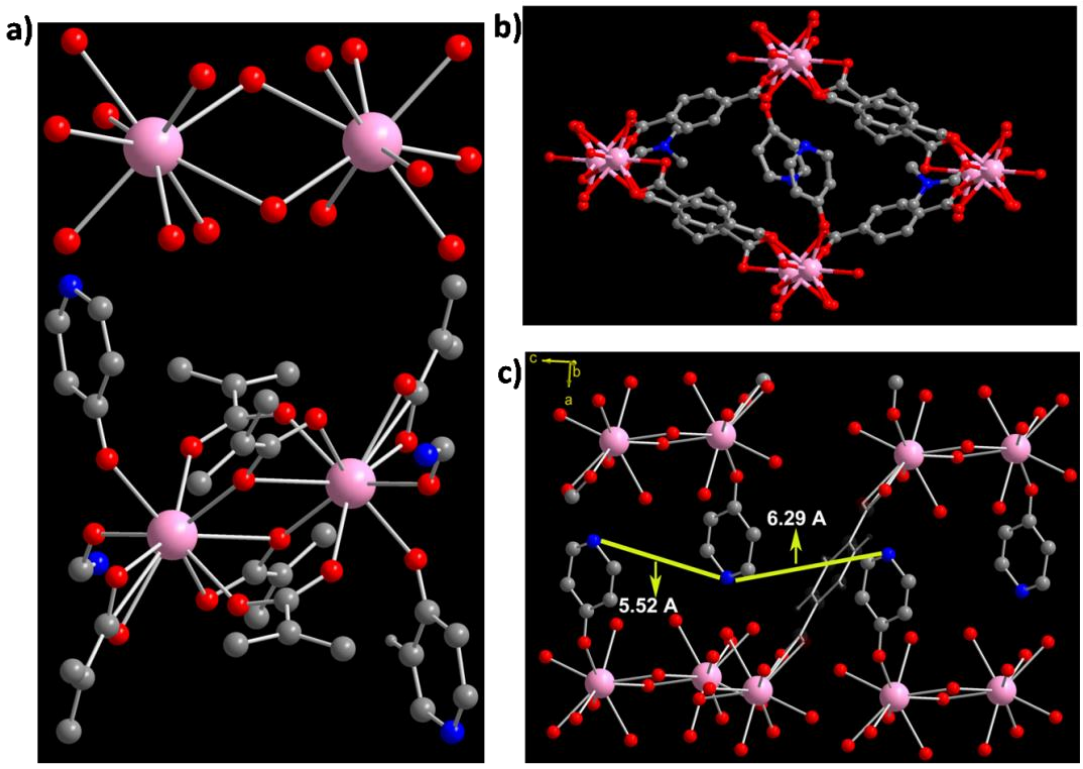

Figure 2.3. (a) Structure of **3** showing 9-coordinated Nd_2 dimers, the different binding modes of the terephthalate units, and also the presence of monodentately bound pyridinols and DMF molecules. (b) 1-D channel of **3** decorated with pyridinol units. (c) A column of dimers in **3** showing the arrangement of pyridinols along the column. Color code: Nd- Pink, O- red, N- blue, C-Grey.

The obvious difference is that the pyridinol in **3** is not μ-2 bridging as well as coordinated DMF is absent in **1** and **2**. The pyridyl ends in **1**, **2** and **3** are protonated. As shown in figure 2.2,

the adjacent pyridinols in **1** and **2** are held in position by π -π interactions (π -π distance = ~3.6–3.9 Å). The distance between the pyridinols in **3** is larger when compared to that of **1** and **2** (Compare Figures 2.2 c, d, and 2.3 c). However, this might open up a lot of space for the water molecules to come in and form hydrogen bonds with pyridinols under the humid conditions.

2.3.2. Bulk phase characterization

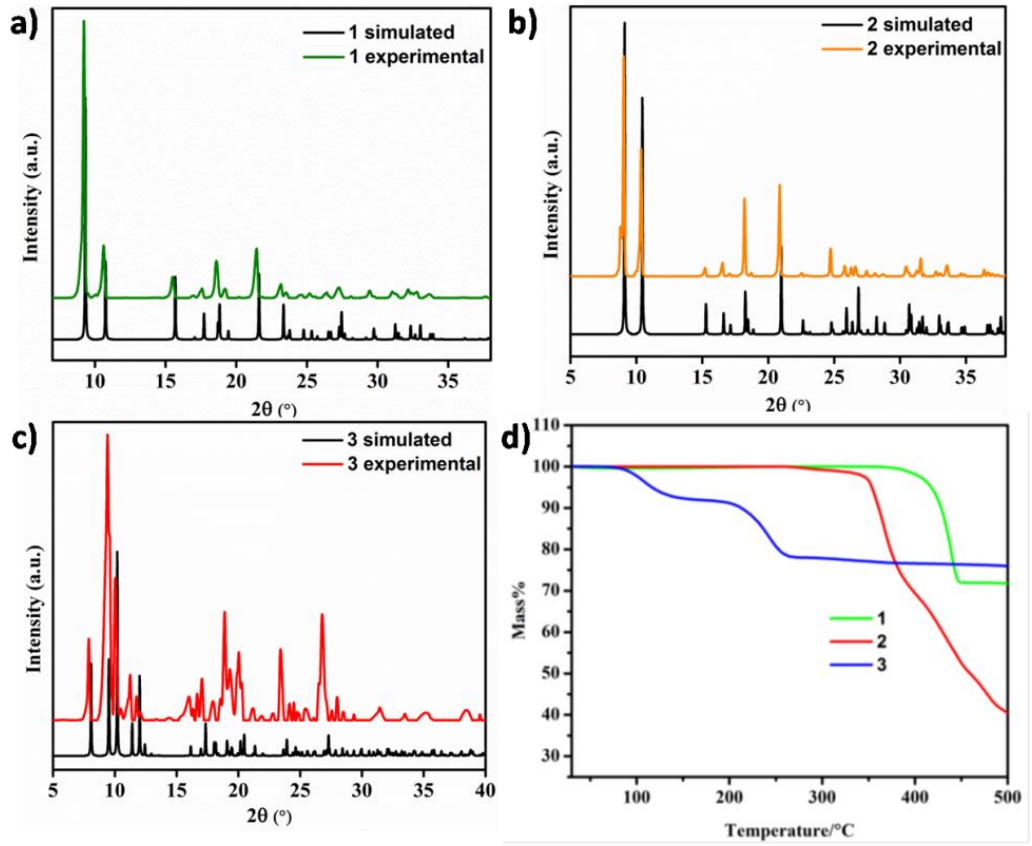

Figure 2.4. Bulk phase characterization. (a, b, c) PXRD comparison for **1**, **2,** and **3** respectively. (d) TGA comparison of **1, 2,** and **3**.

All the three MOFs were isolated as pure phases. The powder X-ray pattern for the three MOFs matched well with the simulated patterns. The comparatively broader peaks for **3** are most probably due to the fluorescence from the sample, which is very common for lanthanide MOFs (Figure 2.4). The bulk compositions of these MOFs proving the stoichiometric loading of the protic pyridinol moieties have been confirmed from TGA and CHN analysis (Figures 2.4 and section 2.2.1). The repeated synthesis, as well as the gram scale synthesis, produced samples with the similar PXRD and TGA profiles. For **1**, a weight loss of 33.50 % between 350 to 450˚C

in the TGA profile corresponds to the loss of coordinated pyridinol. Similarly, a weight loss of 25.59 % from 350 to 380˚C in **2** and a weight loss of ~16 % at 200˚C in **3** correspond to the pyridinol loss in the two phases.

2.3.3. Proton conductivity studies

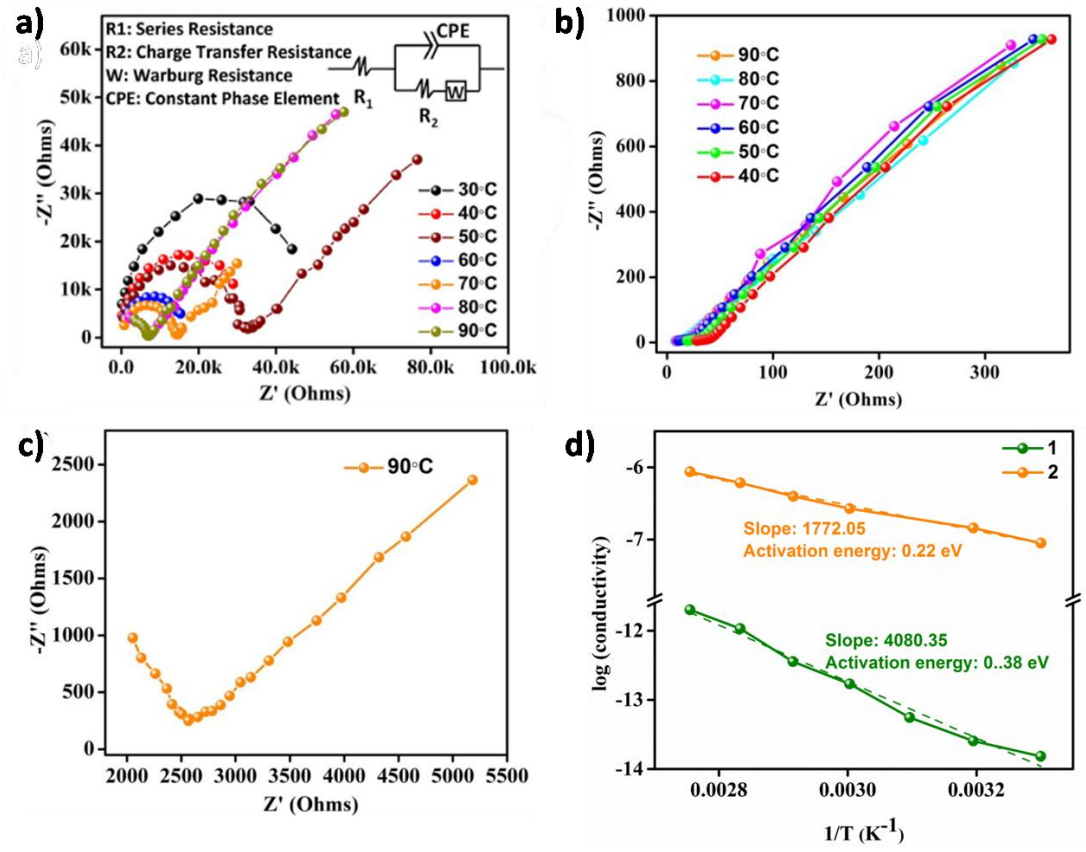

Figure 2.5. Nyquist plots for (a) **1**, (b) **2**, and (c) **3** showing the variation of resistance with the temperature at 90% relative humidity. (The equivalent circuit is shown as an inset for **1**, and for others can be found in the appendix.) (d) Logarithmic plot of conductivity vs. temperature.

The pyridinols being coordinating in nature position the protonated pyridyl ends in a structured manner which provides a gas-tight percolating pathway for the protons to travel. More importantly, these solids are dense and have a negligible porosity which in turn means that they don't favor the fuel crossover (Figure 2.A.1). To assess the capability of these samples to work as solid electrolytes, we measured the alternating-current (ac) impedance spectra for the pelletized samples. The measurements were done from 30˚C to 90˚C at 90% relative humidity.

The conductivities for the three MOFs were calculated by fitting the impedance spectra to a proposed equivalent circuit (Figures 2.5 a and 2.A.2).

On comparing the conductivity values, it turned out that **2** made up of the Cd metal centers exhibited highest proton conductivity, i.e.,10^{-3} S/cm at 90˚C and 90% RH among the three. **1** showed a conductivity of 10^{-6} S/cm at 90˚C, 90% RH and **3** had a conductivity value of the order of 10^{-5} S/cm at 90˚C and 90% RH (figures 2.5 and table 2.1). The activation energies were calculated using the Arrhenius equation and were found to be 0.38 and 0.22 eV for **1** and **2** respectively. The low activation energies in these cases suggest the Grotthuss/hopping type of conduction. **3** didn't show any interesting conductivity value; therefore, its conductivity wasn't studied as a function of temperature. More importantly, pyridnol being a relatively mild acid (pKa, = 3.2) provides conductivities which are quite comparable to the ones reported in some of the sulfonic[20] and phosphonic[25] acid (pKa ~0.6 to 2.4) based proton conducting MOFs. Researchers have suggested higher concentration and acidities of the protic moieties as a prerequisite to guarantee efficient proton conduction and transport[33,34]. Polyprotic phosphonic acids and sulfonic acids have been decorated into the MOFs for attaining significant conductivities[20,25,26]. When compared, we have much lesser density/concentration of protons, yet comparable proton conduction is observed under humid conditions.

Table 2.1. Table showing conductivity and activation energies for the three MOFs.

MOF	Conductivity @ 90˚C, 90% RH (S/cm)	Activation energy (eV)
1	8.30 x10^{-06}	0.38
2	2.33 x10^{-03}	0.22
3	4.04 x10^{-05}	N/A

Note: The low activation energies in all cases suggest Grotthuss type conduction. Activation energies are calculated using $\sigma = (\sigma_0/T) \exp(-Ea/ [R \text{ or } (KB).T])$.

The difference in conductivity of 1, 2 and 3

The marked dissimilarity in the humidity-dependent conductivities is intriguing despite **1** and **2** being isostructural frameworks. Such differences can be anticipated to originate from the

number of water molecules that these frameworks can accommodate within them[35]. To understand this, we have carried out water vapor sorption experiment on both the phases (Figure 2.6 a). As can be seen, **2** shows ~8 times higher water uptake when compared to **1**. Analyzing the crystal structure of the two MOFs more carefully, we observe that in both **1** and **2** the metal centers have octahedral coordination. While for Mg this represents saturated coordination, Cd can take up to seven coordinations, presenting an extra site for the water to coordinate under the humid conditions that are employed during the conductivity measurements. It is very well known that the coordinated water act as an excellent amphoteric center to form hydrogen bonds as well as to transfer proton across the channels. Also, when samples were analyzed under the TGA after the sorption experiment (Note: a large number of the water molecules are removed during the desorption cycle), weight loss resulting from water loss for both **1** and **2** could be observed, which were absent in the as-synthesized phases (Figure 2.6 b).

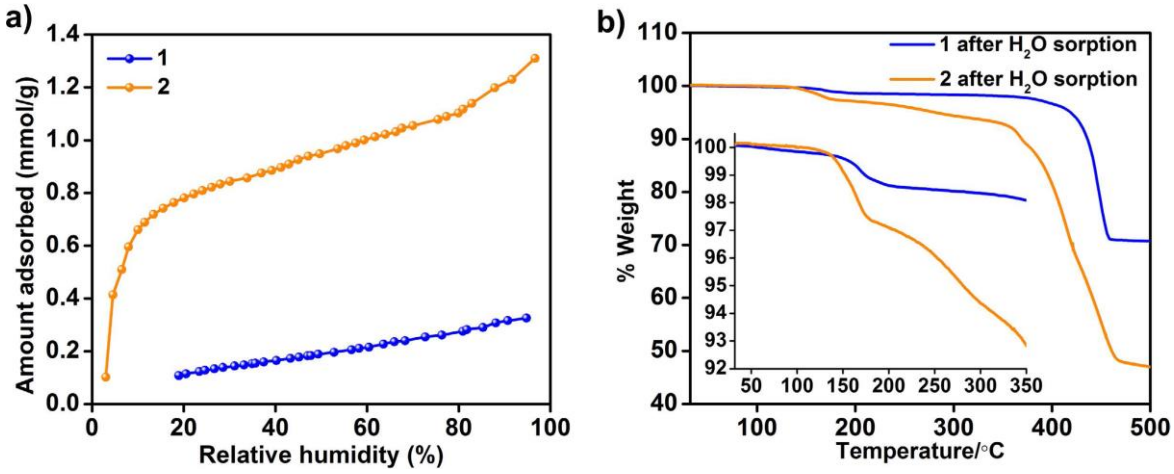

Figure 2.6. (a) Water- sorption isotherms of **1** and **2** at RT. (b) TGA plots of the post sorption samples of **1** and **2** depicting the water loss (120˚C–280°C). Inset: Zoomed-in image showing the weight losses from the water.

When the TGA profiles of the hydrated forms of the two MOFs are compared, weight loss due to water in the temperature range of 120˚ to 200˚C for **1** is observed. However, **2** has a two-step weight loss in the range of 130˚C to 280˚C. The water loss at a higher temperature in **2** is likely to be related to the tightly bound water, and some of them could also be coordinated to the Cd site. Most importantly, **2** seems to incorporate the notably larger amount of water when compared to **1** (2% for **1** vs. 8% for **2**, inset Figure 2.6 b). Nd in **3** also can host more coordinated

water molecules and could account for the higher proton conductivity than **1**. Also, the pores in **3** are significantly larger, but the relatively less difference in the conduction values between **1** and **3** suggests that this effect doesn't contribute much to the overall proton conductivity compared to the differences in the acidity of pyridinol arising from the hardness/softness of the metal centers.

2.3.4. Post-impedance stability of the MOFs

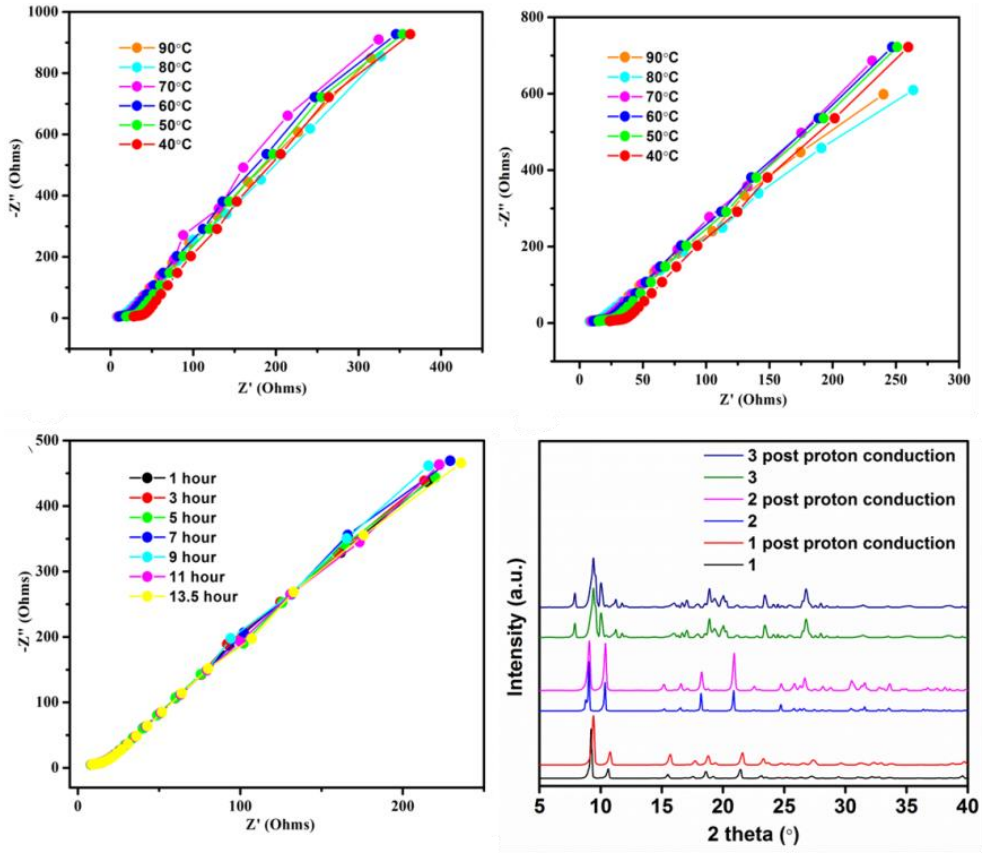

Figure. 2.7. Stability studies: Variable Temperature Impedance Spectra for (a) **2** at 90% RH (heating), (b) 2 at 90% RH (cooling) (c) Impedance spectra for **2** at different equilibration time at 90˚C, 90% RH. (d) PXRD comparisons for the three MOFs before and after proton conduction.

Any possible guest leaching for **2** under the operational conditions was verified by measuring the conductivity values for both heating and cooling cycles. The conductivities indicated no change when both the cycles were compared (Figure 2.7). Further characterizations were carried out on the post-impedance measurement samples using PXRD, CHN and Field Emission SEM to confirm the same (Figures 2.7 d, 2.A.5, and Table 2.A.1). PXRD patterns proved that the MOFs didn't decompose under the measurement conditions. Even the recently

reported sodium and cesium sulfonate and magnesium phosphonate MOFs do not show any such decomposition under similar conditions[20,28,36].

2.4. Conclusions

In conclusion, this study is a proof-of-concept, showing how anchoring a zwitterionic, relatively mild acidic guest into the MOF frameworks can prove to be an effective strategy to achieve stoichiometric loading of the guest. This approach is an efficient route to minimize the guest leaching, which in turn increases the life of the electrolyte material and is key to obtaining steady proton conduction. In the presence of water, i.e., under humid conditions, pyridinol forms hydrogen-bond mediated conduction pathway and exhibits moderate proton conductivity values. Being a mild acid, it provides conductivity values quite comparable to the reported MOFs having highly acidic guests. The activation energies are all very low signifying that the conduction happens via the Grotthus mechanism. This strategy has the scope of being readily extended across some other metal organic systems. However, the proton conductivity values are not high (target value: 10^{-2} S/cm), so the next chapter deals with enhancing the conductivities using post-synthetic modification.

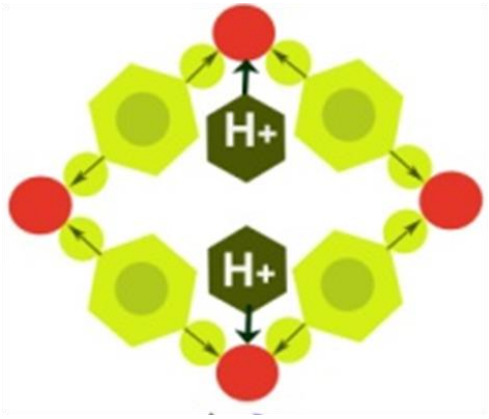

MOF	Conductivity @ 90°C/90% RH (S/cm)	Activation energy (eV)
1_Mg	8.30×10^{-06}	0.38
2_Cd	2.33×10^{-03}	0.22
3_Nd	4.04×10^{-05}	N/A

2.5. References:

1. Kirubakaran, A.; Jain, S.; Nema, R. K. Renew. *Sust. Energ. Rev.* **2009**, *13*, 2430.
2. Jourdani, M.; Mounir H.; Marjani, A. E. *The Open Fuels & Energy Science Journal*, **2017**, *10*, 96.
3. Zhu, L.; Liu, X.; Jiang, H.; Sun, L. *Chem. Rev*. **2017,** *117*, 8129.
4. Li, H.; Wang, K.; Sun, Y.; Lollar, C. T.; Li, J.; Zhou, H. *Mater. Today*. **2018**, *21*, 108.
5. Lustig, W. P.; Mukherjee, S.; Rudd N. D.; Desai, A. V.; Li. J.; Ghosh, S. K. *Chem. Soc. Rev*. **2017**, *46*, 3242.
6. Lin, R.; Liu, S.; Ye, J.; Li, X.; Zhang, J. *Adv. Sci.*, **2016**, *3*, 1500434.
7. Shao, M.; Chang, Q.; Dodelet, J.-P.; Chenitz, R. *Chem. Rev*. **2016**, *116*, 3594.
8. Zhou, J.; Qi, P.; Wang, B. *Coord. Chem. Rev*. **2016**, *307*, 361.
9. Ramaswamy, P., Wong, N. E. & Shimizu, G. K. H. *Chem. Soc. Rev*. **2014**, *43*, 5913.
10. Yoon, M., Suh, K., Natarajan, S. & Kim, K. *Angew. Chem. Int. Ed*. **2013**, *52*, 2688.
11. Yamada, T., Otsubo, K., Makiura, R. & Kitagawa, H. *Chem. Soc. Rev*. **2013**, *42*, 6655.
12. Meng, X.; Wang, H.; Song, S.; Zhang H. *Chem. Soc. Rev*. **2017**, *46*, 464.
13. Sadakiyo, M.; Ōkawa, H.; Shigematsu, A.; Ohba, M.; Yamada, T.; Kitagawa, H. *J. Am. Chem. Soc*. **2012**, *134*, 5472.
14. Sadakiyo, M., Yamada, T.; Kitagawa, H. *J. Am. Chem. Soc*. **2009**, *131*, 9906.
15. Zhou, Z., Li, S., Zhang, Y., Liu, M. & Li, W. *J. Am. Chem. Soc*. **2005**, *127*, 10824.
16. Chen, Y.; Thorn, M.; Christensen, S.; Versek, C.; Poe, A.; Hayward, R. C.; Tuominen M. T.; Thayumanavan. S. *Nat. Chem*. **2010**, *2*, 503.
17. Nandi, S.; Dhavale, V. M.; Shalini, S.; Werner-Zwanziger, U.; Singh, H.; Kurungot, S.; Vaidhyanathan, R. *Adv. Mater. Interfaces*. **2015**, 1500301, (doi: 10.1002/admi.201500301.
18. Kreuer, K. D. *Chem. Mater*. **2014**, *26*, 361.
19. Gao, H.; Lian, K. *RSC Adv*. **2014**, *4*, 33091.
20. Hurd, J. A.; Vaidhyanathan, R.; Thangadurai, V.; Ratcliffe, C. I.; Moudrakovski, I. L.; Shimizu. G. K. H. *Nat. Chem*. **2009**, *1*, 705.
21. Bureekaew, S.; Horike, S.; Higuchi, M.; Mizuno, M.; Kawamura, T.; Tanaka, D.; Yanai, N.; Kitagawa. S. *Nat. Mater*. **2009**, *8*, 831.
22. Shimizu, G. K. H., Taylor, J. M.; Kim, S. *Science*. **2013**, *341*, 354.

23. Sadakiyo, M., Yamada, T., Honda, K., Matsui, H.; Kitagawa, H. *J. Am. Chem. Soc*. **2014**, *136*, 7701.
24. Sahoo, S. C., Kundu, T.; Banerjee, R. *J. Am. Chem. Soc*. **2011**, *133*, 17950.
25. Taylor, J. M.; Mah, R. K.; Moudrakovski, I. L.; Ratcliffe, C. I.; Vaidhyanathan, R.; Shimizu, G. K. H. *J. Am. Chem. Soc*. **2010**, *132*, 14055.
26. Phang, W. J.; Jo, H.; Lee, W. R.; Song, J. H.; Yoo, K.; Kim, B.; Hong, C. S. *Angew. Chem. Int. Ed*. **2015**, *54*, 5142.
27. Ponomareva, V. G.; Kovalenko, K. A.; Chupakhin, A. P.; Dybtsev, D. N.; Shutova, E. S.; Fedin, V. P. *J. Am. Chem. Soc*. **2012**, *134*, 15640.
28. Ramaswamy, P., Wong, N. E., Gelfand, B. S.; Shimizu, G. K. H. *J. Am. Chem. Soc*. **2015**, *137*, 7640.
29. Ponomareva, V. G., Kovalenko, K. A., Chupakhin, A. P., Shutova, E. S.; Fedin, V. P. *Solid State Ionics*, **2012**, *225*, 420.
30. Horike, S.; Chen, W.; Itakura, T.; Inukai, M.; Umeyama, D.; Asakurae, H.; Kitagawa, S. *Chem. Commun*. **2014**, *50*, 10241.
31. Zhai, Q. G.; Mao, C.; Zhao, X.; Lin, Q.; Bu, F.; Chen, X.; Bu, X.; Feng, P. *Angew. Chem. Int. Ed*. **2015**, *54*, 7886.
32. Tu, T. N.; Phan, N. Q.; Vu, T. T.; Nguyen, H. L.; Cordova, K. E.; Furukawa, H. *J. Mater. Chem. A*. **2016**, *4*, 3638.
33. Kreuer, K.-D.; Wohlfarth, A. *Angew. Chem. Int. Ed.* **2012**, *51*, 10454.
34. Vuilleumier, R.; Borgis, D. *Nat. Chem*. **2012**, *4*, 432.
35. Taylor, J. M.; Komatsu, T.; Dekura, S.; Otsubo, K.; Takata, M.; Kitagawa. H. *J. Am. Chem. Soc*. **2015**, *137*, 11498.
36. Wong, N., Hurd, J. A., Vaidhyanathan, R.; Shimizu, G. K. H. *Can. J. Chem*. **2015**, *93*, 988.

2.A. Appendix

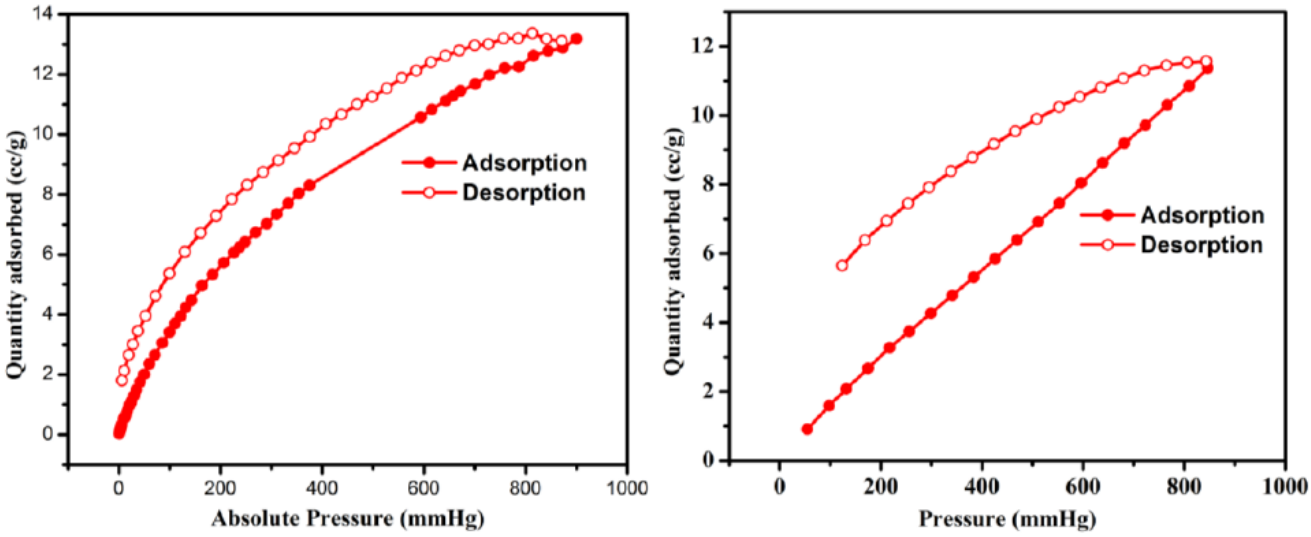

Figure 2.A.1. CO_2 Adsorption isotherm for **1** (left) and **2** (right) at 273 K.

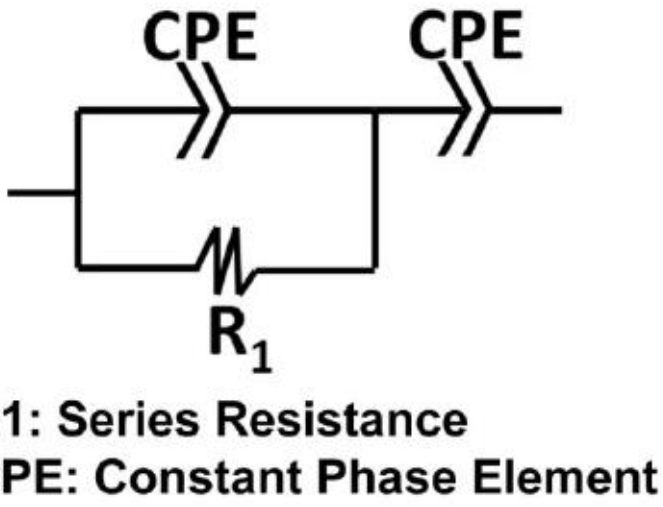

Figure 2.A.2. The equivalent circuit used to calculate resistance from the impedance plots for **2**, and **3**.

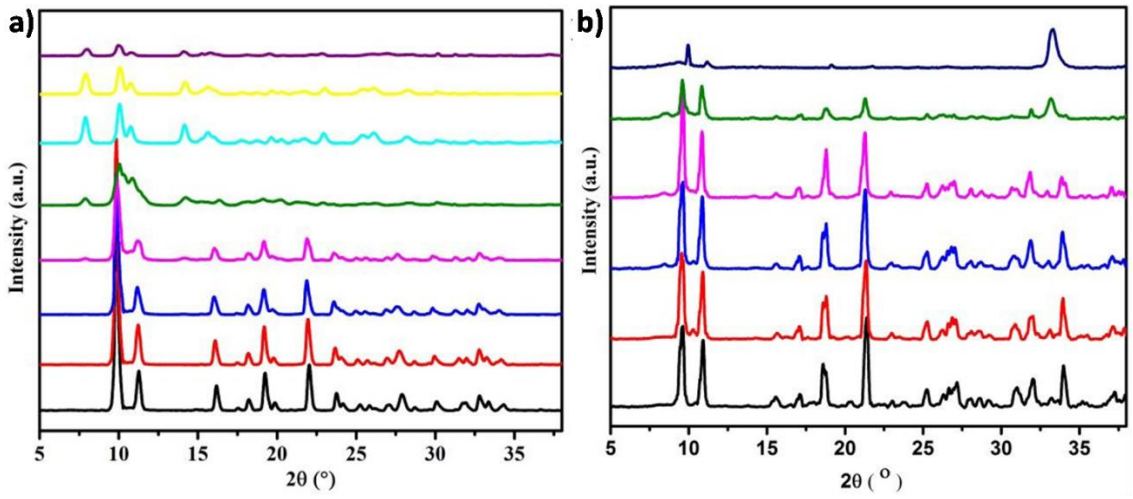

Figure 2.A.3. Variable temperature PXRD for (a) **1** and (Note that phase starts to change at ~450˚C and a completely new phase is obtained at ~550˚C. This phase change is irreversible, and the phase has been indexed (Figure 2.A.4). Black: 30˚C, Red: 200˚C, Blue: 380˚C, Pink: 400˚C, Olive: 450˚C, Cyan: 550˚C, Yellow: 600˚C, Purple: 30˚C.) (b) **2**. (Black: 30˚C, Red: 150˚C, Blue: 250˚C, Pink: 350˚C, Olive: 400˚C, Purple: 450˚C).

Discussion on the results from VT-PXRD experiments of 1:

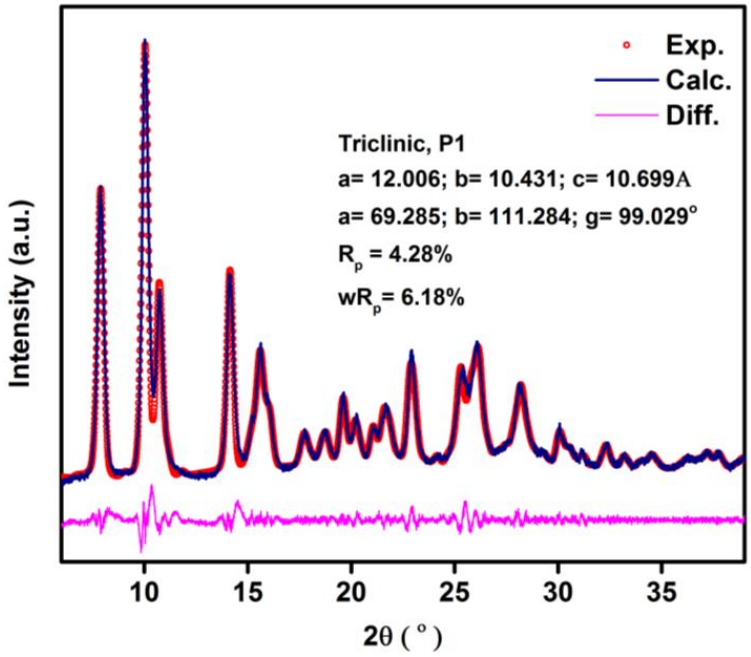

Figure 2.A.4. Pawley refinement of the new beta phase formed by the transformation of the **1** at 550˚C.

.

In **1**, the pyridinol is lost at ~450˚C which results in Mg metal having a highly unfavorable four-coordinated geometry inducing a severe structural strain. The structure, therefore, is expected to rearrange. Accordingly, with the loss of pyridinol at 450˚C, a phase change is triggered, and by 550˚C a beta-phase is crystallized. This conveys that the Mg-terephthalate exists as a crystalline phase even upon the removal of the pyridinol as the framework is neutral. This beta phase has been indexed and a Pawley fit (Accelrys) has been carried out using material studio which resulted in a triclinic cell for this phase (a= 12.006 Å; b= 10.431 Å; c= 10.699 Å, α= 69.285˚; β= 111.284˚; γ= 99.029˚), which corresponds to a new Mg terephthalate phase.

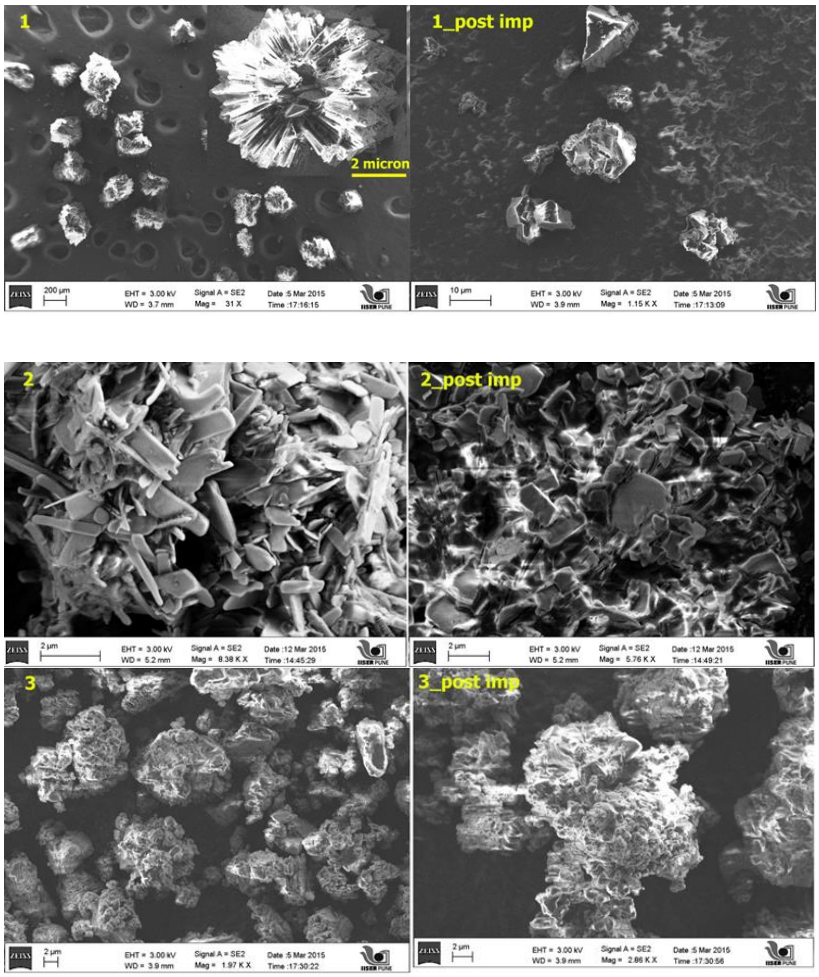

Figure 2.A.5. FE-SEM images of as-made and post-impedance samples of **1**, **2** and **3** showing the polycrystalline morphologies being intact.

Table 2.A.1. CHN values for the three MOFs before and after proton conduction.

Sample	%N	%C	%H
1 before proton conduction	4.82	54.80	3.076
1 after proton conduction	4.89	54.85	2.961
2 before proton conduction	3.73	42.65	2.311
2 after proton conduction	3.76	41.97	2.437
3 before proton conduction	3.99	42.18	2.144
3 after proton conduction	3.77	42.39	2.104

Table 2.A.2. Calculation of Activation Energy for **1** @ 90% RH.

T (˚C)	R (Ω)	Thickness (cm)	A (cm^2)	κ(S/cm)	1/T (K^{-1})	Log (κ)	R(Gas constant)	Slope	Ea (kJ/mol)
30	44185	0.0585	1.326	9.98E-07	0.0033	-3.8175			
40	35356	0.0585	1.326	1.25E-06	0.0031	-13.594			
50	25231	0.0585	1.326	1.75E-06	0.0030	-13.257			
60	15511	0.0585	1.326	2.84E-06	0.0030	-12.770	8.314	4080	33.9044
70	11232	0.0585	1.326	3.93E-06	0.0029	-12.447			
80	6973	0.0585	1.326	6.32E-06	0.0028	-11.971			
90	5310	0.0585	1.326	8.30E-06	0.0027	-11.698			

Table 2.A.3. Calculation of Activation Energy for **2** @ 90% RH.

T (˚C)	R (Ω)	Thickness (cm)	A (cm^2)	κ(S/cm)	1/T (K^{-1})	Log (κ)	R(Gas constant)	Slope	Ea (kJ/mol)
40	56.58	0.065	1.326	8.66E-04	0.0033	-7.0516			
50	45.85	0.065	1.326	1.07E-03	0.0031	-6.8414			
60	35.02	0.065	1.326	1.40E-03	0.0030	-6.5719			

70	29.52	0.065	1.326	1.66E-03	0.0029	-6.4010	8.314	1772	14.7324
80	24.52	0.065	1.326	2.00E-03	0.0028	-6.2155			
90	21.02	0.065	1.326	2.33E-03	0.0027	-6.0614			

Chapter 3

Enhancing Proton Conductivity of MOFs Through Post-synthetic Modifications

2018

Content of this chapter is published in the following articles:

1. *Scientific Reports*. **2016**, *6*, Article number: 32489 https://www.nature.com/articles/srep32489

Reproduced by permission from Nature Publishing Group

2. *Eur. J. Inorg. Chem*. **2016**, *27*, 4382 https://onlinelibrary.wiley.com/doi/abs/10.1002/ejic.201600364

Reproduced by permission from Wiley

3.1. Introduction

Metal Organic frameworks (MOFs) serve as exceptional platforms for modular tuning owing to their crystalline nature and the insights available from their single crystal structures. Accordingly, many studies have been reported wherein replacement of the organic struts, the metal, or the extra-framework species has resulted in enhancement in the properties of MOFs tuned for specific applications[1-9]. Various strategies have been employed to undertake such modular replacements. Post-synthetic modification seems to be an effective approach towards realizing the same[10,11]. Typically, it has been used to introduce functional moieties to enhance properties like chirality, photoactivity, gas selectivity, and biomedical applications[11-13]. Recently, MOFs are being studied very extensively for their use as solid electrolytes or proton-conducting membranes for fuel-cell applications[1-5]. Post-synthetic modification has predominantly been used to boost the proton conductivity values in MOFs by impregnating salts[14,15], ions[16], guest,[17] acid[18-21], guests, defect control[22], and isomorphous ligand replacement[10].

To achieve high proton conductivities in MOFs, one of the key requirements is a large number of hydrogen-bonding species percolating throughout the channels[1-5,22-25]. It has been well established that three-dimensionally extended hydrogen-bonded networks afford most favorable pathways for the transfer of proton through a Grotthuss mechanism[26]. Subsequently, a vast amount of research intended at identifying the species that can be incorporated into the MOFs to enhance their proton conductivity is foregoing.

Loading a protic guest into porous materials via post-synthetic approach is a tricky process[11] as it might lead to the collapse of the framework. As already has been described in section 2.1, the protic guest can either be made a part of the framework or can be incorporated into the pores of the MOF (Figure 2.1). It is not very easy to predict the enhancement in the conduction brought by the incorporation of a flexible hydrogen bonding guest into the framework of the MOF but it brings in additional advantage of avoiding the possibility of leaching of the guest from the MOF. To the best of our knowledge, only one report shows post-synthetic anchoring of proton bearing species (histidine) in a MOF. It exhibited conductivities of 10^{-9} S/cm at 146˚C, but the conductivity under humid conditions was not reported[20]. Loading the guest into the frameworks as an extra-framework species is also a tricky process. An optimum loading needs to be achieved as too low a loading might not be favorable for conduction whereas

the higher loadings can block the channels and limit their diffusion. This leaves the challenge open to discover systems where smaller/optimum amounts of doping ions or molecules show large improvements in the conduction. Here we show an enhancement in proton conductivity for the MOFs described in chapter 2, using both approaches, by judicious choice of the conducting components.

In first approach we use the MOFs **1** and **3**, to introduce a more flexible, protic, stronger hydrogen bonding, neutral guest (ethylene glycol; EG) which can coordinate to the metal center and has a high boiling point. Using this strategy the proton conduction has been enhanced by 1000 folds (10^{-6} to 10^{-3} S/cm) for the resulting MOF and a very low activation energy (0.11 eV) has been achieved. ^{13}C-SSNMR coupled with atomic modeling provides insights regarding the probable proton-conduction pathway functionalized with proton transporting EG moieties. For the second approach, we introduce ~10 % Cs ions into the Mg-terephthalate-pyridinol MOF (**1**), to enhance the proton conductivity of the MOF by 10,000-fold. Remarkably, the Cs loading does not cause any noticeable distortion to the framework. The activation energy is brought down to half of the initial value (from 0.35 eV for **1** to 0.19 eV for **1_Cs**) for the conduction process by the Cs introduction. The high extent of hydration of the Cs^+, which is anticipated to offer more hydrogen bonds and thus an efficient pathway for the proton transfer, is what leads to low activation energy and high conductivity.

For easy understanding, these two approaches will be discussed in the following, separate chapters (3I and 3II).

Chapter 3I

1000-fold Enhancement in Proton Conductivity of a MOF Using Post-synthetically Anchored Proton Transporters

2018

3I.1. Materials and Methods:

All the organic chemicals were purchased from Sigma Aldrich. The metal salts were procured from Alfa Aesar. All reagents and solvents were used without any further purification.

3I.1.1 Synthesis procedure

Milligram scale synthesis:

1_EG was prepared by stirring 0.3 g of **1** (see synthesis of **1** in section 2.2.1) in 5 ml EG at 120˚C for 12 hours. Following this, it was filtered and washed with copious amount of methanol and acetone to remove the excess EG present.

(Elemental analysis, observed/calculated: C – 52.58%/53.45%; H - 3.84%/3.38%; N – 3.77%/3.8%). The air-dried sample gave a yield of ~ 90% (based on Mg).

1_C was synthesized hydrothermally using the approximate molar ratios of $Mg(NO_3)_2.6H_2O$, terephthalic acid and 4-hydroxypyridine as 1:1. 0.1g Magnesium nitrate and 0.065 g terephthalic acid were stirred in 5 ml ethylene glycol for 15 minutes at RT. The contents were then sealed in an autoclave and heated at 140˚C for 48 hours. It was slowly cooled down to room temperature. A product containing thin platy crystals was collected by filtration using methanol and acetone.

The air-dried sample gave a yield of ~ 70% (based on Mg).

3_EG was prepared by heating **3** (see synthesis of **3** in section 2.2.1) at 100˚C for 2 hours and then stirring it in EG for 12 hours at 120˚C.

(Elemental analysis, observed/calculated: C – 41.82%/42.02%; H - 2.191%/2.35%; N – 2.69%/2.72%). The air-dried sample gave a yield of ~ 87% (based on Nd).

The bulk products were phase pure as confirmed by powder X-Ray diffraction experiment (Figure 3I.1).

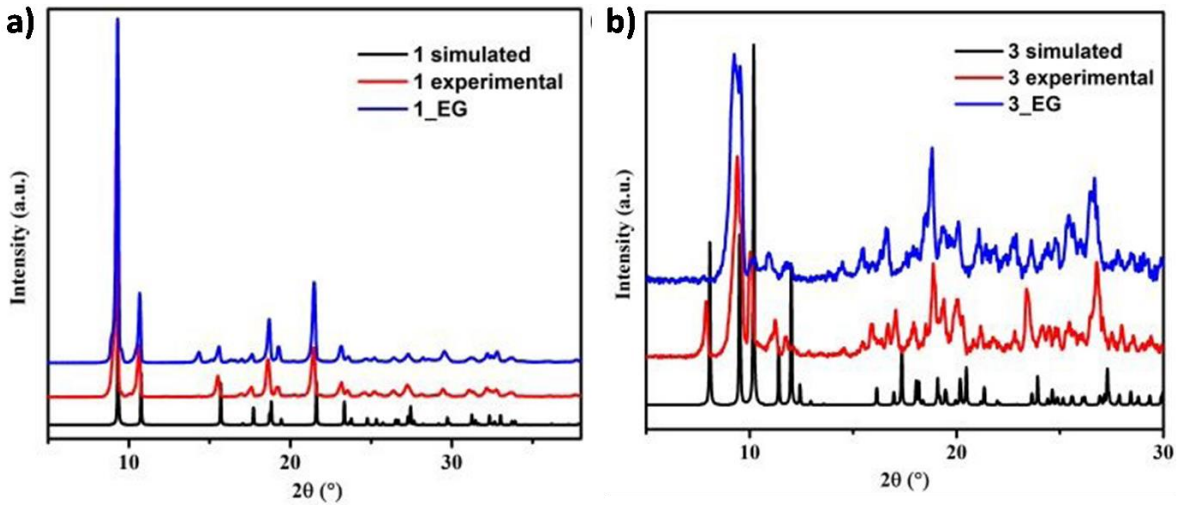

Figure 3I.1. PXRD comparison for (a) **1** and **1_EG** and (b) **3** and **3_EG**.

3I.1.2. Characterization and analytical methods:

Solid-state NMR spectroscopy:

Solid-state NMR was recorded using an 800 MHz Bruker NMR instrument.

Structure Simulation studies:

Structural simulations were done using Materials Studio (Accelrys) software.

3I.2. The motivation for the work

The conductivity values for **1**, **2** and, **3** as described in chapter 2 were not very high. On having a closer look at their structures, we observe that the spatial separation of the protonated pyridinol units (3.82 Å in **1**, 3.97 Å in **2,** and 5.52 Å in **3**, Fig. 2.2, 2.3) is rather large. Lacing a more flexible and stronger hydrogen-bonding guest down the conduction path decorated by the pyridinols could aid in transferring these far-spaced protons. To achieve this, we need a protic guest with optimal hardness capable of coordinating to the metal centers in the MOFs, it should bind preferably over pyridinol and should have adequate flexibility to help proton shuttling via increased hydrogen bonds. Also, it needs to be neutral in order to replace the zwitterionic pyridinols. Ethylene Glycol (EG) fulfills all of these requirements. **1**, $Mg_4(Tp)_4(PyOH)_4$, was stirred in EG at 120˚C for loading ethylene glycol. By this procedure, we could successfully

replace 1/4th of the pyridinol (confirmed via TGA as shown in figure 3I.2 and ^{13}C-MAS NMR) by EG forming $Mg_4(Tp)_4(PyOH)_3(EG)$. Using this approach, we expected high conductivity for **2** considering it has inherently high conductivity, but all the attempts to load EG in the framework resulted in the collapse of the framework as the structure is not stable to the pyridinol loss (Figure 2.4). **3**, on the other hand, is stable to the loss of pyridinol. In addition to the stability, the presence of replaceable coordinated DMF molecules provides an extra site for EG binding. **3** was heated at 100˚C under vacuum to remove DMF, and while maintaining it under vacuum, EG was syringed in. The sample was then allowed to stand for 12 hrs at 120˚C. EG treated samples were meticulously washed with a plentiful amount of solvents.

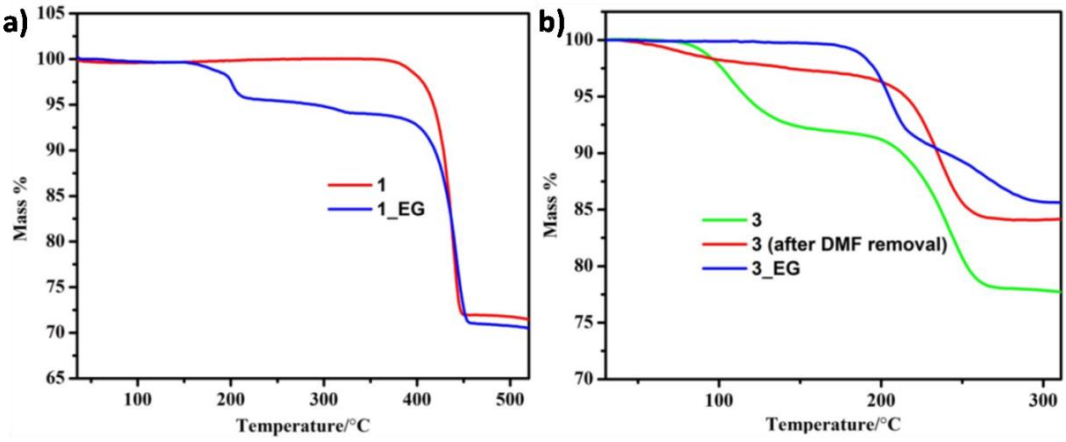

Figure 3I.2. (a) TGA comparison of **1** and **1_EG**. Weight loss corresponding to loss of μ-2 bridging pyridinol happens in the temperature range of 320 to 450˚C. (b) TGA comparison for **3**, **3** after DMF removal, and **3_EG**.

3I.3. Results and discussion

3I.3.1. Solid State ^{13}C-NMR studies

Solid State NMR (SSNMR) has been successfully used to understand the role of functional species in various proton conducting MOFs[27,28]. We carried out NMR spectroscopy on **1_EG** and **3_EG** to confirm the coordination modes of ethylene glycol in the two. Interestingly, we observed a terminal coordination of EG to the metal centers (Mg and Nd) for both **1_EG** and

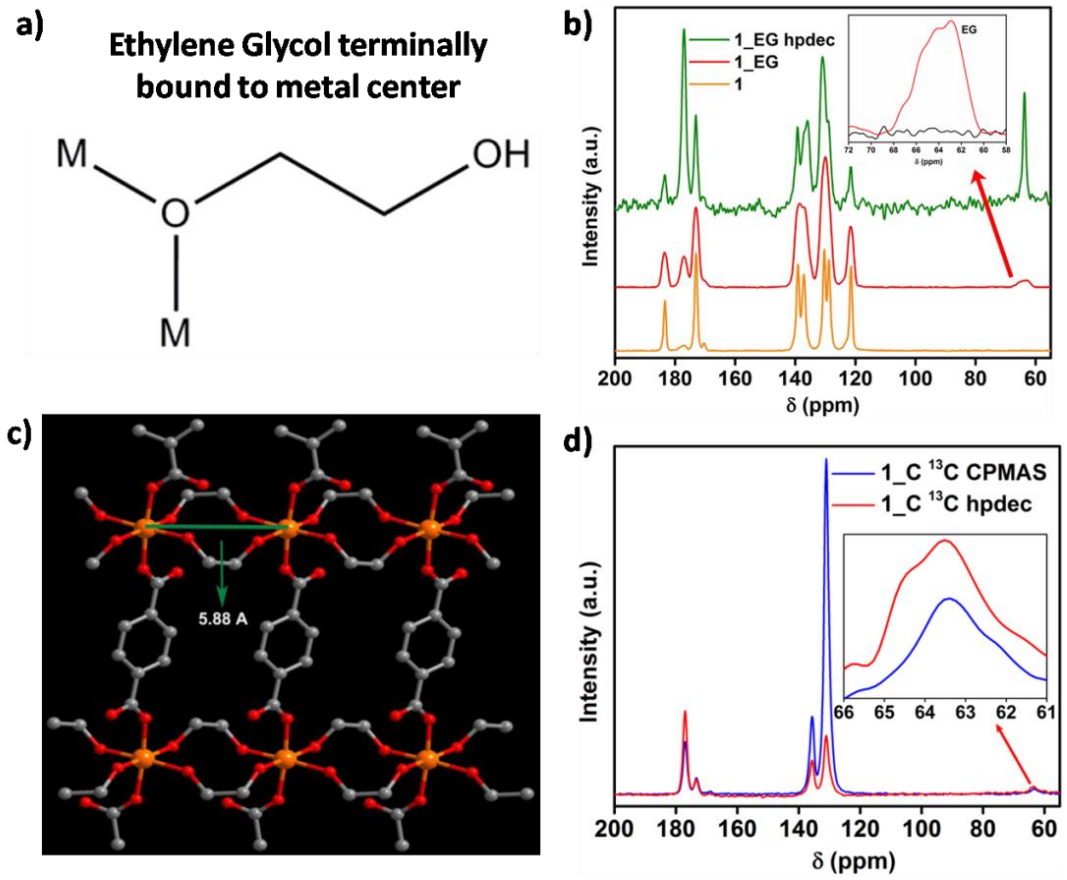

Figure. 3I.3. (a) Schematic representation of EG bound to the metal center. (b) Comparison of the ^{13}C-SSNMR of **1** and **1_EG**, showing the presence of terminal coordination mode for EG. (c) Model compound, i.e. a magnesium terephthalate ethylene glycol layer showing ethylene glycol bonded in a μ2-bridging fashion. The distance between the two magnesium centers required for accommodation of the ethylene glycol is ~5.9 Å whereas the available space in **1** is 3.6 Å. This compound has not been reported in the literature. Color code: Orange- Mg, red- O, Grey-C. Right: ^{13}C NMR for **1_C** showing the peak for EG appearing as a singlet, which suggests the presence of only one type of coordination mode for the EG molecules.

3_EG (Figures 3I.3, 3I.4). This leaves the other non-coordinated OH- groups hanging into the pore of the resulting MOFs. Further, for obtaining more insights into the mobility of the framework components, mainly the PyOH, and EG, the SSNMR spectra of **1**, **1_EG**, and a control (**1_C**) have been compared (Figure 3I.3 b). **1_C** is a Mg-terephthalate framework having ethylene glycol binding two different metal centers via both its oxygen in a μ-2 fashion and has

no pyridinol (Figure 3I.3 c). This represents EG in the most rigid form with all the carbons from such EG molecules being equivalent.

The ^{13}C CPMAS NMR of **1** (Figure 3I.3 a) shows well-resolved peaks for both terephthalate and pyridinol owing to its high crystallinity. Most importantly, multiple peaks for pyridinol are observed in the NMR. It seems like pyridinol is present in two forms, one where the proton resides on the pyridyl nitrogen (chemical shifts: 139, 137, 121 ppm) and other where most probably the -OH group bound to the metal center is protonated (chemical shift: 183, 173, 129 ppm). In the ^{13}C CPMAS NMR spectrum of **1_EG**, the main region of focus is the 55-75 ppm corresponding to the peaks from EG. A prominent peak is seen at 64 ppm, which appears to be a doublet indicating that EG is terminally bound to the metal center (Figure 3I.3 a). We also carried out a proton-decoupled ^{13}C Magic Angle Spinning (MAS) NMR for **1_EG** and observed that the relative intensity of the peak at 64 ppm is considerably higher when compared to the peak from the ^{13}C CPMAS NMR for the same (Figure 3I.3 b). This means that the mobility of ethylene glycol is comparatively higher than the other framework components.

Distinctly, the peak for EG in **1_C** is a singlet (Figure 3I.3 d), and the ^{13}C CPMAS NMR experiments suggest the lack of mobility related to the EG molecules. Also, if the EG had been loaded in the pore as an extra-framework guest, given the similar shape and size of the pores of **1** and **2** (Figure 2.2), EG should have been loaded in both the MOFs. However, just **1** shows loading, therefore, the most probable explanation is that EG is not loading just as an extra-framework guest, but takes up the coordination. Thus, it is concluded that there is a very high probability of a terminally bound EG in **1_EG** which are very mobile as observed from the comparison of the ^{13}C CPMAS NMR and ^{13}C MAS NMR spectra with high power decoupling (hpdec) spectrum.

In-depth study for **3_EG** could not be done because of difficulty in recording NMR as Nd is paramagnetic in nature. However, ^{13}C-SSNMR for **3_EG** shows the peak for EG as a doublet, implying that the EG binds to the Nd center via one of the OH groups in a monodentate fashion (Figure 3I. 4).

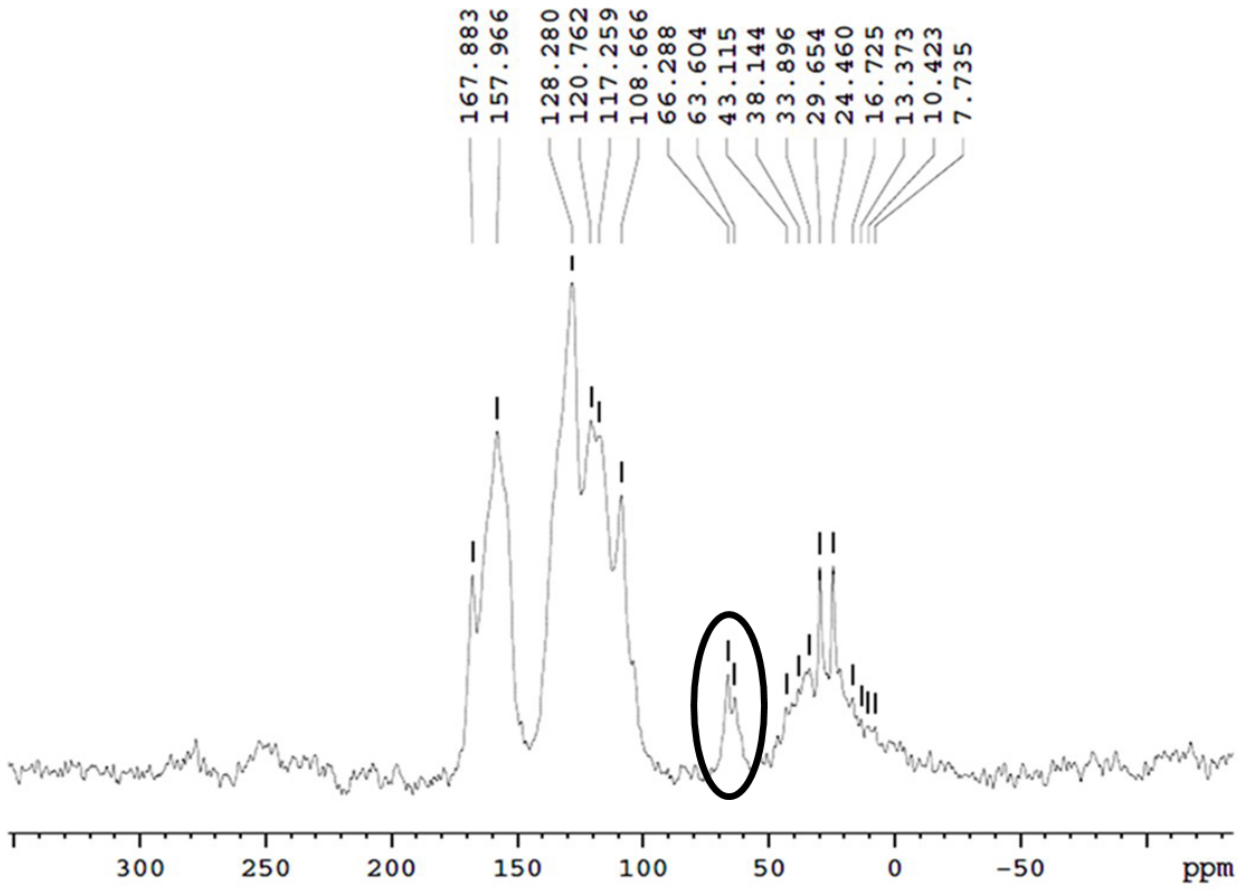

Figure 3I.4. ^{13}C-SSNMR for **3_EG**. Peaks corresponding to EG are circled.

3I.3.2. Structural simulation studies

Recently, atomic simulation has been employed very efficiently to solve and manipulate periodic structures, mainly, in framework solids such as COF and MOF[29-31]. In order to gain additional insights into the role of ethylene glycol in proton conduction, we carried out structural simulations using the Materials Studio V.6.0 (Accelrys) software. For **1**, we built a triclinic model where 1/4th of the pyridinol moieties were made to be replaced by EG molecules (consistent with TGA and SSNMR). One of the OH groups of the EG was made to coordinate the Mg center, and the other end was left dangling into the pore. The coordinated oxygen was made into μ-2 bridging oxygen. This configuration gets the EG sandwiched between the two pyridinol units along the c-axis (Figure 3I.5 a). Following this, a geometry optimization was performed using a tight binding DFT (DFT-TB) algorithm on this configuration. While doing the

geometry optimization, the unit cell was kept fixed. Running an energy optimization on this phase showed that it had a relative energy of ~50% lower than that of the parent phase.

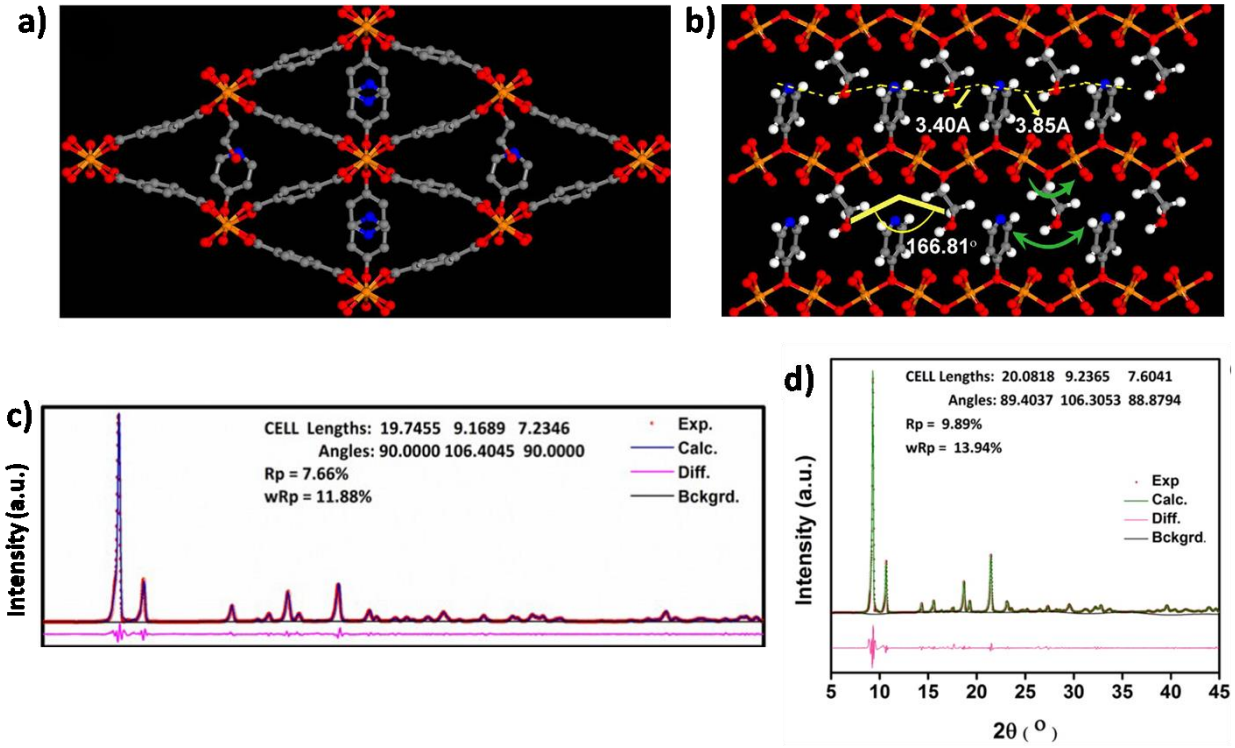

Figure 3I.5. (a) Simulated structure **1_EG**, showing the pendant EG and pyridinol lining the top and bottom of the 1-D channels (hydrogens have been omitted for clarity). (b) An a-axis view of **1_EG** showing the pendant EG and pyridinol lining the top and bottom of the 1-D channels (Dotted yellow lines: potential H-bond pathway; Green arrows: Rotational and pendulum-like motion that can be possible with the EG assisting proton transfer along this pathway). (c) Pawley refinement carried out on **1** and (d) **1_EG**.

This is also corroborated by the evident increase in the number of weak hydrogen bonds for the EG loaded configuration as determined by carrying out a PLATON analysis (section 3I.A.1). A probable hydrogen bond pathway lined with EG moieties and protonated pyridinols has been shown in Figure 3I.5 b. Ethylene glycol has the freedom to rotate and bend, and therefore, its pendant type arrangement could allow the EG to function like a pendulum to shuttle the protons across the pyridinol moieties. We believe the cooperativity between the pyridinol and EG will simultaneously increase the number of charge carrying species as well as bridge the

distance between the adjacent pyridinol units in the framework. For **3_EG**, a configuration was built wherein, the coordinated DMF molecules were made to be replaced by the EG. Like **1_EG,** the geometry was optimized for **3_EG** (Figure 3I.6 a). As expected, when the resulting configuration was compared with **3**, the **3_EG** had a lower relative energy and substantial number of hydrogen bonds.

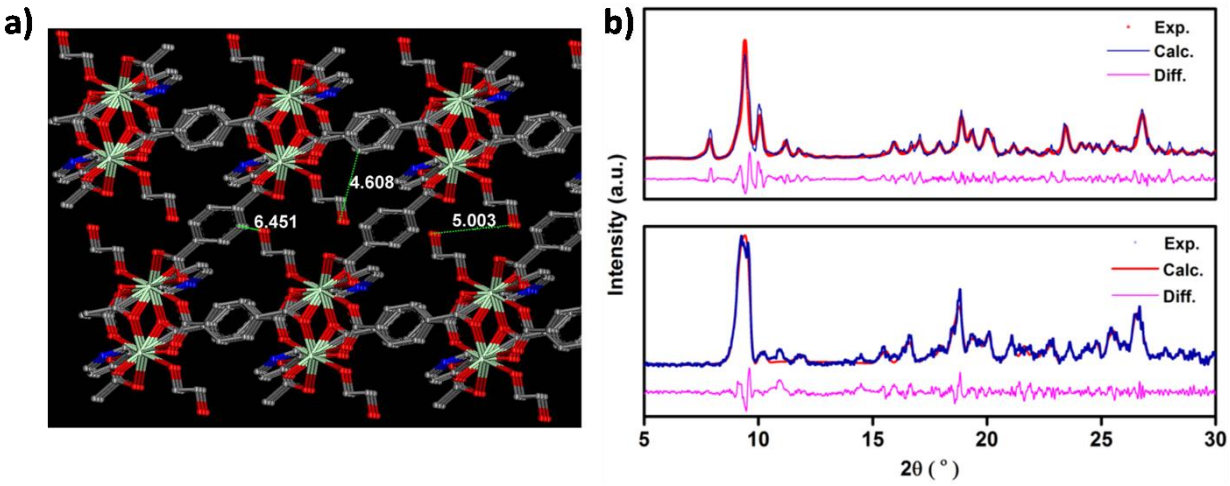

Figure. 3I.6. (a) Simulated structure of **3_EG**, with the DMF sites replaced by EG molecules and the energy/geometry was minimized using DFT routine. The optimized geometry shown above indicates the presence of larger spaces in this, wherein the EG resides and could have sufficient dynamic character to facilitate hydrogen bonds between protic pyridinols and can accommodate more water molecules under humid conditions. This could explain the higher conductivities of **3** over **1**. Color code: Sea-green- Nd; Red- O; Grey- C; Blue- N. (b) Pawley refinement carried out on **3** with a=10.400 Å, b= 10.340 Å, 11.292 Å, α- 99.132°, β- 90.645°, γ- 114.645°, Rwp- 15.29, Rp- 11.30% (top) and **3_EG**, a=10.764 Å, b= 10.605 Å, 11.183, α- 98.274°, β- 89.992°, γ- 113.834°, Rwp- 15.23%, Rp- 11.62% (bottom).

We could further substantiate these triclinic models of **1_EG** and **3_EG** by carrying out both Lebail and Pawley refinements. The F_{obs} could be extracted (Figures 3I.5 c, d, 3I.6 b, and 3I.7). The fits obtained for the experimental PXRD of the EG loaded phases reflected a good match with the proposed models.

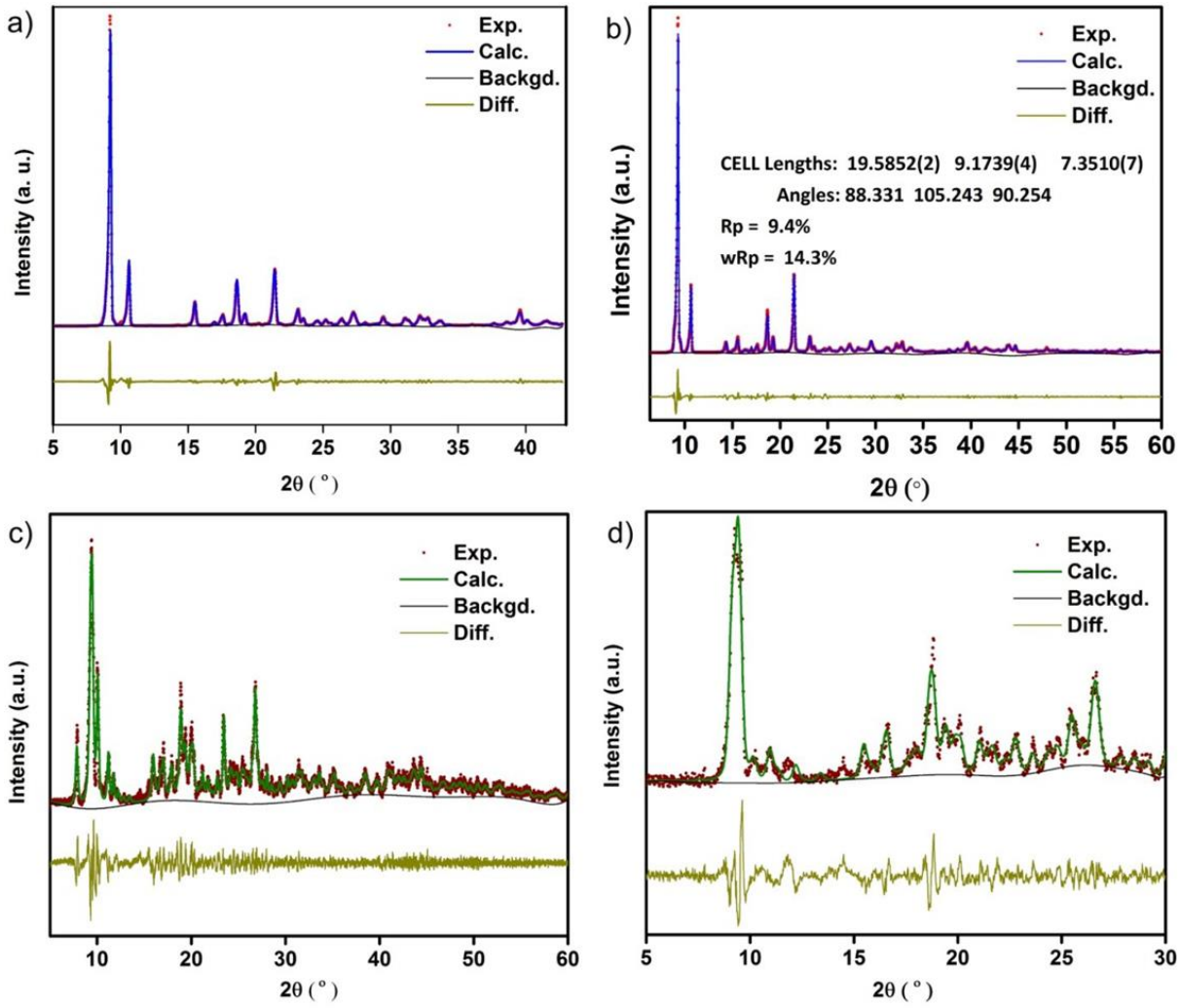

Figure 3I.7. Le Bail fit for a) **1**, a= 19.785(2) Å, b=9.196(5) Å, c=7.252(6) Å, α= 90.000˚, β=106.326(7)˚, γ=90.000˚, V= 1266.142(19) Å^3, wRp- 12.19%, Rp- 9.21%, χ^2- 8.18, D_{wd}- 0.12; b) **1_EG,** c) **3**, a= 10.322(2) Å, b=10.277(2) Å, c= 11.206(2) Å, α= 99.481(12)˚, β=90.489(11)˚, γ=114.909(11)˚, V= 1059.554(29) Å^3, wRp- 18.85%, Rp- 12.86%, χ^2- 1.92, D_{Wd}- 0.45 and d) **3_EG**, a= 10.277(5) Å, b=10.099(6) Å, c= 11.467(6) Å, α= 99.702(35)˚, β=91.683(49)˚, γ=113.336(49)˚, V= 1071.217(123) Å^3, wRp- 18.01%, Rp- 13.93%, χ^2- 1.98, D_{Wd}- 0.60. Note: Our attempts to carry out Reitveld refinements using these starting models have so far not yielded a satisfactory convergence.

3I.3.3. Proton conductivity studies

To assess the capability of these samples to work as solid electrolytes, we measured the alternating-current (ac) impedance spectra for the pelletized samples. The measurements were

done from 30˚C to 90˚C at 90% relative humidity. The conductivity values for the ethylene glycol loaded phases, **1_EG** and **3_EG** were calculated by fitting the impedance spectra of the samples to a proposed equivalent circuit (Figure 3I.8). **1_EG** and **3_EG** exhibited conductivities of 1.08×10^{-3} S/cm and 1.72×10^{-3} S/cm, respectively at 90˚C and 90% relative humidity. This represents 1000-fold (10^{-6} S/cm to 10^{-3} S/cm) and 100-fold (10^{-5} S/cm to 10^{-3} S/cm) enhancement in the proton conductivity values for **1_EG** and **3_EG**, respectively (Table 3I.1).

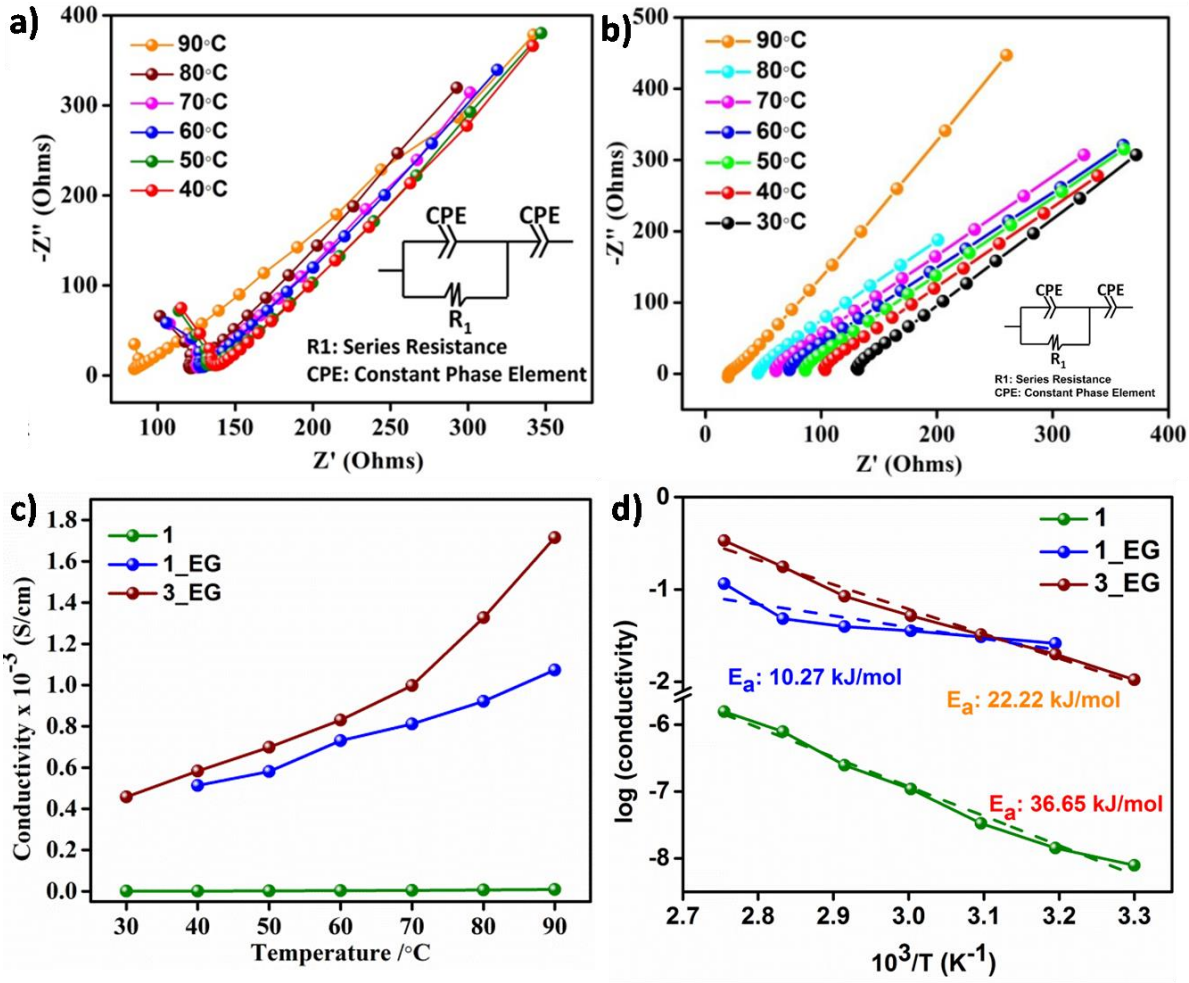

Figure 3I.8. Nyquist plots for (a) **1_EG** and (b) **3_EG** showing the variation of resistance with the temperature at 90%RH. (equivalent circuits are shown as insets for both the samples). (c) Conductivity vs. temperature plots showing the Arrhenius behavior in **1**, **1_EG** and **3_EG**. (d) Logarithmic plot of conductivity vs. temperature.

Enhancement of this extent is quite remarkable by using this simple and versatile design strategy. The already discussed cooperativity between the ethylene glycol and pyridinol is responsible for the increase in proton conductivity. It also seems to create a strongly knit, percolating conduction pathway that favors Grotthuss transport with an exceptionally low activation energy[26,33] (0.11 eV for **1_EG**). This, in fact, represents the minimal amount of energy required to break the hydrogen bonds implying that the EG/pyridinol combination provides nearly optimal strength of hydrogen bonds helping the transport of mildly acidic protons[26].

Table 3I.1: Conductivity and activation energy comparison for all the phases.

MOF	Conductivity @ 90°C/90% RH (S/cm)	Activation energy (eV)
1	8.30×10^{-06}	0.38
1_EG	1.08×10^{-03}	0.10
3	4.04×10^{-05}	N/A
3_EG	1.72×10^{-03}	0.21

3I.3.4. Post-impedance stability of the MOFs

Any possible guest leaching for the two phases under the operational conditions was verified by measuring the conductivity values for both heating and cooling cycles. The conductivities indicated no change when both the cycles were compared, (Figure 3I.9 a-d). Further characterizations were carried out on the post-impedance measurement samples using PXRD, CHN, TGA and Field Emission SEM to confirm the same (Figures 3I.9 e, f, 3I.A.1-4, and Table 3I.A.1). PXRD patterns proved that the MOFs didn't decompose under the measurement conditions. Also, if the partial decomposition of these glycol loaded phases resulted in the high conductivities in the glycol loaded phases, the same would be expected for the parent phases too. However, **1** and **3** clearly show considerably lower conductivities at 90˚C and 90% RH, strongly suggesting lack of any such decomposition.

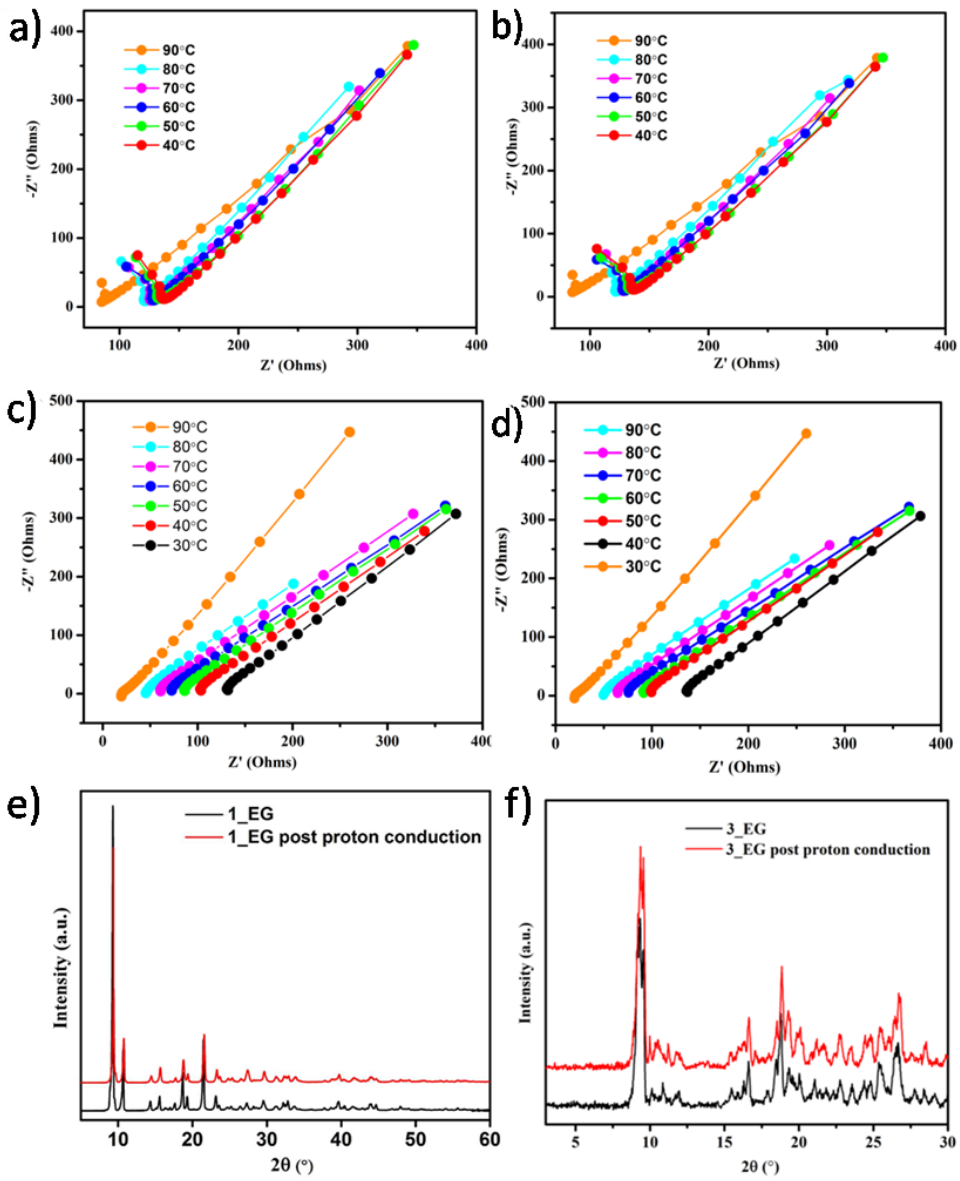

Figure 3I.9. Stability studies: Variable Temperature Impedance Spectra for (a) **1_EG** at 90% RH (heating), (b) **1_EG** at 90% RH (cooling) (c) **3_EG** at 90% RH (heating), (d) **3_EG** at 90% RH (cooling), (e) PXRD comparison for **1_EG** and (f) **3_EG** before and after proton conduction.

3I.4. Conclusions

In conclusion, this is a proof-of-concept, wherein incorporating flexible, coordinating hydrogen bonding guest (EG) into the MOF frameworks proves to be an effective strategy to attain stoichiometric guest loading and minimize the guest leaching. These are key to obtain

consistent proton conductivity values. Most importantly, this post-synthetic exchange of the coordinated pyridinols with EG provides a better hydrogen-bonded conduction pathway with significantly improved conductivities and record low activation energy. It offers 1000-fold enhancement in conductivity (10^{-6} S/cm to 10^{-3} S/cm) with an activation energy of 0.11 eV. Atomic modeling and ^{13}C-SSNMR provide structural insights into the most-probable proton conduction pathway decorated by the post-synthetically anchored EG moieties.

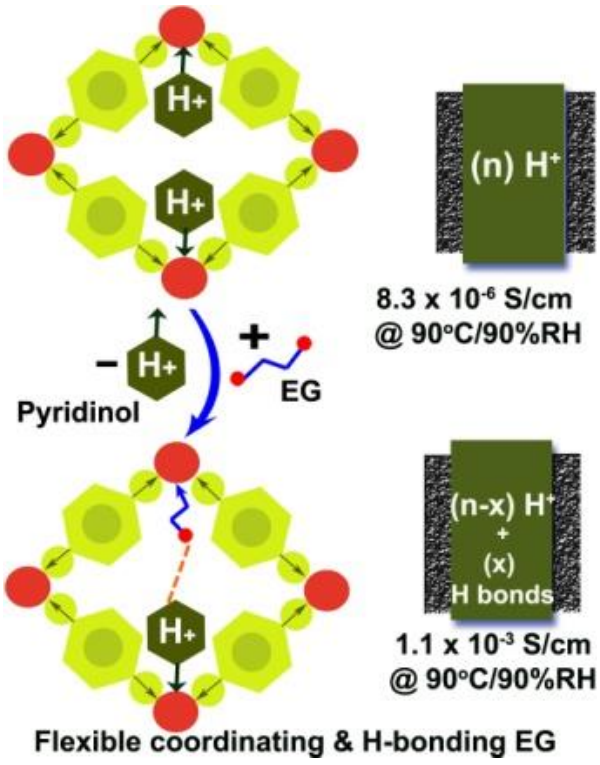

3I.A. Appendix

3I.A.1. Hydrogen bonds analyses using PLATON (WinGX)

1

Analysis of Potential Hydrogen Bonds and Schemes with d(D...A) < R(D)+R(A)+0.50, d(H...A) < R(H)+R(A)-0.12 Ang., D-H...A > 100.0 Deg

==========

Note: - ARU codes in [] are with reference to the Coordinates printed above (Possibly transformed, when MOVE .NE. 1.555)

==========

Nr Typ Res Donor --- H....Acceptor [ARU] D - H H...A D...A D - H...A A..H..A* A'..H..A" Sum(XY,YZ) Sum(XZ)

---

1 1 C(7) --H(11) ..O(6) [1556.01] 1.14 2.43 3.1047 116

Translation of ARU-code to Equivalent Position Code. [1556] = x,y,1+z.

1_EG

Analysis of Potential Hydrogen Bonds and Schemes with d(D...A) < R(D)+R(A)+0.50, d(H...A) < R(H)+R(A)-0.12 Ang., D-H...A > 100.0 Deg

==========

Note: - ARU codes in [] are with reference to the Coordinates printed above (Possibly transformed, when MOVE .NE. 1.555)

==========

Nr Typ Res Donor --- H....Acceptor [ARU] D - H H...A D...A D - H...A A..H..A* A'..H..A" Sum(XY,YZ) Sum(XZ)

---

1 Intra 1 C(7) --H(80) ..O(6) [1554.01] 1.14 2.43 3.1047 116

2 Intra 1 C(21) --H(86) ..O(20) [ ] 1.14 2.43 3.1047 116

3 Intra 1 C(35) --H(92) ..O(34) [1556.01] 1.14 2.43 3.1047 116

4 Intra 1 C(46) --H(97) ..O(71) [1565.01] 1.14 2.47 3.1032 113

5 Intra 1 C(49) --H(98) ..O(48) [ ] 1.14 2.43 3.1047 116

6 Intra 1 C(70) --H(104) ..O(27) [1545.01] 1.14 2.59 3.0633 104

7 Intra 1 C(70) --H(104) ..N(75) [1544.01] 1.14 2.25 3.3540 163

Translation of ARU-code to Equivalent Position Code. [1545] = x,-1+y,z; [1554] = x,y,-1+z; [1556] = x,y,1+z; [1565] = x,1+y,z; [1544] = x,-1+y,-1+z.

3

Analysis of Potential Hydrogen Bonds and Schemes with d(D...A) < R(D)+R(A)+0.50, d(H...A) < R(H)+R(A)-0.12 Ang., D-H...A > 100.0 Deg

==========

Note: - ARU codes in [] are with reference to the Coordinates printed above (Possibly transformed, when MOVE .NE. 1.555)

==========

Nr Typ Res Donor --- H....Acceptor [ARU] D - H H...A D...A D - H...A A..H..A* A'..H..A" Sum(XY,YZ) Sum(XZ)

---

1 1 C(103)--H(103) ..O(3) [1655.01] 0.93 2.58 3.1968 124

2 Intra 1 C(11) --H(206) ..O(1) [ ] 0.93 2.52 3.4323 166

Translation of ARU-code to Equivalent Position Code. [1655] = 1+x,y,z

3_EG

Analysis of Potential Hydrogen Bonds and Schemes with d(D...A) < R(D)+R(A)+0.50, d(H...A) < R(H)+R(A)-0.12 Ang., D-H...A > 100.0 Deg

==========

Note: - ARU codes in [] are with reference to the Coordinates printed above (Possibly transformed, when MOVE .NE. 1.555)

==========

Nr Typ Res Donor --- H....Acceptor [ARU] D - H H...A D...A D - H...A A..H..A* A'..H..A" Sum(XY,YZ) Sum(XZ)

---

1 Intra 1 C(11) --H(12) ..O(31) [ ] 1.07 2.57 2.9941 103

2 Intra 1 C(15) --H(16) ..O(37) [2666.01] 1.07 2.37 3.1729 130

3 Intra 1 C(20) --H(21) ..O(34) [2666.01] 1.07 2.31 3.2943 153

Translation of ARU-code to Equivalent Position Code. [2666.] = 1-x,1-y,1-z.

For C--H...Acceptor Interactions See: Th. Steiner, Cryst. Rev, (1996), 6, 1.

H-Bond classification [G.A.Jeffrey, H.Maluszynska & J.Mitra., Int.J.Biol.Macromol.(1985),7,336. 2-Centre (linear) D-H...X most prob. angle 160 o - also: G.A.Jeffrey & W.Saenger, Hydrogen Bonding in Biological Structures; 3-Centre (bifurcated) SUM of 3 angl. about H = 360o, Springer-Verlag, Berlin, 1991, pp 20. 4-Centre (trifurcated).

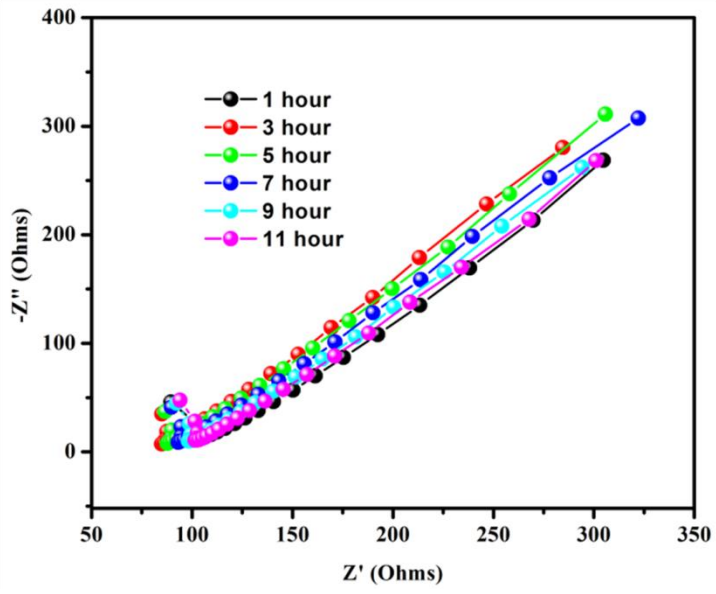

Figure 3I.A.1. Impedance spectra for **1_EG** at different equilibration time at 90˚C and 90% RH.

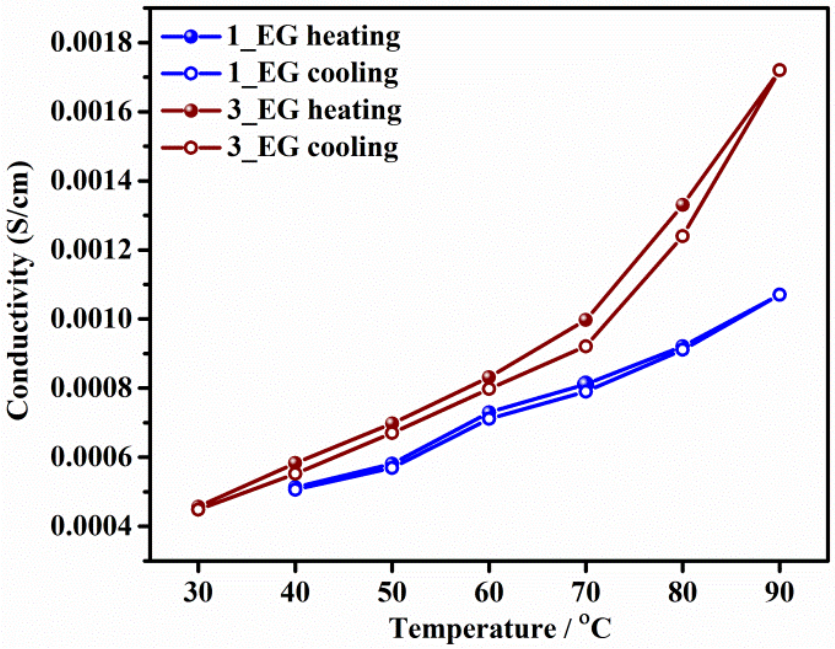

Figure 3I.A.2. The stability of the conductivity of **1_EG** and **3_EG** observed from heating and cooling cycles.

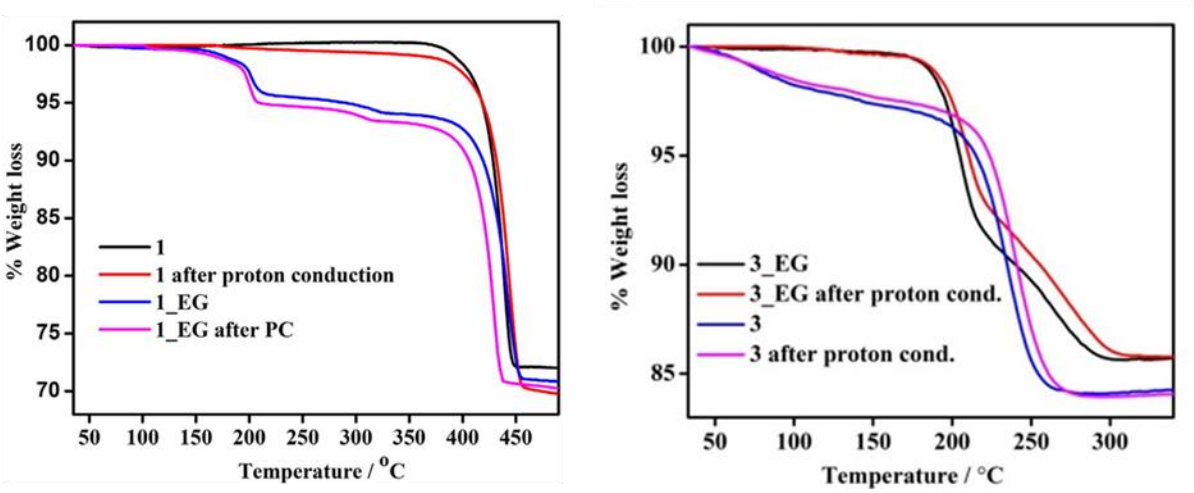

Figure 3I.A.3. Comparison of the TGA plots showing a good match in the observed weight losses between the as-made, EG loaded, and the post-treated samples, which corresponds to the loss of pyridinol.

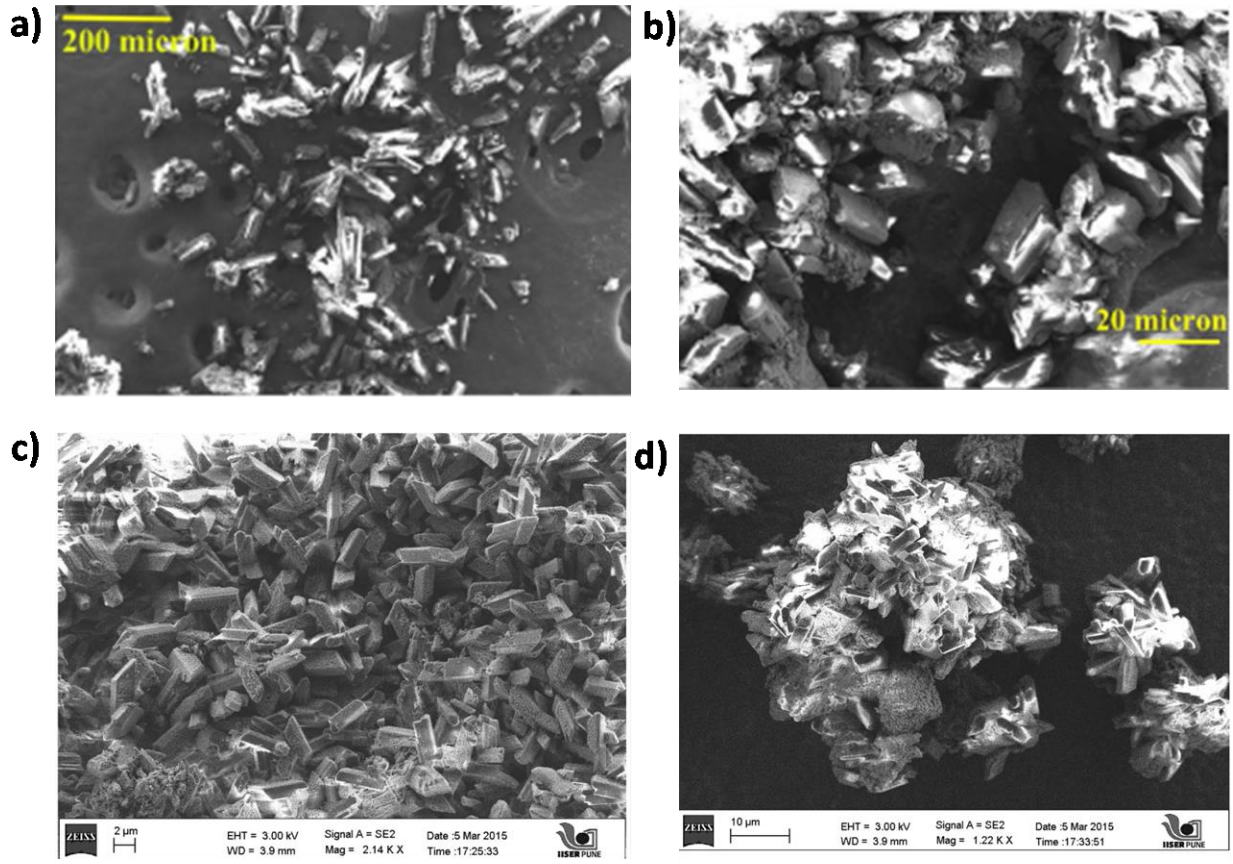

Figure 3I.A.4. Field emission SEM images of the (a) **1_EG,** (b) post impedance **1_EG,** (c) **3_EG** and (d) the post impedance **3_EG** phases.

Table 3I.A.1. CHN values for both the phases before and after proton conduction

Sample	%N	%C	%H
1_EG before proton conduction	3.77	52.58	3.840
1_EG after proton conduction	3.82	52.59	3.870
3_EG before proton conduction	2.69	41.82	1.91
3_EG after proton conduction	2.71	41.96	2.021

Table 3I.A.2. Calculation of activation energy for 1_EG at 90% RH

T (˚C)	R(Ω)	Thickness (cm)	A (cm^2)	κ(S/cm)	1/T (K^{-1})	Log (κ)	R(Gas constant)	Slope	Ea (kJ/mol)
40	138.9	0.120	1.326	6.55E-04	0.0033	-7.3306			
50	133.5	0.1208	1.326	6.82E-04	0.0031	-7.2906			

60	128.9	0.1208	1.326	7.06E-04	0.0030	-7.2553	8.314	656.3	5.4564
70	126.8	0.1208	1.326	7.18E-04	0.0029	-7.2395			
80	120.0	0.1208	1.326	7.59E-04	0.0028	-7.1841			
90	84.42	0.1208	1.326	1.08E-03	0.0027	-6.8320			

Table 3I.A.3. Calculation of activation energy for **3_EG** at 90% RH

T (˚C)	R (Ω)	Thickness (cm)	A (cm^2)	κ(S/cm)	1/T (K^{-1})	Log (κ)	R(Gas constant)	Slope	Ea (kJ/mol)
30	131.9	0.08	1.326	4.57E-04	0.0033	-7.6904	8.314	2335	19.4198
40	103.5	0.08	1.326	5.83E-04	0.0031	-7.4479	8.314		
50	86.4	0.08	1.326	6.98E-04	0.0030	-7.2673	8.314		
60	72.6	0.08	1.326	8.31E-04	0.0030	-7.0933	8.314		
70	60.46	0.08	1.326	9.97E-04	0.0029	-6.9103	8.314		
80	45.45	0.08	1.326	1.33E-03	0.0028	-6.6249	8.314		
90	35.16	0.08	1.326	1.72E-03	0.0027	-6.3682	8.314		

Chapter 3II

10000-fold Enhancement in Proton Conductivity of a MOF by Post-synthetic Doping of Cesium Ions in the Framework

2018

3II.1. Materials and methods

All the organic chemicals were purchased from Sigma Aldrich. The metal salts were procured from Alfa Aesar. All reagents and solvents were used without any further purification.

3II.1.1 Synthesis procedure

Milligram scale synthesis:

Synthesis of 1: A mixture of $Mg(NO_3)_2 \cdot 6H_2O$/terephthalic acid/4-hydroxypyridine (1:1:2 molar ratio) in DMA (5 mL) was sealed in a Teflon-lined stainless steel vessel and was heated at 140˚C for 2 days. The reaction system was then cooled to room temperature. The rod-shaped crystals were collected by filtration by using methanol and acetone. $C_{13}H_9MgNO_5$ (283.52): calcd. C: 55.07%, H: 3.20%, N: 4.94%; found C: 54.80%, H: 3.08%, N: 4.82%.

Synthesis of 1_Cs: A saturated solution of Cs_2CO_3 was prepared in methanol (10 mL) and water (0.5 mL). To this solution, **1** was added, and the mixture was kept at room temperature for 24 h. It was then filtered by using methanol and acetone. The Cs loading was monitored by TGA, ICP, and EDAX.

3II.1.2. Characterization and analytical methods:

Thermogravimetric analysis:

Thermogravimetry was carried out on NETSZCH TGA-DSC system. The TGAs were done under N_2 gas flow (20ml/min) (purge + protective), and samples were heated from RT to 800˚C at 5 K/min.

Composition of 1: $Mg(C_8O_4H_4)(C_5NOH_5)$: A weight loss of 33.50% between 350 to 450˚C corresponds to the loss of coordinated pyridinol.

Composition for 1_Cs: $Mg_4(C_8O_4H_4)_4(C_5NOH_5)_4Cs(H_2O)_7$

Molecular Weight: 1392.08 g/mol (from TGA)
TGA: Observed weight loss for water till ~350˚C = ~8.7%.
Calculated weight loss for water = 9.05%

The two step weight loss is due to free water as well as water coordinated to Cs. The second weight loss (~24.25%) corresponds to pyridinol.

3II.2. The motivation for the work

As discussed in chapter 3I, loading ethylene glycol in **1** helped us achieve 1000-fold enhancement in the proton conductivity value (10^{-3} S/cm). The commercially used electrolyte, nafion, conducts at 10^{-2} S/cm and therefore, the target value to be achieved is either more or equal to 10^{-2} S/cm. Further improvement is needed in the conductivity of **1**. We recently published a study wherein a practically non-conducting porous organic polymer containing phenolic pores was converted into a conducting one by loading Li^+ (Figure 3II.1). The high hydration ability of Li^+ was responsible for the significantly improved proton conductivity[34].

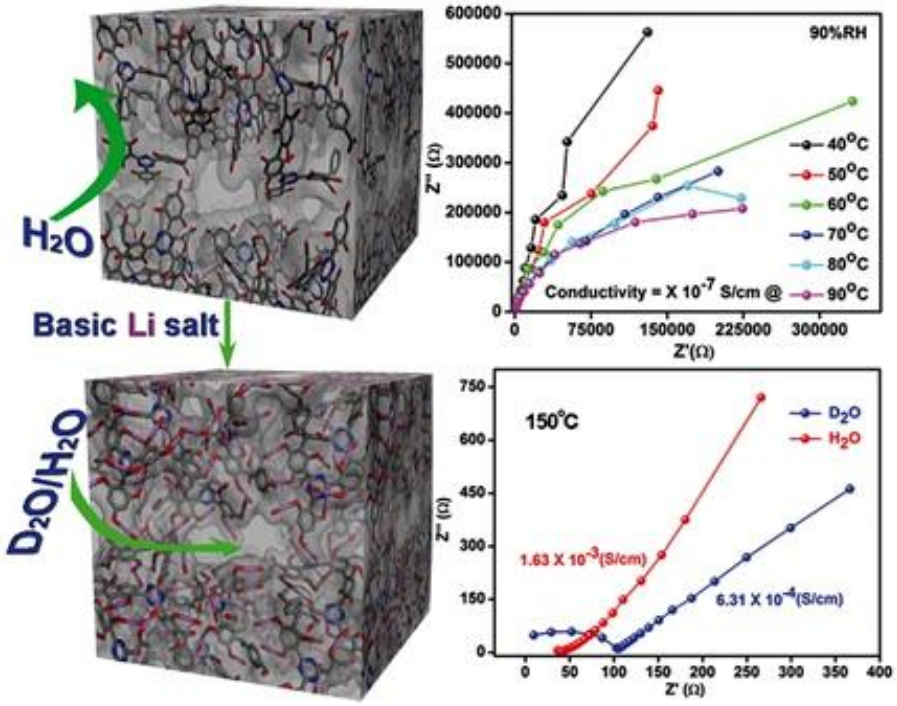

Figure 3II.1. A schematic showing improved conductivity of a triazine based polymer upon loading Li^+ ions. (Adapted from ref. 32)

We attempted a similar Li^+ loading on **1** but the MOF did not show any tendency to load the ion despite of the rigorous attempts made. Characterization techniques like elemental analysis, TGA, and ICP were used to confirm the lack of the loading. The MOF (**1**) has a dense

framework and the pores are very tight to start with. Considering that the Li^+ has an effective diameter of 600 pm in its hydrated form, it does not appear to be the suitably sized ion[35]. Interestingly, in comparison to Li^+, the Cs^+ ion has an effective diameter of 250 pm in its hydrated form, which is appreciably smaller. Also, it can function the same way as Li^+ in terms of bringing in more of the acidic, coordinated water into the framework for facile proton conduction. Hence, Cs^+ loading was attempted. As anticipated, we observed easy loading of Cs^+ ions by simply suspending **1** in a methanolic solution of Cs_2CO_3.

3II.3. Results and Discussion

3II.3.1. Structure of the proton conducting metal organic framework

The structure of **1** was solved by single-crystal X-ray diffraction and has already been discussed in chapter 2 in detail. For the ease of visualizing and reading, a very brief description is given here. The structure of **1** is made up of Mg center that is octahedrally coordinated and is crystallographically unique. Two pyridinol oxygen atoms and four terephthalate oxygen atoms bind to each Mg center. Both the pyridinols and terephthalate groups are μ-2 bridging giving rise to an inorganic ⋯Mg–O–Mg–O–Mg⋯ chain which is cross-linked by the terephthalate units. The pyridinols remain terminally bound and dangling into the pore of the MOF. They line the one-dimensional rhombic-shaped channels running along the c axis (Figure 2.2). The pyridinols lining these channels are present in zwitterionic form, wherein, the protons reside on the pyridyl nitrogen sites. When viewed along the a-axis, we observe that the pyridinols are pretty far spaced (ca. 3.8 Å, N–N distance, Figure 3II.2 b), leaving the structure with hardly any hydrogen bonds. Also, there is no free or coordinated or free water present in the structure. This explains the poor proton conductivity value of **1** (10^{-6} S/cm).

1_Cs is obtained by soaking **1** in a saturated methanolic solution of Cs_2CO_3. The amount of Cs loading can be controlled by varying the soaking time. However, the loading of Cs^+ is very reproducible. We could load the same amount of Cs^+ across different batches by keeping the soaking time constant. About 10% Cs^+ ions in their hydrated form could be introduced in place of the pyridyl protons by soaking **1** for 24 hours in the aqueous methanol medium (Figure 3II.2 c). It is highly likely that these Cs^+ ions can reside in the space between the adjacent pyridinol

units and get coordinated to the N-centers. Such positioning would result in a percolating hydrogen bond pathway all along the 1-D channels formed by the terephthalate framework.

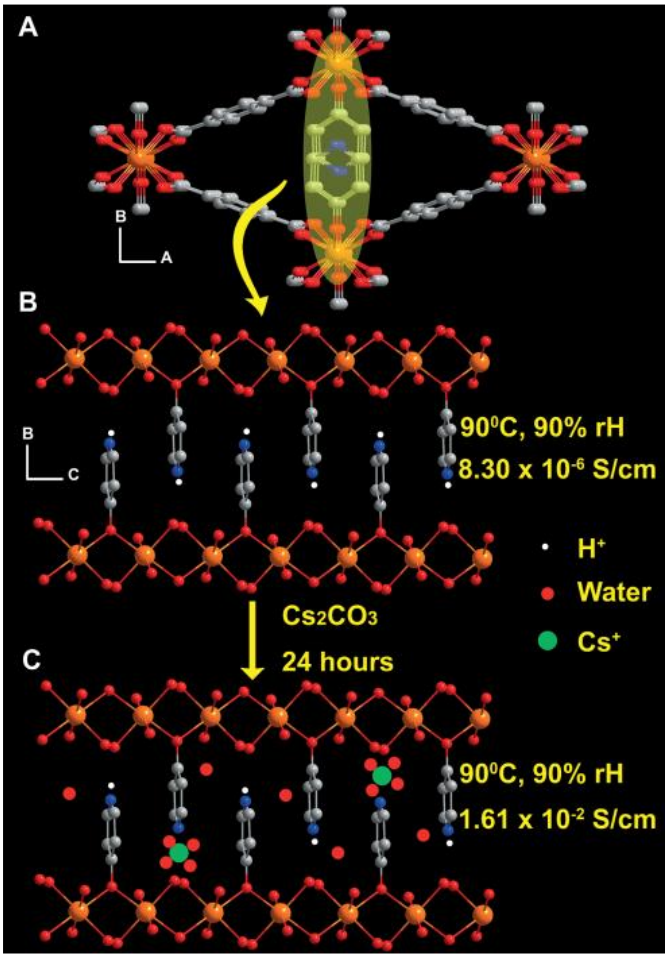

Figure 3II.2. (a) Structure of **1** showing the channels wherein the protonated pyridinols are located. (b) A view of the channels along the a-axis showing the zigzag arrangement of the coordinated pyridinols and the conductivity. (c) Random doping of Cs^+ (ca. 10 %) is represented schematically. Note: Cs^+ would be expected to have much higher coordination but is shown as four coordinate for clarity. Orange, Mg; red, O; gray, C; blue, N.

This would give rise to a smooth and facile proton transfer with very little hindrance from the coordinatively saturated Mg metal centers. Typically, hydrated cesium ions coordinate to six or seven water molecules, which would mean that as humidity is introduced, these ions can actively construct such hydrogen bond paths with the help of water.

3II.3.2. Bulk phase characterization

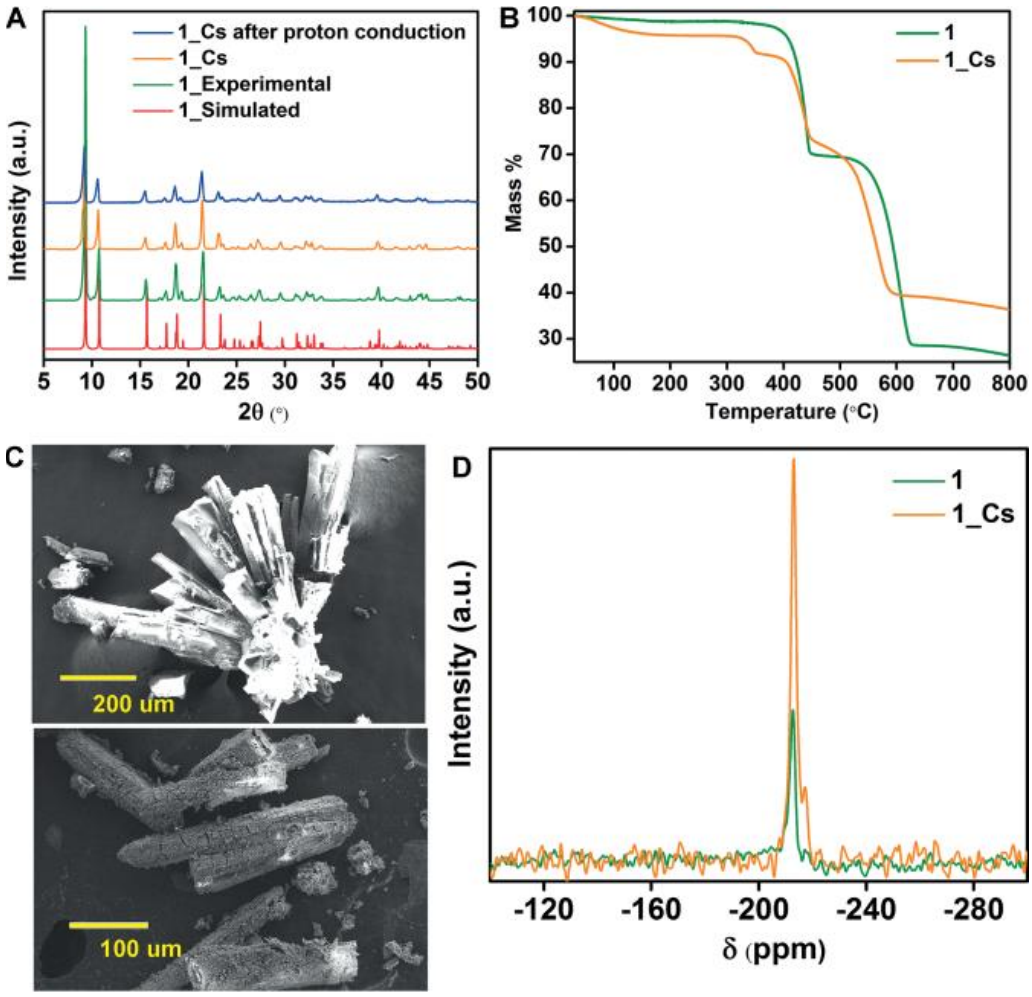

Figure 3II.3. (a) Bulk purity and characterization of the different phases by using powder XRD analysis. (b) Thermogravimetric curves of **1** and **1_Cs** showing increased hydration with the Cs loaded phase and the weight-loss step owing to pyridinol in both cases. (c) Field-emission scanning electron microscopy images of **1** and **1_Cs**. During Cs loading, the surfaces of the crystals are attacked, but the powder XRD pattern indicates that the crystallinity is maintained. (d) Solid-state ^{15}N NMR spectra of **1** and **1_Cs** showing the presence of two types of nitrogen atoms in the latter.

Powder X-ray diffraction confirms the phase purity of the two MOFs (Figure 3II.3 a). On loading Cs^+ ions, the PXRD doesn't change proving that the structure of **1_Cs** is the same as of **1**. Thermogravimetric analysis (TGA) was used to monitor the Cs loading. TGAs were performed from 30˚C to 800˚C under a nitrogen atmosphere and at a heating rate of 5˚C/min (Figure 3II.3 b). From the TGA data, the composition was found to be as

$Mg_4(C_8O_4H_4)_4(C_5NOH_5)_4Cs{\cdot}7H_2O$. **1_Cs** has weight-loss steps at 100˚C and 300˚C that have been attributed to the loss of free solvents (probably methanol) and water molecules coordinated to Cs, respectively. The highly oxophilic magnesium centers bind to water strongly[36], which increases the acidity of the coordinated water. This explains why water leaves at such high temperature. Introduction of Cs^+ into the MOF seems to increase the amount of such strongly coordinated water, a feature which is absent in **1**. As a result, the Cs^+ ions directly increase the concentration of acidic water in the MOF (Note: Water molecules coordinated to Lewis acidic metal centers tend to be acidic). Elemental analysis [Energy Dispersive X-ray analysis (EDXA) and CHN analysis] was used to further verify the composition of **1_Cs** (Tables 3II.A.1, 3II.A.2, Figures 3II.A.1, 3II.A.2). The CHN values (%) were found (calcd.) to be C: 44.34 (44.86), N: 4.02 (4.02), and H: 2.79 (3.55). Inductively coupled plasma (ICP) was also carried out to confirm the percentage of Cs and Mg in the structure. The Mg values matched closely with the composition calculated from TGA (observed/calcd.: 6.84%/6.98%) but, the percentage of Cs^+ ions could not be confirmed despite repeated attempts.

3II.3.3. Solid State ^{15}N-NMR studies

We carried out NMR spectroscopy to further confirm the way Cs^+ ions load in the framework. From the solid-state ^{15}N NMR spectroscopy it was found that the Cs^+ ions replace some of the pyridyl protons. In **1_Cs**, the resonance for the pyridyl nitrogen atom has a distinct shoulder, which was absent in **1**. This suggests the presence of two types of nitrogen atoms in **1_Cs** (one that's associated with the protons and the other associated with the Cs^+ ions) as compared to only one type protonated pyridyl nitrogen in **1**, (Figure 3II.3 d).

3II.3.4. Proton conductivity studies

The alternating current (ac) impedance spectra were measured on the pelletized samples from 30 to 90 % RH at 90˚C (Figure 3II.4 a) and from 30 to 90˚C at 90% RH (Figure 3II.4 b). The results were then compared with the conductivities of **1** (Table 3II.A.3, 3II.A.4, Figure 3II.A.3). The conductivity of **1_Cs** (1.61×10^{-2} S/cm at 90˚C and 90% relative humidity) was found to be very high relative to that of **1** (8.30×10^{-6} S/cm at 90˚C and 90% RH). An exciting observation was made that the resistance in case of **1_Cs** did not change much when the temperature is varied at 90% RH (Figure 3II.4 c).

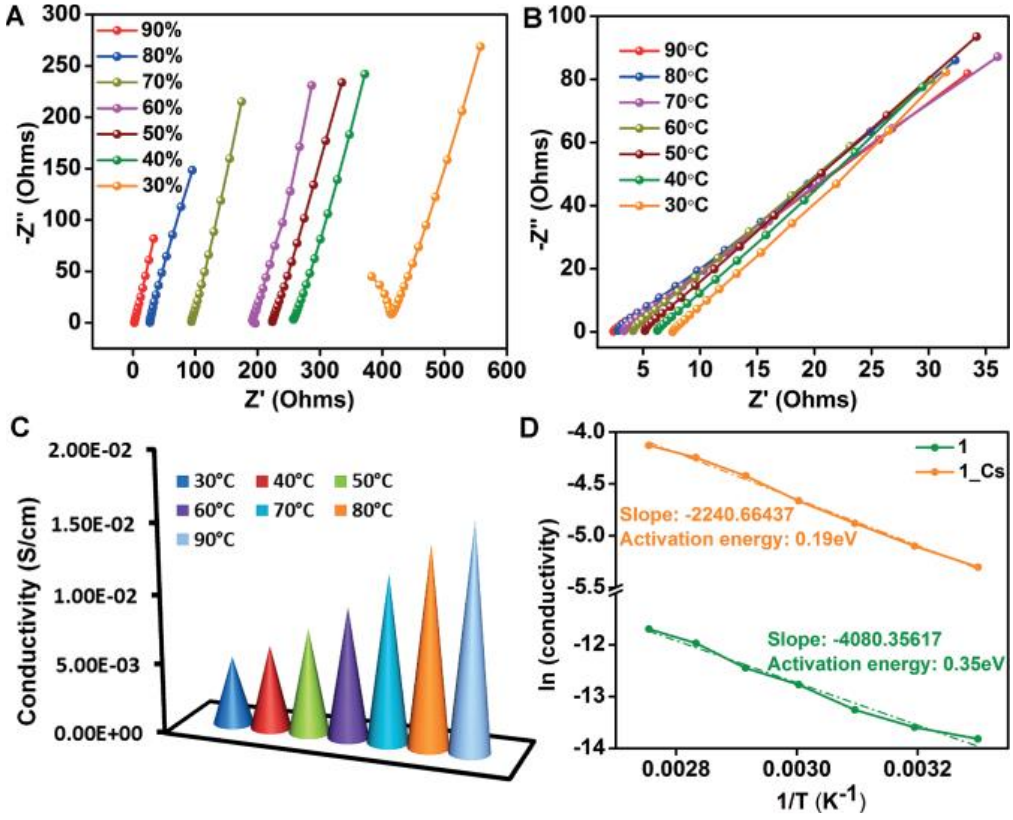

Figure 3II.4. (a) Nyquist plots from ac impedance spectroscopy measurements showing variation in the conductivities with relative humidity at 90 ℃ for **1_Cs**. (b) Nyquist plots showing variation in the conductivities with temperature at 90 % rH. (c) Plot showing the increase in conductivity with temperature indicating Arrhenius behavior. (d) Comparison of the activation energies for proton conduction in **1** and **1_Cs** showing the near-halving of the activation energy upon 10 % Cs loading.

This made us suspect some electronic contribution to the overall conductivity which led us to perform two-probe direct current (dc) experiment. The measurements were conducted for both **1** and **1_Cs** at room temperature. The resultant I–V curves confirmed the lack of any electronic contribution (Figure 3II.5, **1** was measured as a control). Hence, it was concluded that a high value of conductivity (4.97×10^{-3} S/cm) was attained even at 30˚C, 90 % RH, and a further increase to 1.61×10^{-2} S/cm at 90˚C happens steadily. At this high humidity, Cs^+ in all probability attains high levels of hydration even at lower temperatures. The proton conductivity was very reproducible and consistent across different batches. It has a low activation energy of 0.19 eV signifying that the conduction happens via Grotthus mechanism[26]. The low activation energy also rules out the possibility of conduction via Cs ions. Cs ions being bulkier compared to protons will be expected to have higher activation energies when compared to the lighter

protons. From the literature[37], it is seen that Cs ions conduction has higher activation energies (> 0.4 ev). The activation energy for 1_Cs is calculated to be 0.19 eV, which is very low for Cs conduction. Ideally, the origin of conductivity due to only protons and not Cs ions can be confirmed by very complex electrode blocking experiment. This experiment is quite complex (requires optimization) and is time consuming, unfortunately, we do not have access to the instrument for such longer periods.

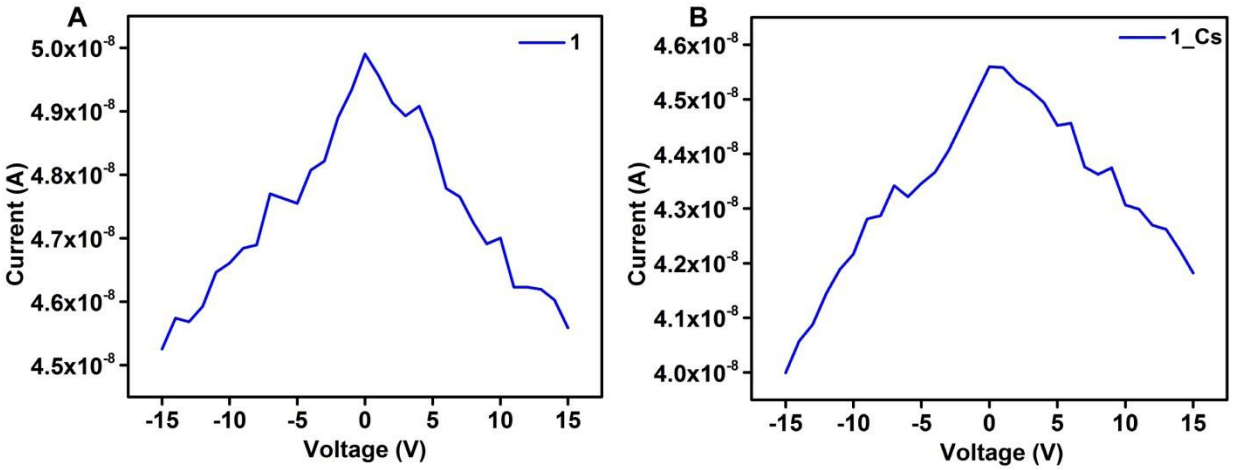

Figure 3II.5. IV curves measured for A) **1** and B) **1_Cs** using 2-probe. Both the samples showed no electronic contribution to the conductivity.

To confirm the effect of different loadings on proton conduction, we carried out impedance analysis on two different Cs loadings. It was observed that upon increasing the loading to ~20%, the conductivity value decreased to 1.96×10^{-3} S/cm (10% Cs: 1.61×10^{-2} S/cm at 90˚C/90% RH,) under the same conditions (Figure 3II.6 a). **1** has a comparatively much less porous framework than some of the recently reported proton-conducting MOFs[18-21,38]. Incorporating Cs^+ ions seems to provide sites with acidic water which help generate proton conduction pathway. However, the porosity could be blocked in this denser framework if the concentration of Cs^+ is increased beyond a certain level. This, in turn, minimizes the likelihood of hosting any more water molecules. To confirm this, we ran water–vapor sorption experiments on both **1_Cs** (10%) and **1_Cs** (20%) (Figure 3II.6 b). The saturation water uptake for **1_Cs** (10%) was almost double that of **1_Cs** (20 %) [**1_Cs** (10%) =0.75 mmol/g; **1_Cs** (20%) = 0.41 mmol/g]. This confirms that the relative concentration of Cs^+ ions plays a major role in the

proton conduction, which can be controlled very easily in this MOF. Loading below 10% could not be characterized consistently, and hence, we have not presented the results.

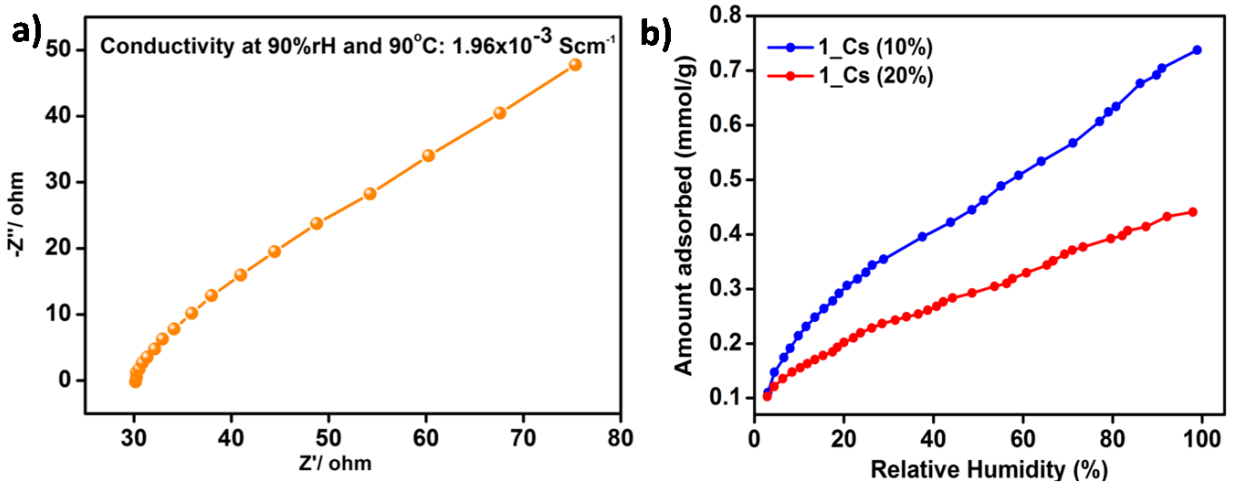

Figure 3II.6. (a) Nyquist plot from ac-impedance spectroscopy measurements at 90˚C and 90% RH and for ~20% loaded sample. (b) The water vapor adsorption isotherm collected at room temperature (298K). Higher Cs loadings could be blocking the porosity inhibiting further loading of water.

3II.3.5. Post-impedance stability

The post-impedance stability of the samples was confirmed by comparing the before and after-impedance phases by using different analytical techniques. The powder pattern of both the initially loaded sample and post-impedance sample matched extremely well (Figure 3II.3 a). TGA also showed a good match between the decomposition profiles of these phases, which confirmed the absence of any kind of decomposition of the sample under the measurement conditions (Figure 3II.A.4). The constant compositions of the pre- and post-measurement samples were confirmed by elemental analysis (Table 3II.A.1) and the Cs and Mg weight percentages were determined via EDAX (Table 3II.A.2). Also, the percentage of Mg obtained from ICP for pre- and post-impedance analyses samples matched well (as- synthesized **1_Cs**: 6.84; post-proton conduction **1_Cs**: 6.75 %).

3II.4. Conclusions

In conclusion, we have enhanced the proton conductivity of **1** using a post-synthetic strategy wherein the protons of zwitterionic pyridinol are partially exchanged with Cs^+ ions.

These hard ions bring in coordinated water, which tend to be acidic, into the framework resulting in better hydrogen-bonded proton conduction pathways. This approach led to a drastic increase in the conductivity value (10000-fold). **1_Cs** exhibited a humidity-dependent proton conductivity of 1.61×10^{-2} S/cm. This conductivity is comparable to some of the highest values reported for MOFs[18,19,39]. Moreover, the new conduction pathway provided a low energy barrier for proton hopping by Grotthus mechanism, lowering the activation energy to almost half of **1**. Also, it was established that an optimal loading of Cs^+ ions is critical to achieve maximum proton conduction. This study provides a potential approach to control the proton-conduction in MOF materials via simple post-synthetic loading methods, to bring them closer to being fuel-cell electrolytes.

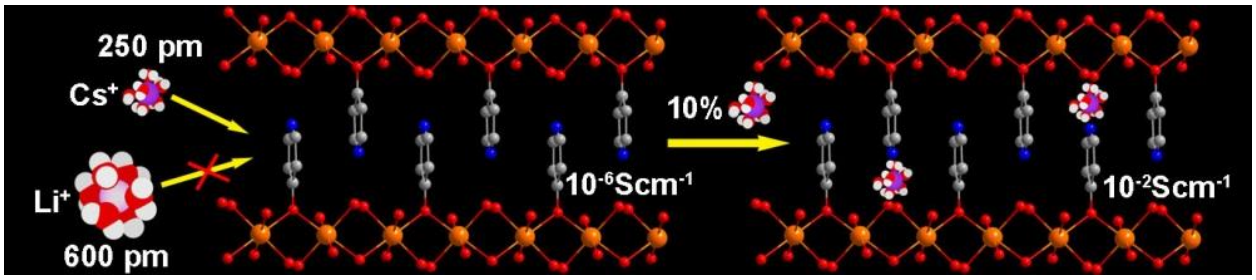

3II.A. Appendix

Table 3II.A.1. Elemental analysis (CHN analysis) for **1_Cs** before and after proton conduction.

	Observed values (%)		**Calculated values (%)**
Element	**Before proton conduction**	**After Proton conduction**	
C	44.34	44.71	44.86
N	4.02	3.97	4.02
H	2.69	2.68	3.55

Table 3II.A.2. Elemental analysis (EDAX) for **1_Cs** before and after proton conduction.

Element	**Weight % (observed)**		**Weight % (calculated)**
	Before proton conduction	**After proton conduction**	
Batch 1:			
Mg	7.47	6.91	6.98
Cs	10.13	9.38	9.55
Batch 2: (used for elemental mapping)			
Mg	6.93	-	6.98
Cs	9.95	-	9.55

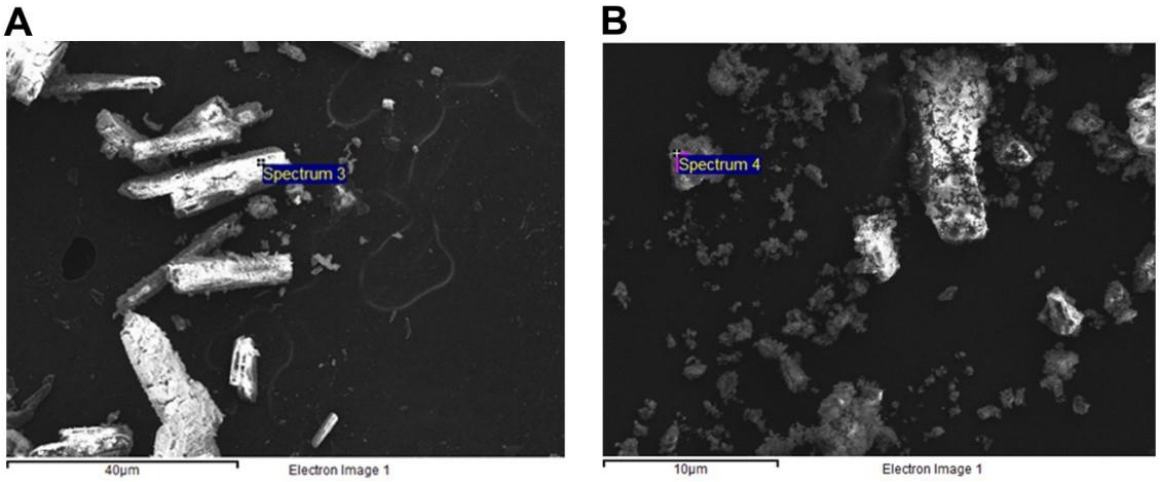

Figure 3II.A.1. FE-SEM image showing the region where EDAX was carried out for **1_Cs.** A) Before proton conduction B) After proton conduction

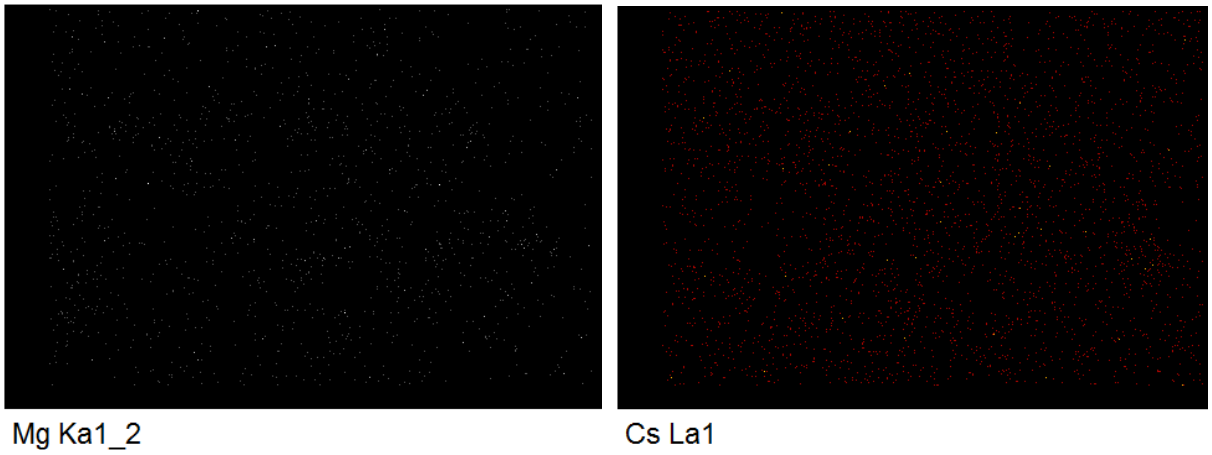

Figure 3II.A.2. Elemental mapping from EDAX analysis.

Table 3II.A.3. Variation of conductivity with temperature at 90%rH and calculation of activation energy for **1_Cs.**

T (°C)	R (Ω)	Thickness (cm)	Area (cm^2)	κ(S/cm)	1/T (K^{-1})	Log (κ)	R(Gas constant)	Slope	Ea (kJ/mol)
30	7.58	0.05	1.326	4.97E-03	0.0033	-5.3039	8.314	2240	18.623
40	6.18	0.05	1.326	6.10E-03	0.0031	-5.0997			
50	4.96	0.05	1.326	7.60E-03	0.0030	-4.8797			
60	3.99	0.05	1.326	9.43E-03	0.0030	-4.6636			
70	3.14	0.05	1.326	1.20E-02	0.0029	-4.4226			
80	2.63	0.05	1.326	1.43E-02	0.0028	-4.2453			
90	2.34	0.05	1.326	1.61E-02	0.0027	-4.1285			

Table 3II.A.4. Variation of conductivity with relative humidity at 90˚C for **1_Cs.**

RH (%)	R (Ω)	Thickness (cm)	Area (cm^2)	K (S/cm)
30	410.84	0.05	1.32665	9.17E-05
40	257.63	0.05	1.32665	1.46E-04
50	223.58	0.05	1.32665	1.69E-04
60	191.42	0.05	1.32665	1.97E-04
70	91.17	0.05	1.32665	4.13E-04
80	26.86	0.05	1.32665	1.40E-03
90	2.34	0.05	1.32665	1.61E-02

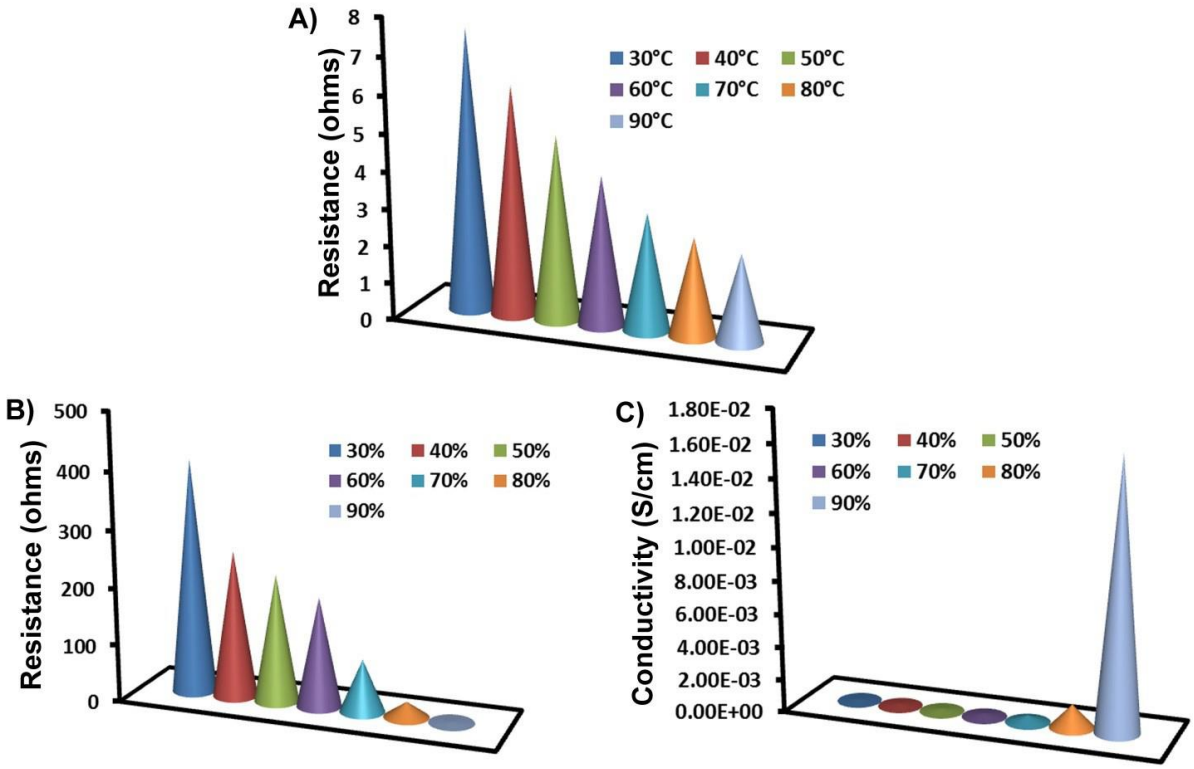

Figure 3II.A.3. Figure shows the variation of A) resistance with respect to temperature at a constant 90% RH, B) resistance with respect to relative humidity at constant 90°C and C) conductivity with different relative humidity at 90°C for **1_Cs**.

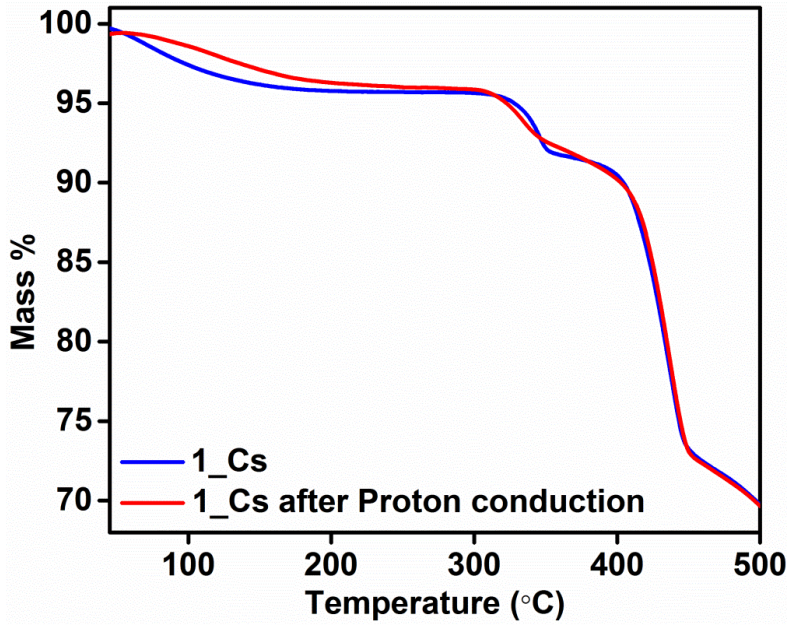

Figure 3II.A.4. TGA comparison of **1_Cs** before and after proton conduction.

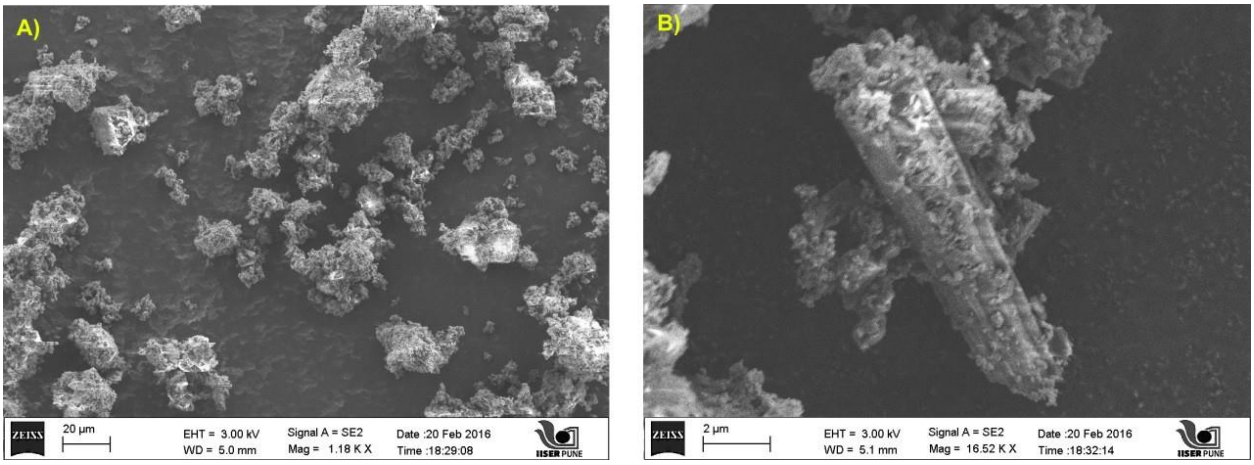

Figure 3II.A.5. SEM images of **1_Cs** after proton conduction.

Table 3II.A.5. Elemental analysis (EDAX) for ~20% Cs^+ loaded sample.

Element	Weight % (observed)
Mg	11.61
Cs	18.32

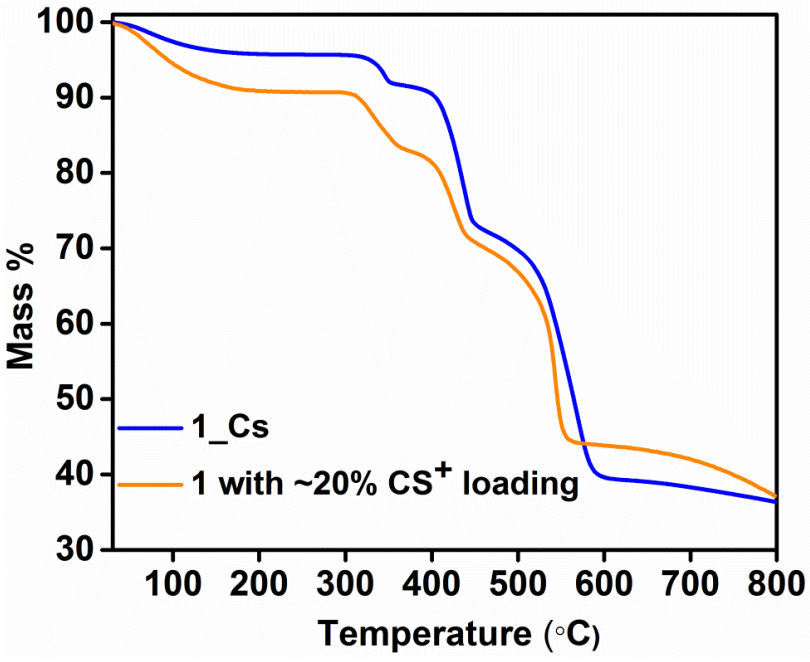

Figure 3.II.A.6. TGA comparison of **1_Cs** and **1_Cs** (20%).

Table 3II.A.6. Relative content of water as function of humidity (Estimated from water-vapor isotherm shown in figure below).

RH %	Amount adsorbed (mmol/g)	No. of water molecules
30	0.36	501.14
40	0.40	556.83
50	0.46	640.35
60	0.51	709.96
70	0.56	779.56
80	0.62	863.08
90	0.70	974.45

3.2. References.

1. Sadakiyo, M.; Yamada, T.; Kitagawa, H. *J. Am. Chem. Soc*. **2009**, *131*, 9906.
2. Ramaswamy, P.; Wong, N. E.; Shimizu, G. K. H. *Chem. Soc. Rev*. **2014**, *43*, 5913.
3. Yoon, M.; Suh, K.; Natarajan, S.; Kim, K. *Angew. Chem. Int. Ed*. **2013**, *52*, 2688.
4. Yoon, M.; Suh, K.; Natarajan, S.; Kim, K. *Angew. Chem*. **2013**, *125*, 2752.
5. Yamada, T.; Otsubo, K.; Makiura, R.; Kitagawa, H. *Chem. Soc. Rev*. **2013**, *42*, 6655.
6. Eddaoudi, M.; Sava, D. F.; Eubank, J. F.; Adil, K.; Guillerm, V. *Chem. Soc. Rev*. **2015,** *44*, 228.
7. Papaefstathiou, G. S.; MacGillivray, L. R. *Coord. Chem. Rev*. **2003**, *246*, 169.
8. Sun, Y.; Zhou, H. C. *Sci. Technol. Adv. Mater*. **2015**, *16*, 11.
9. Eddaoudi, M.; Moler, D. B.; Li, H.; Chen, B.; Reineke, T. M.; O'Keeffe, M.; Yaghi, O. M. *Acc. Chem. Res.* **2001**, *34*, 319.
10. Kim, S. R.; Dawson, K. W.; Gelfand, B. S.; Taylor, J. M.; Shimizu, G. K. H. *J. Am. Chem. Soc*. **2013**, *135*, 963.
11. Cohen, S. M. *Chem. Rev*. **2012**, *112*, 673.
12. Nguyen, H. G. T.; Weston, M. H.; Farha, O. K.; Hupp, J. T.; Nguyen, S. T. *CrystEngComm*. **2012**, *14*, 4115.
13. Jones, C. G.; Stavila, V.; Conroy, M. A.; Feng, P.; Slaughter, B. V.; Ashley, C. E.; Allendorf, M. D. *ACS Appl. Mater. Interfaces* **2016**, *8*, 7623.
14. Horike, S.; Kamitsubo, Y.; Inukai, M.; Fukushima, T.; Umeyama, D.; Itakura, T.; Kitagawa, S. *J. Am. Chem. Soc.* **2013**, *135*, 4612.
15. Khatua, S.; A. K., Bar; Sheikh, J. A.; Clearfield, A.; Konar, S. *Chem. Eur. J*., **2017**, *24*, 872.
16. Sadakiyo, M.; Yamada, T.; Kitagawa, H. *J. Am. Chem. Soc*. **2014**, *136*, 13166.
17. Khatua, S.; Bar, A. K.; Konar, S. *Chem. Eur. J*., **2016**, *22*, 16277.
18. Phang, W. J.; Jo, H.; Lee, W. R.; Song, J. H.; Yoo, K.; Kim, B. S.; Hong, C. S. *Angew. Chem. Int. Ed.* **2015**, *54*, 5142.
19. Phang, W. J.; Jo, H.; Lee, W. R.; Song, J. H.; Yoo, K.; Kim, B.; Hong, C. S. *Angew. Chem*. **2015**, *127*, 5231.
20. Inukai, M.; Horike, S.; Umeyama, D.; Hijikata, Y.; Kitagawa, S. *Dalton Trans*. **2012,** *41*, 13261.

21. Ponomareva, V. G.; Kovalenko, K. A.; Chupakhin, A. P.; Dybtsev, D. N.; Shutova, E. S.; Fedin, V. P. *J. Am. Chem. Soc*. **2012**, *134*, 15640.
22. Taylor, J. M.; Dekura, S.; Ikeda, R.; Kitagawa, H. *Chem. Mater*. **2015**, *27*, 2286.
23. Sadakiyo, M.; Yamada, T.; Honda, K.; Matsui, H.; Kitagawa, H. *J. Am. Chem. Soc*. **2014**, *136*, 7701.
24. Sahoo, S. C.; Kundu, T., Banerjee, R. *J. Am. Chem. Soc*. **2011**, *133*, 17950.
25. Taylor, J. M.; Mah, R. K.; Moudrakovski, I. L.; Ratcliffe, C. I.; Vaidhyanathan, R. *J. Am. Chem. Soc*. **2010**, *132*, 14055.
26. (a) Vuilleumier, R.; Borgis, D. *Nat. Chem*. **2012**, 4, 432. (b) Agmon, N. *Chem. Phys. Lett*. **1995**, *244*, 456.
27. Goesten, M. G.; Juan-Alcañiz, J.; Ramos-Fernandez, E. V.; SankarGupta, K. B. S.; Stavitski, E.; Bekkum, H. v.; Gascon, J.; Kapteijn, F. *J. Catal*. **2011**, *281*, 177.
28. Ogawa, T.; Kamiguchi, K.; Tamaki, T.; Imai, H.; Yamaguchi, T. *Anal. Chem*. **2014**, *86*, 9362.
29. Reece, C.; Willock, D. J.; Trewin, A. *PCCP* **2015**, *17*, 817.
30. Lukose, B.; Supronowicz, B.; Petkov, P. S.; Frenzel, J.; Kuc, A. B.; Seifert, G.; Vayssilov, G. N.; Heine, T. *Phys. Stat. Sol. b*. **2012**, *249*, 335.
31. Nandi, S.; Werner-Zwanziger, U; Vaidhyanathan, R. *J. Mater. Chem. A*, **2015**, *3*, 21116.
32. Mullangi, D.; Nandi, S.; Shalini, S.; Sreedhala, S.; Vinod, C. P.; Vaidhyanathan, R. *Sci. Rep*. **2015**, *5*, 10876.
33. Phang, W. J.; Lee, W. R.; Yoo, K.; Ryu, D. W.; Kim, B; Hong, C. S. *Angew. Chem. Int. Ed.* **2014**, *53*, 8383.
34. Nandi, S.; Dhavale, V. M.; Shalini, S.; Werner-Zwanziger, U.; Singh, H.; Kurungot, S.; Vaidhyanathan, R. *Adv. Mater. Interfaces* **2015**, *2*, 1500301.
35. Kielland, J. *J. Am. Chem. Soc*. **1937**, *59*, 1675.
36. Reddy, K. R. K.; Suneetha, P; Karigar, C. S.; Manjunath, N. H.; Mahendra, K. N.; *J. Chil. Chem. Soc*. **2008**, *53*, 1653.
37. Otto, K.; Milberg, M. E, *J. Am. Chem. Soc*.**1967**,*50*, 513.
38. Taylor, J. M.; Komatsu, T.; Dekura, S.; Otsubo, K.; Takata, M.; Kitagawa, H. *J. Am. Chem. Soc*. **2015**, *137*, 11498.

39. Ramaswamy, P.; Wong, N. E.; Gelfand, B. S.; Shimizu, G. K. H. *J. Am. Chem. Soc*. **2015**, *137*, 7640.

Chapter 4

Wide-temperature Range Proton Conduction Realized in a Post-synthetically Modified MOF

2018

4.1. Introduction

Metal Organic Frameworks (MOFs) are increasingly being studied as electrolytes for fuel cells, owing to their well-defined framework structure with ordered pores. This makes them excellent for hosting functional guests[1-6]. Owing to their crystalline nature, MOFs provide room for atomic level designability and the chemistry around their framework can be tuned to function cooperatively with the guests to deliver the property of choice. Even in the well-established Nafion like polymer electrolytes, the proton conductivity arises out of the fine interplay between the host and the guest[7-12]. Proton conduction in MOFs has been realized both under humid and anhydrous conditions[1-6]. In most of the cases, the MOF framework consists of highly polar channels with an acidic lining[13-16]. The proton conductivity kicks in when an amphoteric species like water or a nitrogen heterocycle occupies such channels. For example, the sulphonate/phosphonate based MOFs have shown hydrous proton conduction of 2.1×10^{-2} S/cm at 85˚C and 90% RH[17]. Similarly, anhydrous proton conduction (T>120˚C) has been realized in an AlNDC MOF loaded with Imidazole[18] or in rare cases with a trace quantity of moisture trapped in highly oxophilic MOF[19]. With this insight, water-loving alkali metal ions have been introduced post-synthetically to accomplish substantial enhancement in proton conductivity[20,21]. Also, specific hydrogen bonding, coordinating guests have been strategically placed to develop tailor-made proton conduction pathways within the MOF channels[22,23].

However, merely combining these acid-base components in a MOF does not guarantee sufficient proton conduction. For example, having a relatively strong base in its protonated form occupying the pores of an anionic framework can make the water-assisted proton transfer difficult. So, the relative basicity plays a key role[24-26]. Also, obtaining a favorable, closely knit hydrogen bond pathway relies on the proximity of the proton carrying species. However, the location and the orientation of these guest species are dictated by the electrostatic/dispersive force optimization between the charged framework and the guest.

In summary, the performance of an electrolyte, to a large extent, depends on the strength of the acid/base, the availability of multiple hydrogen bonds linked transfer pathways and optimal electrostatic host-guest interaction. Also, for a wide temperature range proton conductor (RT to 150˚C), it becomes important to have a framework with an optimal pore size capable of simultaneously accommodating low and high boiling amphoteric guests[18,27-29]. We believe the

structural designability and chemical tunability of MOF gives an excellent platform to stitch together all these features through synthetic and post-synthetic approach. Though hydrous proton conductivity below the boiling point of water has been established in many MOFs, reports on anhydrous proton conducting MOFs are scanty. This is because the larger size and multiple heteroatom centers in such N-rich amphoteric guest can quite readily get stuck in tailor-made pockets and can get locked via relatively strong electrostatic interactions. This can restrict their dynamics leading to higher activation barriers. This makes it extremely difficult to guarantee proton conduction in a MOF embedded with larger amphoteric guests in comparison to the highly dynamic water-driven proton conductors.

In this chapter, we report three iso-structural anionic, three-dimensional Nd-Oxalate frameworks with different protonated heterocycles in the pore namely **4** (Imidazole), **5** (Aminotriazole), and **6** (Triazole). Using the three MOFs, we have demonstrated the effect of the pKa of the guest in the pore on the proton conductivity values of the MOF. Under humid conditions, all the three phases show proton conductivity but fail to show any conductivity under anhydrous conditions. **6** has the highest conductivity of 10^{-3} S/cm at 90˚C and 90% RH. From the crystal structure, we discerned that the triazoles are pretty far spaced to be able to form a hydrogen-bonded network in the absence of water and hence, no conduction at high temperature. Also, these protonated triazoles reside compactly in the MOF pores and are held by noticeable electrostatic interactions between the protonated nitrogen and the polar framework oxygens. This rules out the possibility of a vehicular motion assisted proton conduction even at temperatures as high as 150˚C. Hence, in a post-synthetic fashion, we loaded neutral triazoles on top of the already present protonated ones to bridge the gap. This is considering that neutral triazoles are amphoteric like water and can help in proton transfer just like water, but more crucially, being higher boiling moieties they can stay and participate in proton conductivity even under anhydrous conditions and can create pathways for a Grotthus type conduction, wherein the heterocylces can tumble in their own space and be able to transfer the proton to the adjacent neutral heterocycle especially at the higher temperatures. Through molecular simulations and DFT energy minimizations, using the Material Studio, and from Pawley refinements we have identified the potential positions of the post-synthetically loaded neutral triazole which seems to complete the required 3-D proton conduction pathway. Hence, a wide temperature range conductivity of 10^{-2} S/cm at 90˚C and 90% RH and of the order of 10^{-4} S/cm at 150˚C has been

achieved. The study brings in an important piece regarding acid-base control and a facile approach towards introducing proton conductivity into near-favorable MOFs, and we have also shown wide-temperature range conductivity, i.e., both humidity dependent as well as anhydrous conductivity from 30˚ to 150˚C.

4.2. Materials and Methods:

All the organic chemicals were purchased from Sigma Aldrich. The metal salts were procured from Alfa Aesar. All reagents and solvents were used without any further purification.

4.2.1. Synthesis procedure

Milligram scale synthesis:

4,$Nd(Ox)_2Im(H_2O).(CH_3OH)(H_2O)$, was synthesized using the approximate molar ratios of Neodymium nitrate, Oxalic acid dihydrate (Ox), Imidazole (Im) as 1:1.5:2. In a glass vial, 0.027 g of imidazole was dissolved in 5 ml methanol. To this solution was added 0.086 g neodymium nitrate. The mixture was then stirred for 15 minutes at RT. To this, 0.037 g oxalic acid dihydrate was added. The contents were heated at 70°C for 10 minutes and then kept at room temperature for 24 hours. A bluish pink microcrystalline powder was collected as a product by filtration using methanol and acetone. (Elemental analysis, observed/calculated: C – 20.09%/21.05%; H - 2.07%/2.65%; N–5.99%/6.14%). The air-dried sample gave a yield of ~ 80% (based on Mg).

5, $Nd(Ox)_2ATz(H_2O).(CH_3OH)(H_2O)$, was synthesized using the approximate molar ratios of Neodymium nitrate, Oxalic acid dihydrate, Aminotriazole (ATz) as 1:2:2. In a glass vial, 0.042 g of aminotriazole was dissolved in5 ml methanol. To this solution was added 0.109 g neodymium nitrate. The mixture was then stirred for 15 minutes at RT. To this, 0.047 g oxalic acid dihydrate was added. The contents were heated at 70°C for 10 minutes and then kept at room temperature for 24 hours. A bluish pink microcrystalline powder was collected as a product by filtration using methanol and acetone. (Elemental analysis, observed/calculated: C – 17.65%/17.80%; H - 2.311%/2.56%; N – 11.73%/11.86%). The air-dried sample gave a yield of ~ 85% (based on Nd).

6, $Nd(Ox)_2Tz(H_2O).(CH_3OH)(H_2O)$, was synthesized using the approximate molar ratios of Neodymium nitrate, Oxalic acid dihydrate, Triazole as 1:1.5:2. In a glass vial, 0.028 g of 1,2,4-triazole was dissolved in5 ml methanol. To this solution was added 0.085 g neodymium nitrate. The mixture was then stirred for 15 minutes at RT. To this, 0.037 g oxalic acid dihydrate was added. The contents were heated at 70°C for 10 minutes and then kept at room temperature for 24 hours. A product containing bluish-pink, very thin rod-shaped crystals, was collected by filtration using methanol and acetone. (Elemental analysis, observed/calculated: C – 18.04%/18.38%; H - 1.96%/2.42%; N – 8.97%/9.19%). The air-dried sample gave a yield of ~ 90% (based on Nd).

6_Tz, $Nd(Ox)_2Tz^+Tz(H_2O).(CH_3OH)(H_2O)$ was synthesized by stirring **6** in a methanolic solution of triazole at room temperature. 300 mg of **6** was added to 25 ml methanol. To this was added 92 mg of triazole. The contents were stirred for 24 hours at room temperature to load triazole in **6**. The product was then filtered using a copious amount of methanol and acetone. (Elemental analysis, observed/calculated: C – 19.08%/20.53%; H - 1.98%/2.68%; N – 16.69%/15.96%). The air-dried sample gave a yield of ~ 95% (based on Nd).

Easy scale-up was possible due to the ready precipitation of the MOFs in bulk quantities.

Gram scale synthesis:

4, $Nd(Ox)_2Im(H_2O).(CH_3OH)(H_2O)$, was synthesized using the approximate molar ratios of Neodymium nitrate, Oxalic acid dihydrate, Imidazole as 1:1.5:2. In a glass vial, 0.54 g of imidazole was dissolved in5 ml methanol. To this solution was added 1.72 g neodymium nitrate. The mixture was then stirred for 15 minutes at RT. To this, 0.74g oxalic acid dihydrate was added. The contents were heated at 70°C for 10 minutes and then kept at room temperature for 24 hours. A bluish pink microcrystalline powder was collected as a product by filtration using methanol and acetone.

5, $Nd(Ox)_2ATz(H_2O).(CH_3OH)(H_2O)$ was synthesized using the approximate molar ratios of Neodymium nitrate, Oxalic acid dihydrate, Aminotriazole as 1:2:2. In a glass vial, 0.84 g of aminotriazole was dissolved in50 ml methanol. To this solution was added 2.18 g neodymium nitrate. The mixture was then stirred for 15 minutes at RT. To this, 0.94g oxalic acid dihydrate was added. The contents were heated at 70°C for 10 minutes and then kept at room

temperature for 24 hours. A bluish pink microcrystalline powder was collected as a product by filtration using methanol and acetone.

6, $Nd(Ox)_2Tz(H_2O).(CH_3OH)(H_2O)$ was synthesized using the approximate molar ratios of Neodymium nitrate, Oxalic acid dihydrate, Triazole as 1:1.5:2. In a glass vial, 0.56 g of 1,2,4-triazole was dissolved in50 ml methanol. To this solution was added 1.70 g neodymium nitrate. The mixture was then stirred for 15 minutes at RT. To this, 0.74g oxalic acid dihydrate was added. The contents were heated at 70°C for 10 minutes and then kept at room temperature for 24 hours. A product containing bluish-pink, very thin rod-shaped crystals, was collected by filtration using methanol and acetone.

6_Tz, $Nd(Ox)_2Tz^+Tz(H_2O).(CH_3OH)(H_2O)$ was synthesized by stirring **6** in a methanolic solution of triazole at room temperature. 600 mg of **6**was added to 500 ml methanol. To this, was added 184 mg of triazole. The contents were stirred for 24 hours at room temperature to load triazole in **6**. The product was then filtered using a copious amount of methanol and acetone.

4.2.2. Characterization and analytical methods:

Single crystal structure determination:

Single-crystal data was collected on a Bruker SMART APEX four-circle diffractometer equipped with a CMOS photon 100 detector (Bruker Systems Inc.) and with a Cu Kα radiation (1.5418Å). The incident X-ray beam was focused and monochromated using Micro focus system (IμS). Crystal of **6** was mounted on nylon Cryo loop with Paratone-N oil. Data was collected at 173(2) K, integrated using Bruker SAINT Software and corrected for absorption using SADABS. The structure was solved by Intrinsic Phasing module of the Direct methods and refined using the SHELXTL 2014 software suite. All non-hydrogen atoms were located from an iterative examination of difference F-maps following which the structure was refined using the least-squares method. Hydrogen atoms were placed in geometrically riding mode.

4.3. Results and Discussion

4.3.1. Structure of the proton conducting metal organic frameworks (4-6).

A family of MOFs (**4**, **5** and **6**) was formed by reacting Nd-nitrate with oxalic acid in the presence of imidazole(**4**)/aminotriazole(**5**)/triazole(**6**) in methanol via a facile room temperature synthesis. Despite enormous attempts made **4** and **5** always precipitated as a microcrystalline powder. **6**, on the other hand, formed tiny rode shaped crystals. It crystallizes in monoclinic, $P2_1/c$ space group (a = 9.953Å, b=17.08Å, c=8.782Å, β=101.394°, V= 1463.75Å^3). The.

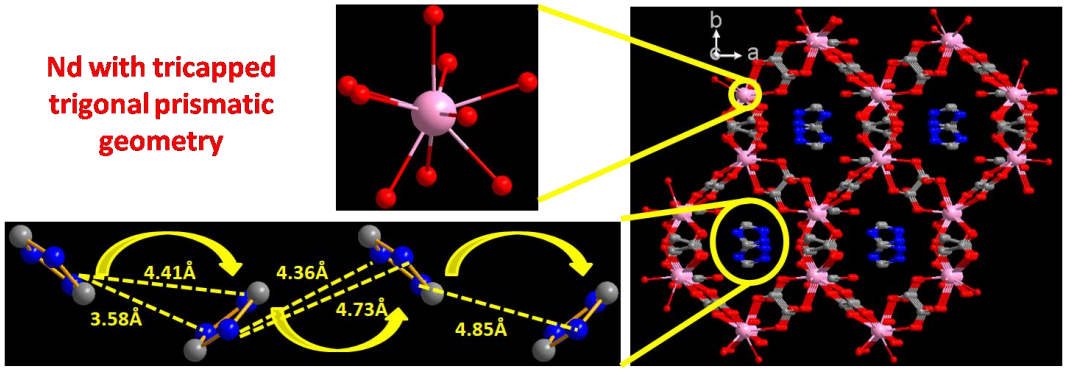

Figure 4.1. The 3-D anionic Nd oxalate framework with protonated triazoles in the rhombic-shaped channels and the coordination environment of Nd. The distances between the triazole moieties along the c-axis have been shown. Hydrogens are not shown for clarity. Color code: Pink: Nd, Blue: N, Red: O, Gray: C.

crystallographically unique Nd center is nine coordinated and exists in tricapped trigonal prismatic geometry (Figure 4.1). The coordination is satisfied by four oxalates and one water molecule. It has an anionic Nd-oxalate framework, $[Nd(Ox)_2]^{1-}$, wherein the out-of-plane oxalates cross-link the in-plane Nd-Oxalate honeycomb layers into a three-dimensional network. The framework comprises of rhombic channels along the a- and c-axes and also along the [111] direction with dimensions ~10 Å, ~12 Å, and ~10 Å, respectively (Figures 4.1 and 4.A.1). The charge-balancing protonated cationic triazoles occupy these channels

4.3.2. Bulk phase characterization

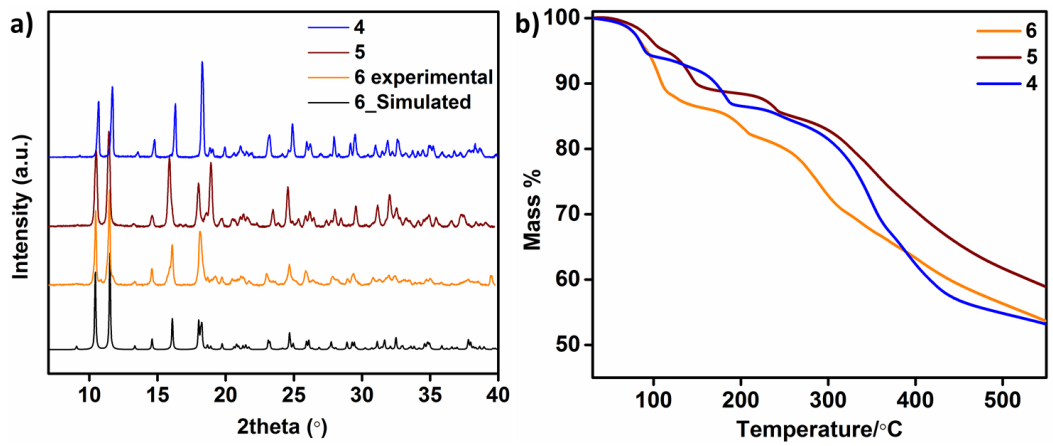

Figure 4.2. (a) Comparison of the powder XRD patterns of the MOFs showing the three phases to be isostructural. (b) TGA profiles for the three phases. They are all stable till ~250˚C.

The powder X-Ray pattern for **4** and **5** matched very well with that of **6** proving that the three phases are iso-structural (Figure 4.2 a). All the three MOFs precipitated as bulk-pure phases. The repeated synthesis, as well as the gram scale synthesis, produced samples with the similar PXRD and TGA profiles. From the TGA, the cationic guests were found to leave the structure at ~180˚C, 200˚C, and 250˚C for **4**, **5**, and **6** respectively, triggering a collapse of the framework (Figure 4.2 b).

4.3.3. Proton conductivity studies

The azoles being closely positioned to the oxalates, water and methanol provide a gas-tight percolating pathway for the protons to travel. More importantly, these solids are dense and have a negligible porosity which typically does not allow the fuel crossover (Figure 4.A.2). To assess the capability of these samples to work as solid electrolytes, we measured the alternating-current (ac) impedance spectra for the pelletized samples. The measurements were done from 30˚C to 90˚C at 90% relative humidity. The conductivity for **4**, **5** and **6** was found to be 1.17 $x10^{-4}$ S/cm, 9.09 $x10^{-4}$ S/cm, and 3.06 $x10^{-3}$ S/cm at 90˚C and 90% RH, respectively (Figure 4.3, Table 4.1).

The conductivity of the MOFs increased as the basicity of the guest loaded in the pore (pKa of imidazole: 6.9, aminotriazole: 4.41, triazole: 2.2)[30,31] decreased. Also, **6** has the highest conductivity and least activation energy, and therefore, it appears that the weakest base, triazole, seems to be the optimal amphoteric species capable of accepting and donating the protons from

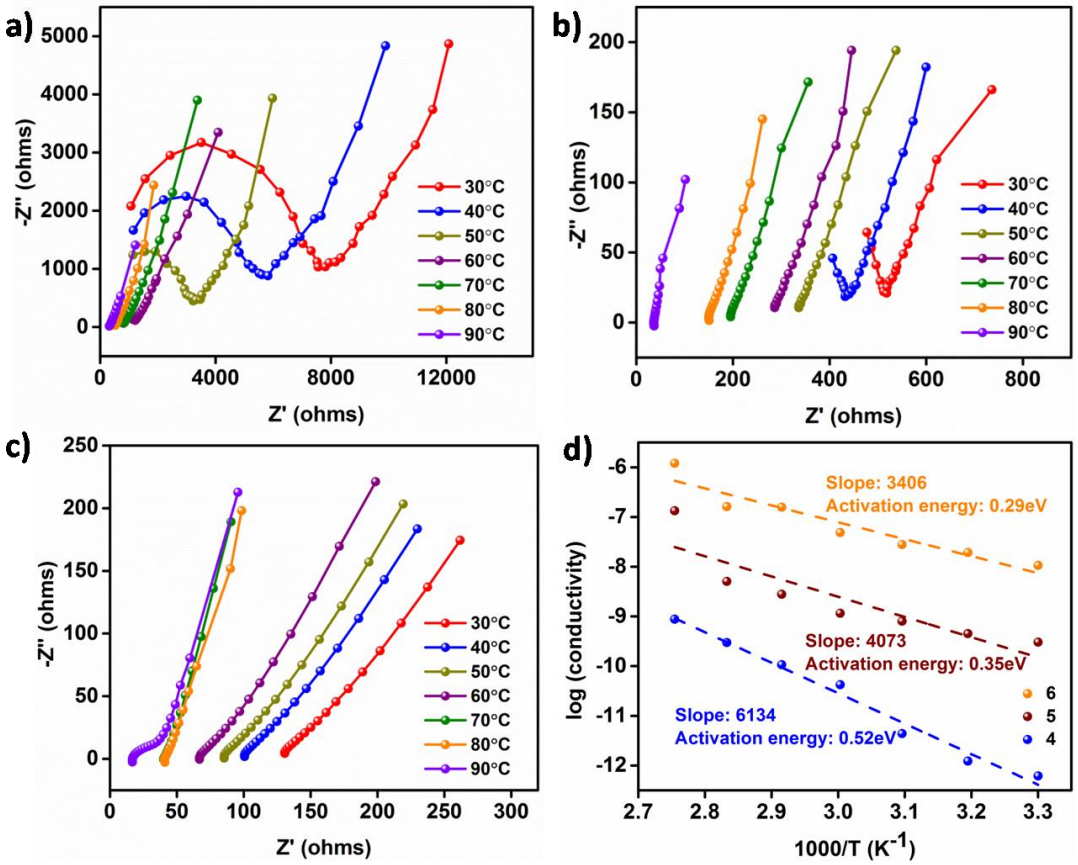

Figure 4.3. Nyquist plots for (a) **4**, (b) **5**, and (c) **6**. (d) The Arrhenius behavior of proton conductivity for the three phases.

the co-amphoteric guest, i.e., the water. Notably, the triazolates have comparable activation energy, and the stronger base imidazole falls nearly in the borderline of Grotthus/vehicular mechanism (Table 4.1).

Although the conductivity values for the three MOFs increased as the basicity of the guest in the pore decreased, the difference between the conductivities of **4** and **5** wasn't as high as the difference in their pKa values. The conductivities, of course, would have contributions from the structure. To verify this, we carried out the water adsorption on all three phases (Figure 4.4). The saturation water uptake for **4**, **5**, and **6** at 298 K are 5.3 mmol/g, 6.3 mmol/g, and 9.2 mmol/g, respectively. **4** showed abrupt uptake (type I) at lower humidities while the other two had weaker interactions at lower humidities but steadily improves at higher water loadings (type II).

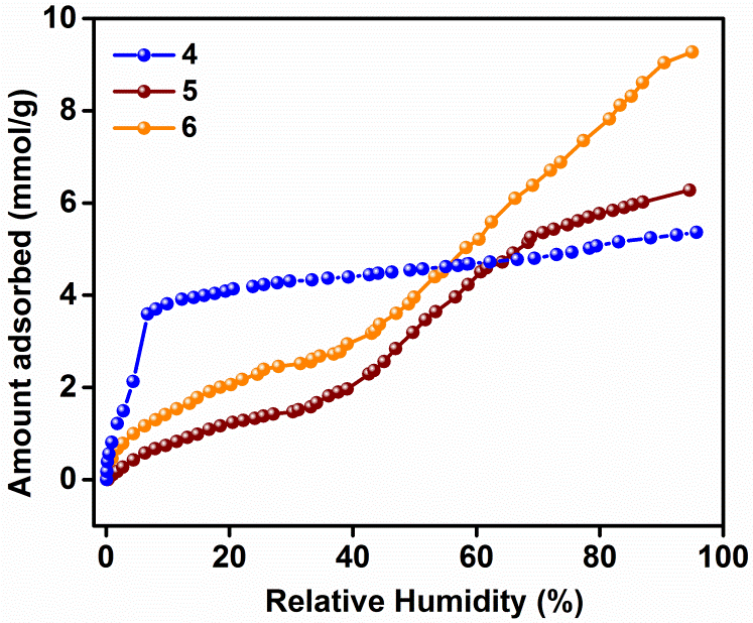

Figure 4.4. Water Sorption for the three phases at 298 K.

Most importantly, at 90% RH which is comparable to the highest humidity employed in the conduction measurements, **6** shows the highest water uptake suggesting that the high conductivity of the triazole phase most likely has contributions from the basicity and the structure.

Table 4.1. Table of comparison of proton conductivity and activation energy for **4**, **5**, and **6**.

MOF	Conductivity @ 90°C/90% RH (S/cm)	pKa for guest	Activation energy (eV)
4	1.17×10^{-04}	6.9	0.52
5	9.09×10^{-04}	4.4	0.33
6	3.06×10^{-03}	2.2	0.30

4.3.4. Post-synthetic modification

Surprisingly, despite the presence of amphoteric, protonated nitrogen heterocycles, none of the three phases showed any conductivity above 90˚C, which nullifies our hope on tuning these for wide temperature range proton conduction. For this, when we analyzed the single crystal structure of **6**, we realized that the water-free structure has heterocycles separated by

distances in the range of 3.5 Å to 4.8 Å (Figure 4.1). These are far spaced for a favorable proton conduction pathway. Since we have an anionic framework tightly holding the cationic guest within their narrow pores via strong electrostatic interactions, a facile across-the-channel movement may not be possible even at elevated temperatures. Also, in the absence of water, there are no species to abstract the protons from these protonated heterocycles. Therefore, filling these gaps with suitable high boiling amphoteric species could complete the conduction pathway and what could be a better guest than the same heterocycle of matching basicity? So we post-synthetically loaded triazole into **6** by stirring it in a methanolic solution of triazole. The loading was confirmed via several analytical techniques like PXRD, TGA and CHN analysis (Figure 4.5, Table 4.A.1). The PXRD pattern for **6_Tz** was very similar to that of **6**. From elemental analysis and TGA, we unambiguously confirmed the loading of neutral guest giving an overall formula $Nd(Ox)_2Tz^+.Tz.x$solvents (1:1::protonated:neutral triazole, **6_Tz**). We did a control experiment where we measured PXRD for the physical mixture of **6** and triazole. The pattern looked different and had diffraction peaks for the triazole. Similarly, the TGA profile for the control proved that stirring **6** in a methanolic solution of triazole, gets triazole loaded into the pores of the MOF and is not just a mixture of the two. When gas sorption was carried out on **6_Tz**, it was observed that it takes less CO_2 when compared to **6**, also proving the loading of triazole (Figure 4.A.3). Unfortunately, the single crystal structure of **6_Tz** could not be obtained, and thus we resorted to some modeling studies to evaluate the structure.

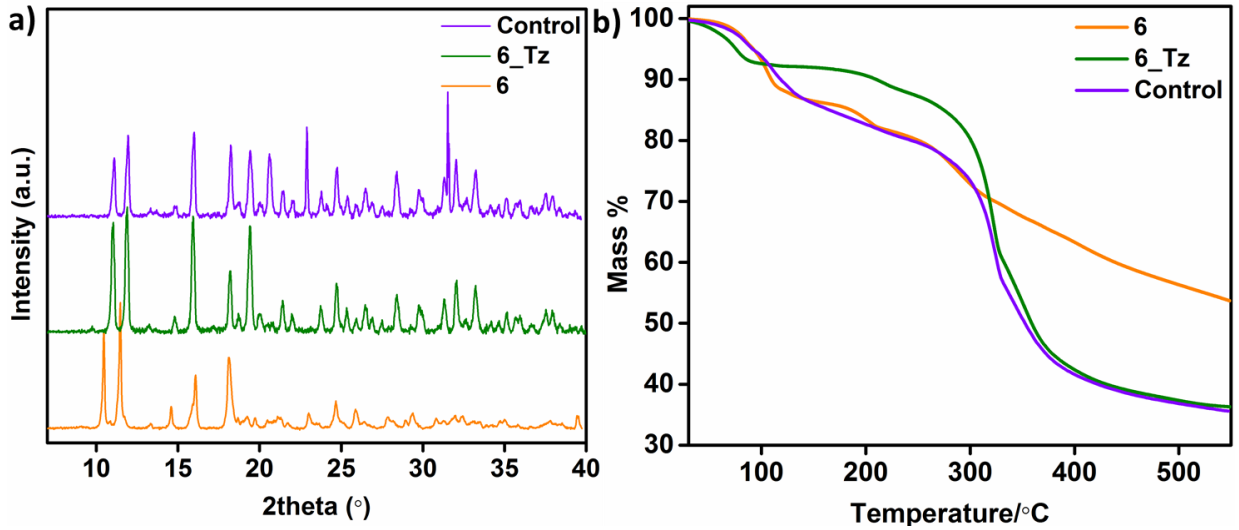

Figure 4.5. (a) Comparison of powder XRD patterns of **6**, **6_Tz** and the control proving the loading of neutral triazole into the pores of **6**. (b) TGA profiles of **6**, **6_Tz** and the control.

4.3.4.1. Modeling studies

All modeling studies were performed using Materials Studio (Accelrys), V.6.0. Using Grand Canonical Monte Carlo (GCMC) simulation, we introduced four molecules of triazole per unit cell of **6**. This count of neutral triazole is derived from the triazole content determined from the analytical characterizations (1:1::protonated:neutral triazole). The resulting configuration had the neutral triazole occupying the spaces left by the water molecules which were present in the as-made phase. Interestingly, this leaves a structure, wherein the 1-D channels along the a-axis of the honeycomb lattice get occupied by the neutral triazoles, while the 1-D channels along the c-axis are filled by the already present protonated triazoles (Figure 4.6 a). This structure was used as a starting model, and a Pawley refinement was carried out. The resulting fit is shown in figure 4.6 b. Importantly, the refined cell was quite comparable to the unit cell obtained from the single crystal XRD (**6**: $P2_1/c$, a= 9.953Å, b=17.08Å, c=8.782Å, β=101.394°, V= 1463.75Å^3, **6_Tz**: $P2_1/c$, a= 9.932 Å, b= 16.973 Å, c= 9.592 Å, β=101.394°, V= 1463.75Å^3) and both the cationic and the neutral triazoles were residing in positions described earlier.

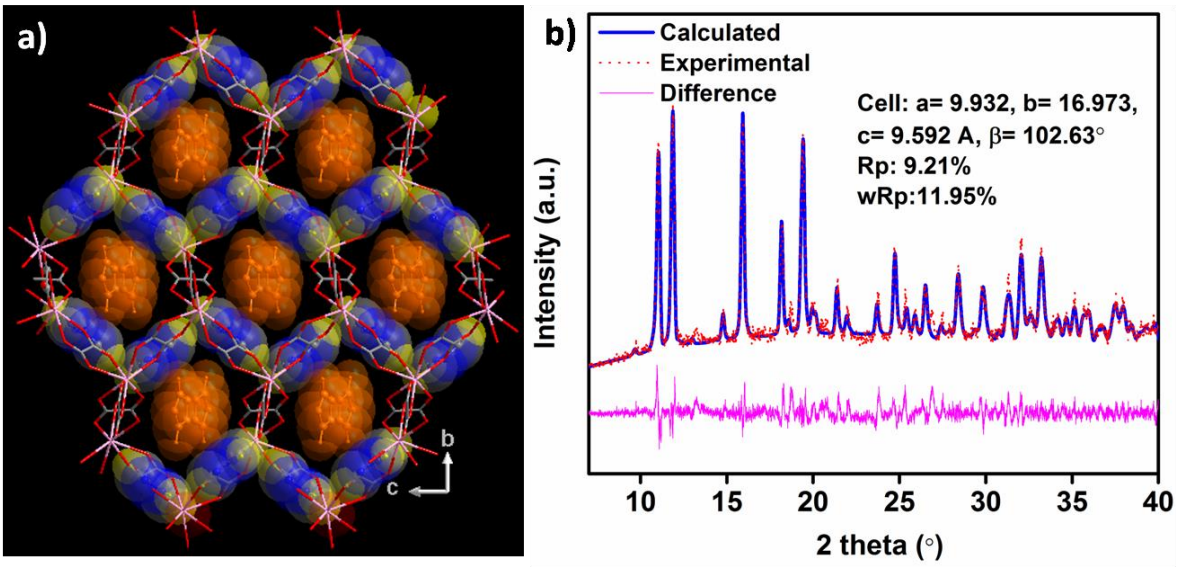

Figure 4.6. (a) Simulated structure of **6_Tz**. The triazoles have been shown as space fill for clarity. The loaded neutral triazoles along the a-axis are shown in orange whereas the already present protonated ones

along the c-axis are colored by elements. Color code: Pink: Nd, Red: O, Gray: C, Blue: N, Yellow: H. (b) Pawley fit for **6_Tz**. The unit cell is shown as an inset.

A satisfactory fit was obtained, and the refined structure clearly showed two columns; one of the protonated triazoles running along the c-axis and the other of the neutral triazoles running along the a-axis. More importantly, in addition to these two columns, we had another pathway for proton transfer running through both the protonated and neutral triazoles (Figure 4.7). The distances between the neutral triazoles and between the neutral and protonated triazoles were found to be well within the hydrogen bonding range. Interestingly, on refinement, the distances between the initial protonated triazoles didn't seem to be affected much.

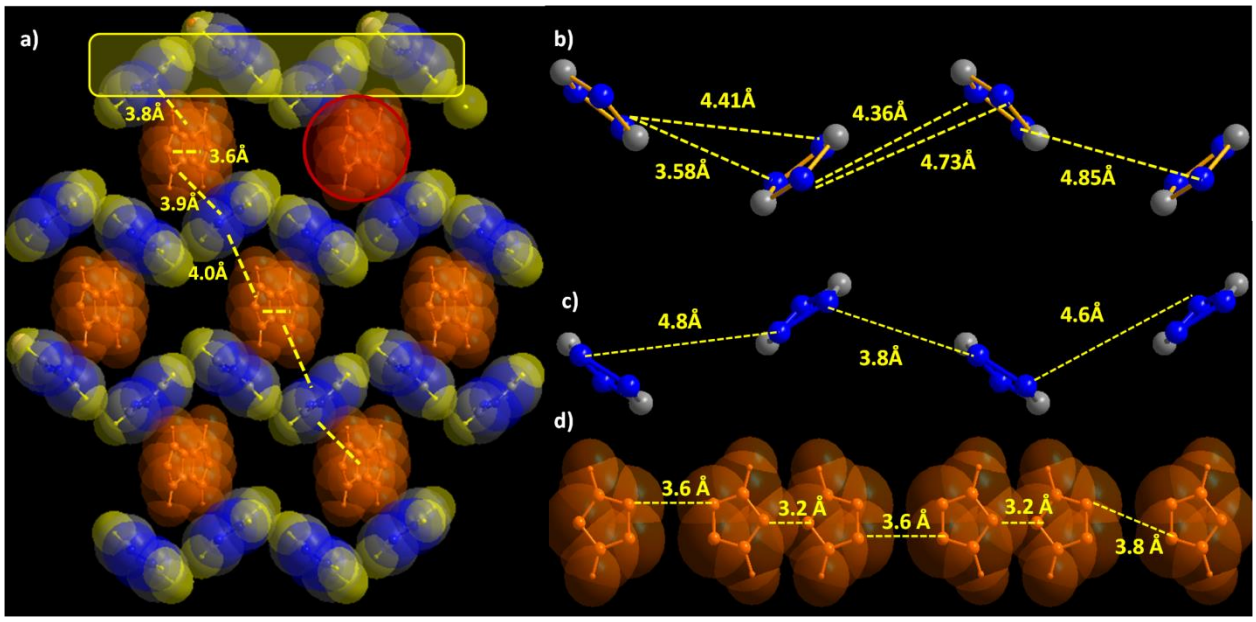

Figure 4.7. (a) The three columns of triazoles in **6_Tz**; protonated triazoles along c-axis highlighted in a yellow rectangle, neutral triazoles along a-axis highlighted in the red circle, and both neutral and protonated triazoles. The framework of the MOF is not shown for clarity. Distances between the neutral and protonated triazoles have been shown in the figure. Distances between the protonated triazoles in (b) **6** and after refinement in (c) **6_Tz**. (d) The distances between the neutral triazoles in **6_Tz**. Color code: Pink: Nd, Red: O, Gray: C, Blue: N, Yellow: H.

4.3.4.2. Impedance studies

Considering the closely knit, gas-tight percolating pathway provided by the protonated triazoles, neutral triazoles and water for the protons to travel, we measured the sample for proton

conduction. To assess the capability of these samples to work as solid electrolytes, we measured the alternating-current (ac) impedance spectra for the pelletized samples. The measurements were done from 30˚C to 90˚C at 90% relative humidity and under anhydrous condition from 120˚C to 150˚C. At 90˚C, 90% RH the conductivity was 10^{-2} S/cm which is 10-fold higher than what was observed for **6**. More importantly, the anhydrous proton conductivity of 1.02 x 10^{-4} S/cm at 150˚C could be realized (Figure 4.8). The conductivities and activation energies are listed in the figure 4.8.

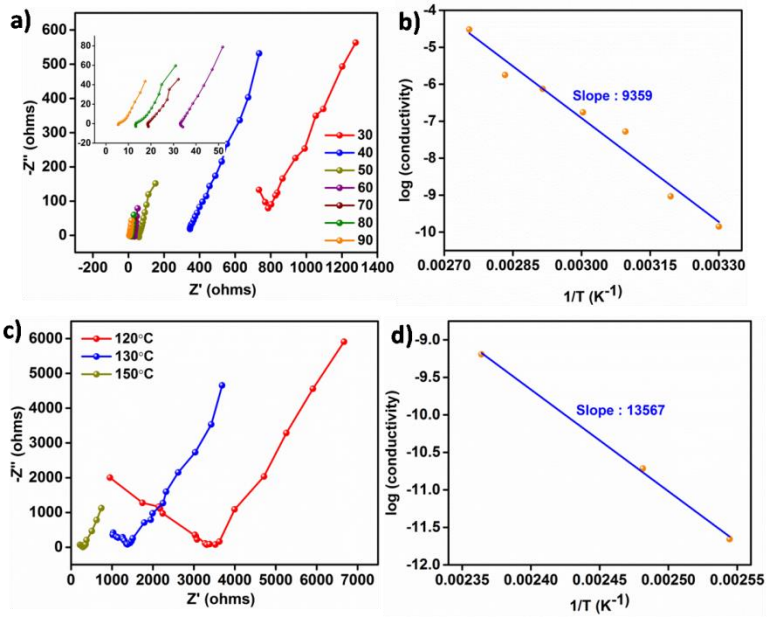

Conductivity and activation energy for 6 and 6_Tz at 90˚C and 90% RH

MOF	Conductivity @ 90°C/90%RH (S/cm)	Ea (eV)
6	3.06 x 10^{-03}	0.30
6_Tz	1.09 x10^{-02}	0.80

Conductivity and activation energy for 6_Tz at different temp. under anhydrous condition

6_Tz	Conductivity	Activation energy (eV)
120°C	8.67 x 10^{-06}	1.16
130°C	2.22 x10^{-05}	
150°C	1.02 x 10^{-04}	

Figure 4.8. (a) Nyquist plot for **6_Tz** at different temperatures under 90% RH. (b) The Arrhenius behavior shown by the conductivity for **6_Tz** at 90% humidity. (c) Nyquist plot for **6_Tz** at high temperatures under anhydrous condition. (d) The Arrhenius behavior shown by the conductivity for **6_Tz** under anhydrous condition. The tables show the conductivity and activation energy under different conditions.

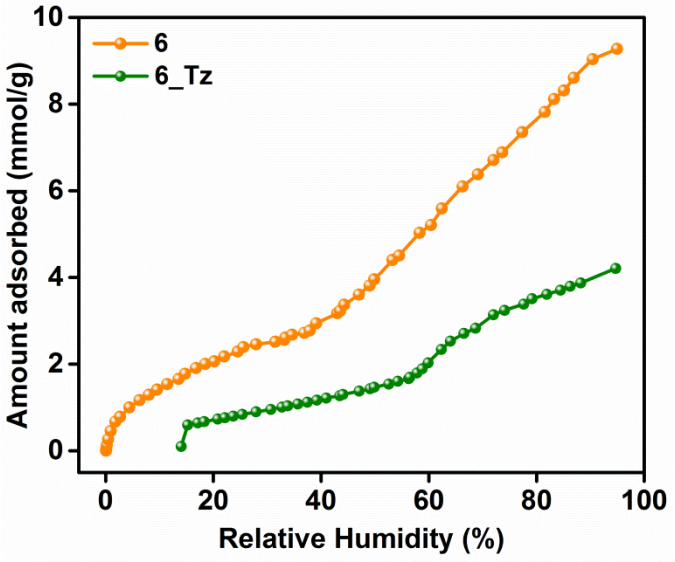

Figure 4.9. Comparison of water sorption of **6** and **6_Tz** at 298 K.

Interestingly, the water sorption studies on **6_Tz** showed a very similar adsorption isotherm profile, with a shallow uptake at lower pressures and a influxion at P/P_0 of 0.55, however, the overall uptake is only 4 mmol/g as against the 9.3 mmol/g observed for **6** (Figure 4.9). This suggests that the pore-structural variations created by the neutral triazole are not drastic but the overall solvent accessible void space is decreased. This structural change has marked differences in their proton conductivity and the activation energy. The **6** has a conductivity of $3x10^{-3}$ S/cm while in **6_Tz** this jumps by 10-fold to 1.09×10^{-2} S/cm with the activation barrier increasing from 0.3 to 0.8 eV, as would be expected for a more tightly packed channels.

4.3.5. Post Impedance and water stability

The post-impedance stability of all the four samples was confirmed by comparing the before and after-impedance phases by using different analytical techniques. The powder pattern of all the samples before and after impedance measurements matched extremely well (Figure 4.10 a). TGA also showed a good match between the decomposition profiles of these phases, which confirmed the absence of any decomposition of the sample under the measurement conditions (Figure 4.A.4). The scanning electron micrographs of the pre- and post-impedance samples also showed a good match (Figure 4.A.5). Notably, all these samples were stable in

water which is a very important requirement for an electrolyte to be stable under hydrous conditions (Figure 4.10 b).

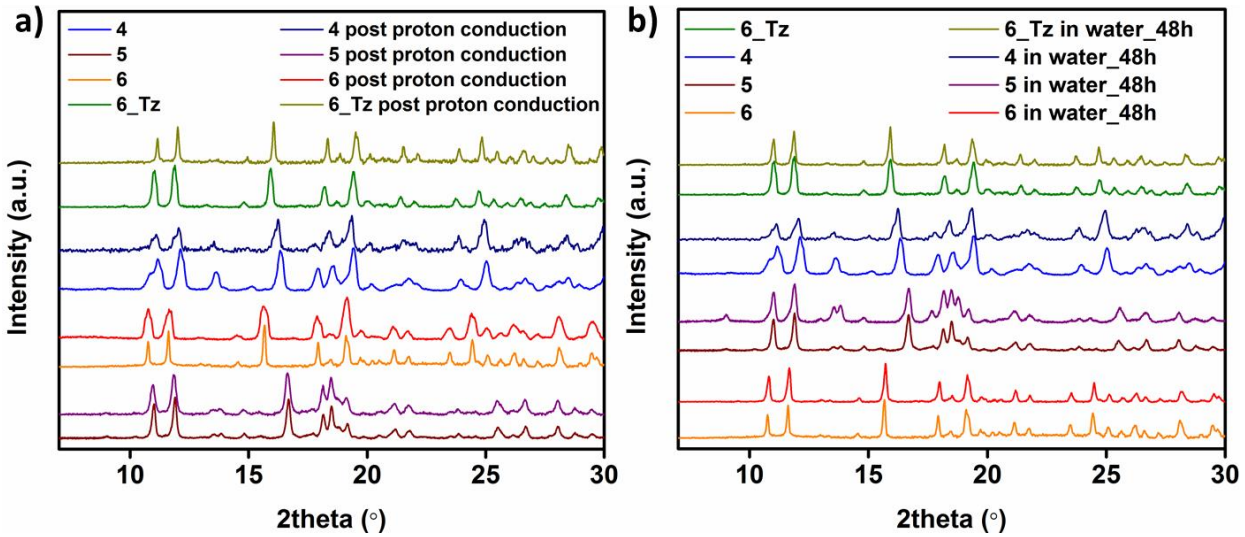

Figure 4.10. Figure showing the powder XRD patterns of all the samples (a) before and after proton conduction measurements and (b) in water for 48 hours.

4.4. Conclusions

To summarize, we have reported a family of Nd oxalate MOFs with different protonated azoles in the pore. On comparing the conductivities of these MOFs, we observe that the conductivity of all these MOFs increases as the basicity of the azoles decreases. We realized that the MOFs with the only protonated guest in the pore (**4**, **5**, and **6**) do not show any high-temperature proton conductivity. In the absence of water under anhydrous conditions, the distances between these guest molecules aren't favorable for proton conduction. Also, we need a species that can extract these protons from the azoles. Considering **6** shows the highest conductivity amongst three, we chose it for post-synthetic modification and loaded neutral triazoles on top of the already present protonated ones in the framework. The cooperativity between the neutral and protonated triazoles provides a facile proton transfer pathway that most probably remains intact under anhydrous conditions (~150˚C).

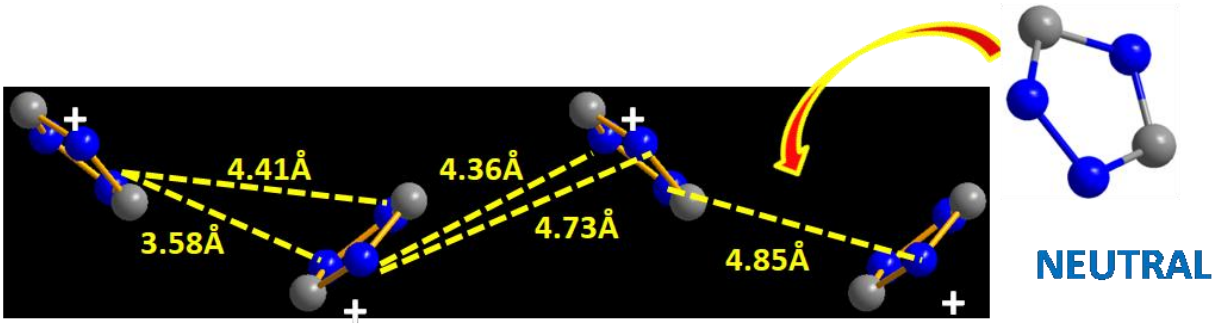

6_Tz	Conductivity @ 90°C/90% RH (S/cm)	Activation energy (eV)
90C/90%rH	1.09×10^{-02}	0.80
120°C	8.67×10^{-06}	1.16
130°C	2.22×10^{-05}	
150°C	1.02×10^{-04}	

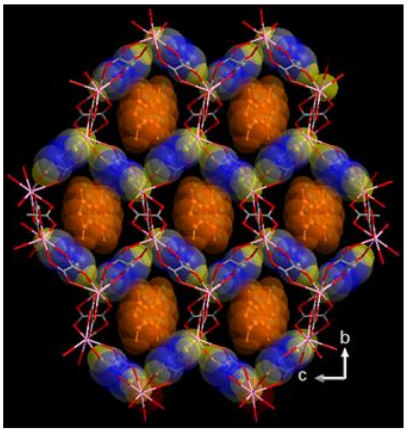

6_Tz shows a high conductivity of 10^{-2} S/cm at 90˚C, and 90% RH which is comparable to the Nafion and also shows high-temperature proton conduction; a feature that's absent in Nafion. When compared to the conductivity value for a MOF at high temperature under the anhydrous condition, **6_Tz** shows a notable conductivity value as shown in table 4.A.2. Considering there are ubiquitous numbers of anionic frameworks with protonated guests, this approach could open up a chance for transforming such near-favorable proton conducting MOFs into useful solid-state proton conductors.

4.5. References

1. Laberty-Robert, C.; Valle, K.; Pereira, F.; Sanchez, *Chem. Soc. Rev*. **2011**, *40*, 961.
2. Yoon, M.; Suh, K.; Natarajan, S.; Kim, K. *Angew. Chem. Int. Ed*. **2013**, *52*, 2688.
3. Ramaswamy, P.; Wong, N. E.; Shimizu, G. K. H. *Chem. Soc. Rev*., **2014**, *43*, 5913.
4. Yamada, T.; Kitagawa, H. *ChemPlusChem* **2016**, *81*,.
5. Li, A.-L.; Gao, Q.; Xu, J.; Bu, X.-H. *Coord. Chem. Rev*. **2017**, *344*, 54.
6. Meng, X.; Wang, H.-N.; Song, S.-Y.; Zhang, H.-J. *Chem. Soc. Rev*. **2017**, *46*, 464.
7. Grot, W. *Chem. Ing. Tech*. **1972**, *44*, 167.
8. Grot, W. *Chem. Ing. Tech*. **1978**, *50*, 299.
9. Moilanen, D. E.; Spry, D. B.; Fayer, M. D. *Langmuir*, **2008**, *24*, 3690–368.
10. Mauritz, K. A.; Moore, R. B. *Chem. Rev*. **2004**, *104*, 4535.
11. Ivanchev, S. S. *Russ. J. Appl. Chem*. **2008**, *81*, 569.
12. Maréchal, M.; Souquet, J.-L.; Guindet, J.; Sanchez, J.-Y. *Electrochem. Commun*. **2007**, *9*, 1023.
13. Phang, W. J.; Jo, H.; Lee, W. R.; Song, J. H.; Yoo, K.; Kim, B. S.; Hong, C. S. *Angew. Chem., Int. Ed*. **2015**, *54*, 5142.
14. Ponomareva, V. G.; Kovalenko, K. A.; Chupakhin, A. P.; Dybtsev, D. N.; Shutova, E. S.; Fedin, V. P. *J. Am. Chem. Soc*. **2012**, *134*, 15640.
15. Ramaswamy, P., Wong, N. E., Gelfand, B. S.; Shimizu, G. K. H. *J. Am. Chem. Soc*. **2015**, *137*, 7640.
16. Taylor, J. M.; Dawson, K. W.; Shimizu, G. K. H. *J. Am. Chem. Soc*. **2013**, *135*, 1193.
17. Kim, S. R.; Dawson, K. W.; Gelfand, B. S.; Taylor, J. M.; Shimizu, G. K. H. *J. Am. Chem. Soc*. **2013**, *135*, 963.
18. Bureekaew, S.; Horike, S.; Higuchi, M.; Mizuno, M.; Kawamura, T.; Tanaka, D.; Yanai, N.; Kitagawa, S. *Nat. Mater*. **2009**, *8*, 831.
19. Tang, Q.; Liu, Y.; Liu, S.; He, D.; Miao, J.; Wang, X.; Yang, G.; Shi, Z.; Zheng, Z. *J. Am. Chem. Soc*. **2014**, *136*, 12444.
20. Nandi, S.; Dhavale, V. M.; Shalini, S.; Werner-Zwanziger, U.; Singh, H.; Kurungot, S.; Vaidhyanathan, R. *Adv. Mater. Interfaces* **2015**, *2*, 1500301.
21. Shalini, S.; Aggarwal, S.; Singh, S. K.; Dutt, M.; Ajithkumar, T. G.; Vaidhyanathan, R. *Eur. J. Inorg. Chem*. **2016**, *27*, 4382.

22. Inukai, M.; Horike, S.; Umeyama, D.; Hijikata, Y; Kitagawa, S. *Dalton Trans*. 2012, *41*, 13261.
23. Shalini, S.; Dhavale, V. M.; Eldho, K. M.; Kurungot, S.; Ajithkumar, T. G.; Vaidhyanathan, R. *Scientific reports*, **2016**, *6*, 32489.
24. Pardo, E.; Train, C.; Gontard, G.; Boubekeur, K.; Fabelo, O.; Liu, H.; Dkhil, B.; Lloret, F.; Nakagawa, K.; Tokoro, H.; Ohkoshi, S.-i.; Verdaguer, M. *J. Am. Chem. Soc*. **2011**, *133*, 15328.
25. Mon, M.; Vallejo, J.; Pasán, J.; Fabelo, O.; Train, C.; Verdaguer, M.; Ohkoshi, S.-i.; Tokoro, H.; Nakagawae, K.; Pardo, E. *Dalton Trans*. **2017**, *46*, 15130.
26. Shigematsu, A.; Yamada, T.; Kitagawa, H. *J. Am. Chem. Soc*. **2011**, *133*, 2034.
27. Hurd, J. A.; Vaidhyanathan, R.; Thangadurai, V.; Ratcliffe, C. I.; Moudrakovski, I. L.; Shimizu, G. K. H. *Nat. chem*. **2009**, *1*, 705.
28. Kreuer, K.-D. *Chem. Mater*. 1996, *8*, 3.
29. Quartarone, E.; Angioni, S.; Mustarelli, P. *Materials* **2017**, *10*, 687.
30. Baran, R.; *Clays and Clay Minerals*, **2005**, *53*, 137.
31. http://www.chemicalbook.com/ProductMSDSDetailCB3756001_EN.htm.
32. Inukai, M.; Horike, S.; Itakura, T.; Shinozaki, R.; Ogiwara, N.; Umeyama, D.; Nagarkar, S.; Nishiyama, Y.; Malon, M.; Hayashi, A.; Ohhara, T.; Kiyanagi, R.; Kitagawa, S. *J. Am. Chem. Soc*. **2016**, *138*, 8505.
33. Umeyama, D.; Horike, S.; Inukai, M.; Kitagawa, S. *J. Am. Chem. Soc*. **2013**, *135*, 11345.
34. Umeyama, D.; Horike, S.; Inukai, M.; Itakura, T.; Kitagawa, S. *J. Am. Chem. Soc*. **2012**, *134*, 12780.
35. Umeyama, D.; Horike, S.; Inukai, M.; Hijikata, Y.; Kitagawa, S. *Angew. Chem*. **2011**, *50*, 11706.
36. Nagarkar S. S.; Unni S. M.; Sharma A.; Kurungot S.; Ghosh S. K. *Angew. Chem. Int. Ed*. **2014**, *53*, 2638.
37. Panda, T.; Kundu, T.; Banerjee, R. *Chem. Commun*. **2013**, *49*, 6197.

4.A. Appendix

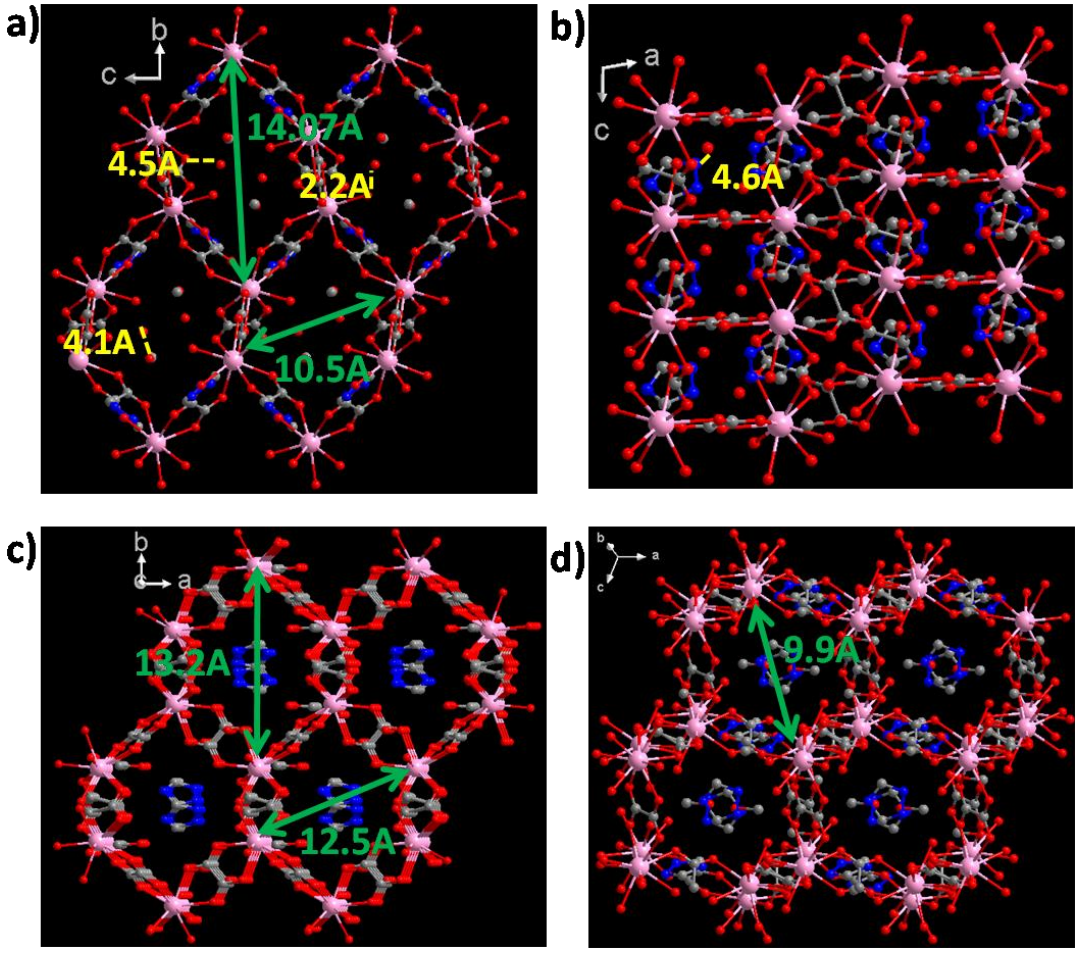

Figure 4.A.1. The dimensions of the rhombic channels of **6** along (a) a-axis, (b) b-axis, (c) c-axis, and (d) [1 1 1] direction. The distances between the triazoles, water and methanol molecules have also been shown.

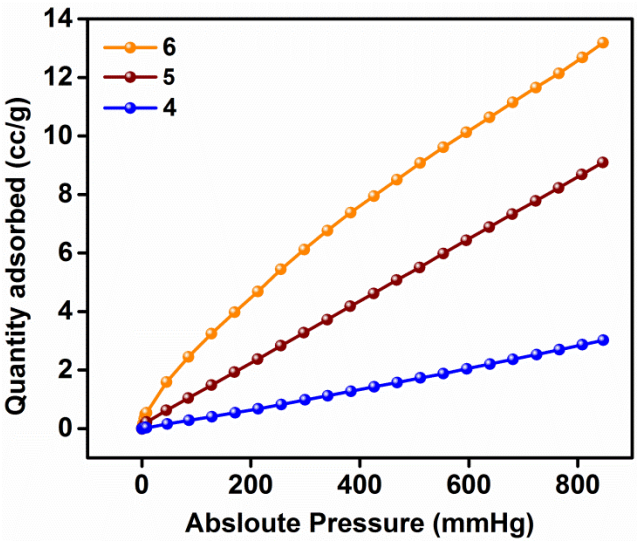

Figure 4.A.2. CO_2 adsorption isotherms of the three phases at 273 K. Note: No N_2 was adsorbed even at 77K.

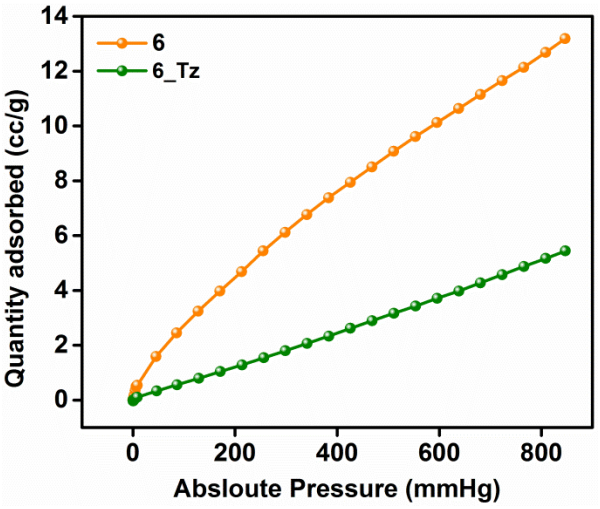

Figure 4.A.3. CO_2 isotherms of **6** and **6_Tz** at 273K. **6_Tz** has an uptake ~half of that of **6,** proving the loading of triazole into the pores of the MOF.

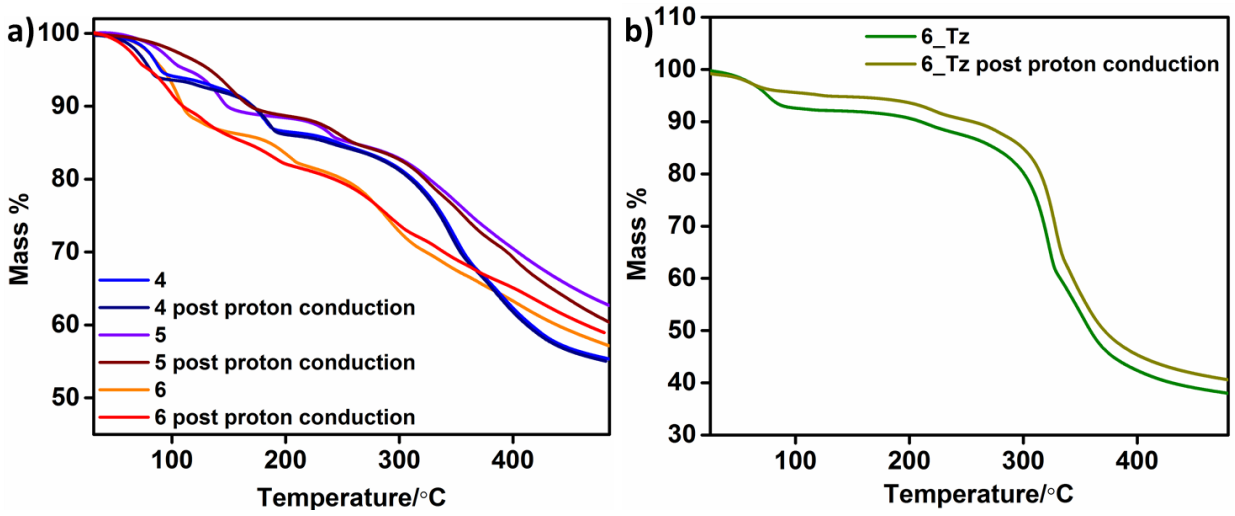

Figure 4.A.4. The thermal decomposition profiles of all the MOFs before and after impedance measurements.

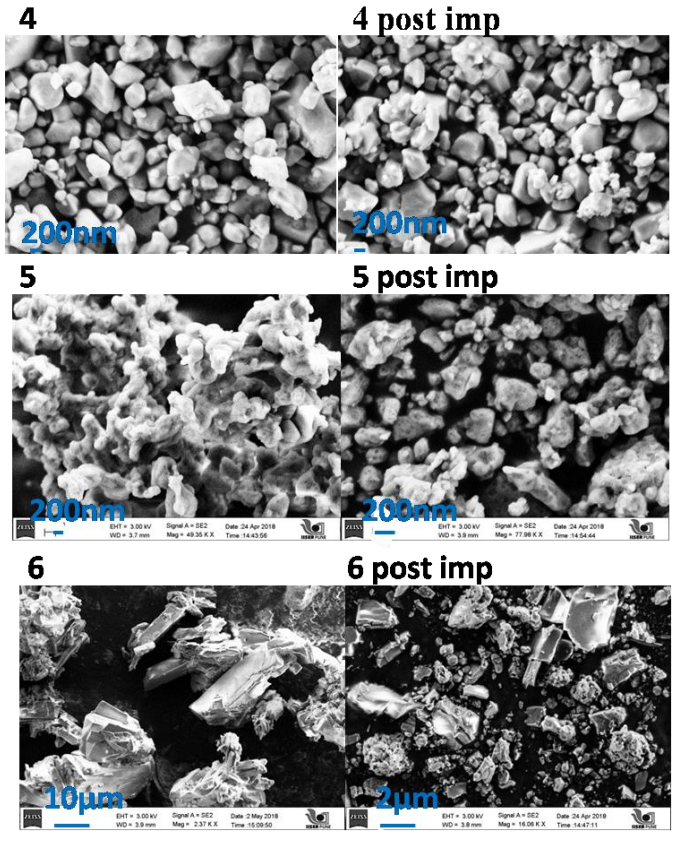

Figure 4.A.5. Scanning electron micrographs of **4**, **5** and **6** before and after impedance measurements.

Table 4.A.1. Comparison of CHN values of **6** and **6_Tz.**

	6		**6_Tz**	
Element	**Observed %**	**Calculated %**	**Observed %**	**Calculated %**
C	18.04	18.38	19.08	20.53
N	8.97	9.19	16.69	15.96
H	1.96	2.42	1.98	2.68

Table 4.A.2. Comparison of the conductivity of **6_Tz** with reported MOFs under anhydrous conditions.

MOF	**Guest**	**Conductivity (S/cm)**	**T (˚C)**	**Ea (eV)**	**Reference**
$[Zn(H_2PO_4)_2\text{-}(C_2N_3H_3)_2]_n$	Phosphoric acid	10^{-3}	150	0.53	32
$[Zn_3(H_2PO_4)_6](Hbim)$ (Hbim = benzimidazole)	Benzimidazole	10^{-3}	120	0.5	33
6_Tz	**Triazole**	**10^{-4}**	**150**	**1.16**	**This work**
$[Zn(H_2PO_4)_2(TzH)_2]_n$		10^{-4}	150	0.6	34
$Al(\mu2\text{-}OH)(1,4\text{-}ndc)_n$ (1,4-ndc = 1,4-naphthalenedicarboxylate)	Histamine	10^{-4}	150	0.25	35
$\{[(Me_2NH_2)_3(SO_4)]_2[M_2(ox)_3]\}_n$	$[(Me_2NH_2)_3(SO_4)]^{+1}$	10^{-4}	150	0.12	36
β-PCMOF-2$(Tz)_{0.45}$	Triazole	10^{-4}	150	0.34	27

$Al(\mu 2\text{-}OH)(1,4\text{-}ndc)_n$	Imidazole	10^{-5}	120	0.6	18
In isophthalate MOF	$[(CH_3)_2NH_2]^+$	10^{-5}	90		37
$\{Al(\mu 2\text{-}OH)(1,4\text{-}bdc)\}_n$	Imidazole	10^{-7}	120	0.9	18
$[Zn_2(2,5\text{-}DOTP)]_n$-His	Histamine	10^{-9}	146		22